Compressible and Geometrical Effects on Shearless Turbulent Mixing

by

Eunhye An

A dissertation submitted in partial fulfillment
of the requirements for the degree of
Doctor of Philosophy
(Mechanical Engineering)
in The University of Michigan
2023

Doctoral Committee:

Associate Professor Eric Johnsen, Chair
Associate Professor Jesse Capecelatro
Assistant Professor Yulin Pan
Assistant Professor Aaron Towne

Eunhye An

graceunh@umich.edu

ORCID iD: 0009-0009-8779-9241

Dedicated to my parents and brother,

and to my beloved in life, Jaesong and Logan

ACKNOWLEDGEMENTS

First of all, I would like to express my deepest gratitude to my advisor, Eric Johnsen, for giving me the opportunity to pursue my Ph.D at the University of Michigan. His mentorship and guidance have been invaluable to me and improved me for the better. I am grateful for his consideration and respect throughout my Ph.D. journey. I would also like to extend my appreciation to the Committee members - Prof. Jesse Capecelatro, Prof. Yulin Pan, and Prof. Aaron Towne - for their invaluable contribution to the improvement of my research. In addition, I would like to acknowledge Prof. Haecheon Choi for his exceptional guidance during my Master's programs and beyond.

To my loving parents and my one and only brother, Eunseok, I owe them the greatest appreciation for their love, support, and belief in me that have been the biggest motivation behind my achievements. I also hold love and appreciation for my parents-in-law. To my beloved in life, Jaesong, and my most precious Logan, my life has been made more valuable and filled with love because of them. Thank you for always being there for me.

To my friends in Michigan who made my life happy and kept me company and those who supported me in South Korea, I am truly thankful. I never forget the SCFPL members. They gave unwavering assistance and have always been supportive. Please contact me when you visit South Korea, and I will treat you to a great Korean BBQ (I am sure that it will be better than Tomokun). I am grateful for the support I received from the Korea Air Force and my colleagues at the Korea Air Force Academy

who encouraged me throughout my Ph.D. program.

Lastly, I would like to express my gratitude to God for always leading me in the right direction.

TABLE OF CONTENTS

LIST OF FIGURES

Figure

LIST OF TABLES

Table

LIST OF APPENDICES

Appendix

ABSTRACT

Compressible turbulent mixing plays an important role in a variety of astrophysical and engineering problems ranging from combustion engines to star formation in space. These flows involve complex physics, such as entrainment, mass/momentum transfer, and viscous dissipation. While incompressible, homogeneous turbulence is relatively well understood, compressibility and inhomogeneity pose challenges to classical theory due to different energy transfer and dissipation mechanisms. Our aim is to conduct high-fidelity numerical simulations to investigate how compressible turbulent flows mix and decay, and how heterogeneity affects these dynamics. We first propose an improved process for generating an initial velocity field that obtains an equilibrium turbulence state with desired properties such as Reynolds number, turbulent Mach number, and the most energetic wavenumber. The rescaled field exhibits the expected $k^{-5/3}$ energy spectrum from time zero. This approach provides a systematic procedure to initialize homogeneous isotropic turbulent fields, which results in the quasi-equilibrium state with higher Reynolds numbers. This enables us to investigate the mixing mechanisms in early stages such as entrainment.

Using this initialization procedure, we investigate shearless compressible turbulent/non-turbulent mixing. We juxtapose an initially shearless homogeneous isotropic turbulent field with a stationary fluid. Near the turbulent/non-turbulent interface, turbulent eddies entrain, and viscous stresses at smaller scales impart vorticity to the irrotational region; then the mixing region develops. The growth of the mixing region follows a self-similar power law of 2/3 in time, consistent with *Barenblatt et al.*

(1987). Moreover, we find that compressibility effects through acoustic waves cause energy losses and result in an enhanced decay of turbulent kinetic energy because kinetic energy is transferred to less energetic flow regions. We propose the new scaling law for the decay of turbulent kinetic energy to account for this compressibility in turbulent/non-turbulent mixing, which we validate using direct numerical simulations.

We then extend this study to investigate shearless compressible turbulent mixing with gradients in turbulent intensity. The flow is initialized by juxtaposing two homogeneous isotropic turbulent fields of different turbulent intensities. The higher-intensity flow has a broader range of scales; it penetrates extensively into the lower-energy region with intermittency. Therefore, there is net energy transfer from the higher- to the lower-intensity regions by dilatation along the inhomogeneous direction. These inhomogeneity and compressibility effects are represented as energy loss and gain in the scaling for the decay of turbulent kinetic energy, leading to delayed and enhanced decay rates.

Geometrical effects on compressible turbulent/non-turbulent mixing are investigated for the propagation of a decaying turbulent front in planar and cylindrical geometries. We show that the cylindrical interface propagates as a power law in time with an exponent of 1/2, which is confirmed by dimensional analysis. The turbulent kinetic energy is determined by the dissipation rate and the triple moment of velocity derivatives; the dissipation rate is independent of the geometry of turbulence because there are no energy production mechanisms. On the other hand, dilatational energy transfer, which is represented as a triple moment of velocity derivatives is subject to the dimension of turbulent fields. Therefore, cylindrical turbulence exhibits more significant energy losses due to acoustic waves propagating to the non-turbulent region compared to planar turbulence. This physics is well described by the new scaling law with appropriate coefficients. This study can improve the understanding and predic-

tion of the complex turbulent flows of engineering relevance and the development of turbulent models.

CHAPTER I

Introduction

This chapter reviews turbulence fundamentals as a means to investigate shearless compressible turbulent mixing in regions of steep gradients in turbulent intensity. Such flows are observed in nature and engineering applications, e.g., atmospheric and oceanic flows, boundary layers, jets, and wakes. The classical theory of turbulence is introduced before discussing its limitations in the context of the present work and describing the state of the art in compressible turbulence and inhomogeneous flows. The objective and contributions of this thesis are subsequently detailed.

1.1 Turbulence: a Non-Linear and Multiscale Flow

Turbulent flow is commonly observed in our lives, such as clouds in the atmosphere, oceanic circulations, flow over aircrafts, and chemical reactions in engines. For example, Fig. 1.1(a) shows an experiment of cloud droplet formation in turbulence and atmospheric turbulence (*Shawon et al.*, 2021). This experiment investigated the effect of turbulence on aerosol-cloud interactions and cloud formation, where turbulence in the cloud increases the fraction of aerosol particles and contributes to the development of different types of clouds. Furthermore, Fig. 1.1(b) illustrates the interaction between molecular clouds in space. Turbulence is observed in molecular clouds, which cause mass and energy exchanges between regions with different

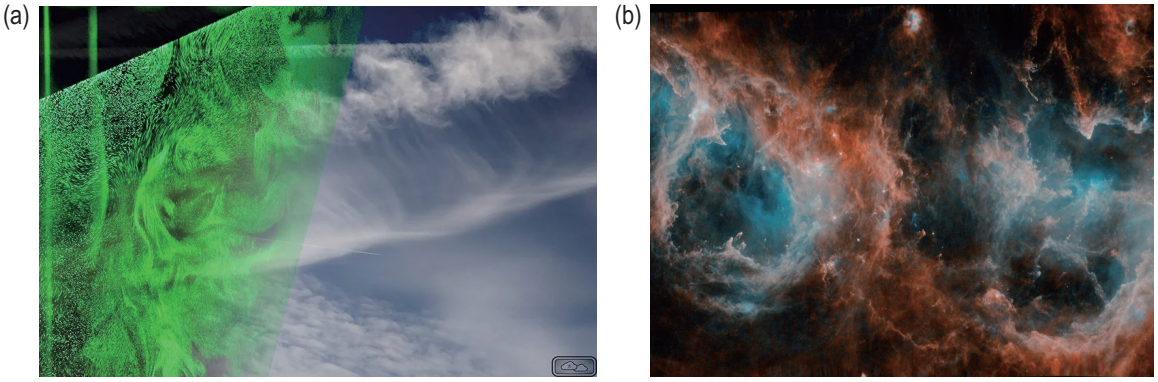

Figure 1.1: (a) Experiment of cloud droplets in turbulence (left) as a mechanism for the cloud formation (right). Reproduced from (*Shawon et al.*, 2021), with the permission of AGU. (b) Interaction between the W3/W4/W5 complex of molecular clouds triggers the formation of a new star. Courtesy NASA/JPL-Caltech.

compositions (density or turbulent intensity), and their kinetic energy inhibits the collapse of the clouds during star formation (*Federrath*, 2018).

An important characteristic of turbulence is variable fluctuations, which occur both in space and time. In turbulent flows, the velocity can be decomposed into two components: the mean velocity and turbulent fluctuation. This decomposition is achieved through the Reynolds decomposition, which follows as:

$$u(x,t) = u(x) + u'(x,t). \tag{1.1}$$

Fig. 1.2 shows the time variation of velocity component $U_1(t)$ for a particular point in a turbulent jet (*Pope*, 2000). While the mean velocity is invariant in time, the significant fluctuations reflect the random motions. These fluctuations occur at different amplitudes and time scales (frequencies), which indicate that the fluctuations u' consist of multiscale eddies that are vortical structures in turbulent fields (*Davidson*, 2015). These motions in turbulent flow are engaged in a nonlinearity, resulting in chaotic dynamics of the motion. The nonlinearity of equations of motion, such as Navier-Stokes equations, complicates the progress necessary to predict physics be-

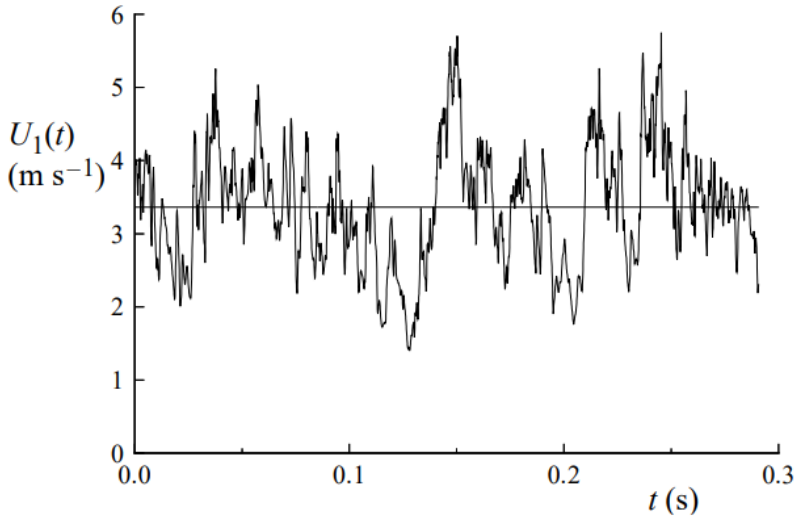

Figure 1.2: Time variation of velocity $U_1(t)$, measured at a given point in a turbulent jet. The mean velocity remains constant over time (solid line). Reprinted with the permission of the Cambridge University Press.

cause it is difficult to quantify the multiscale physics nonlinearly superposed in the flow. Therefore, turbulent motions are characterized by statistical properties. For example, the turbulent intensity can be characterized by the root-mean-square velocity u_{rms}, which is defined as $u_{rms} = \sqrt{\langle u'^2 \rangle}$. As a result, the role of turbulence in many applications has been qualitatively discovered, but the theoretical study of these flows has been limited, and significant costs in experiments and computational resources are required.

1.2 Kolmogorov Theory

Fig. 1.3(a) illustrates turbulence as multiscale energy cascade of eddies (*Richardson*, 1922), describing as:

> Big whorls have little whorls Which feed on their velocity, And little whorls have lesser whorls, And so on to viscosity.

For turbulent flow, large-scale eddies break up and transfer their energy to ever-smaller eddies until the energy is ultimately dissipated into heat. This process, known

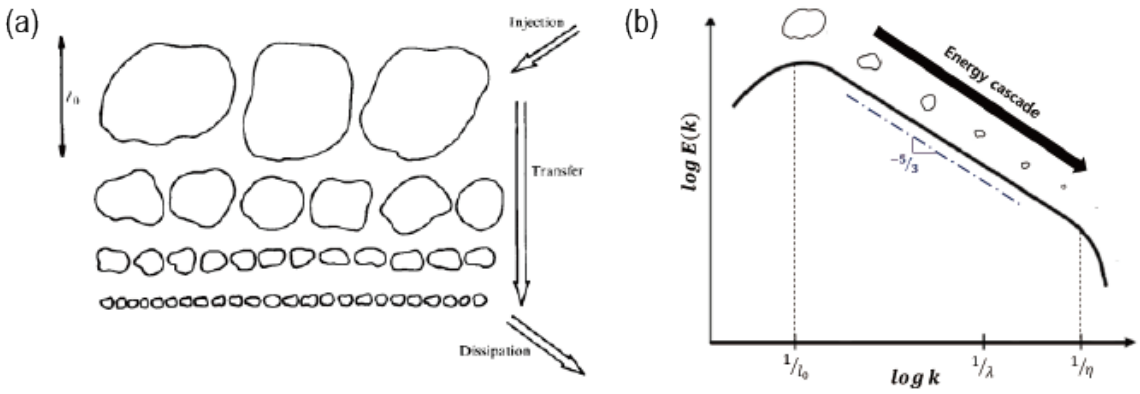

Figure 1.3: (a) Schematic of Richardson's energy cascade. Energy is injected into eddies of size l_0 and transferred to smaller-eddy until it is dissipated, where l_0 is the integral length scale. Reproduced from *Frisch et al.* (1978), with the permission of the Cambridge University Press. (b) Energy spectrum for turbulent flows. The energy is distributed across a range of scales from l_0 where the energy is injected to η where it is dissipated. The spectrum is scaled by the Kolmogorov $-5/3$ power law in the inertial range.

as the energy cascade, is quantified by Kolmogorov theory (*Kolmogorov*, 1941a,b, 1962). Kolmogorov hypothesized that turbulent flow at a sufficiently high Reynolds number has a universal equilibrium range, which is composed of the inertial subrange and the dissipation range. Fig. 1.3(b) shows the distribution of spectral energy in wavenumbers. The universality in this range leads to scaling analysis for spectral analysis of the inertial subrange, i.e., the Kolmogorov -5/3 spectrum $\left(E(k) \sim k^{-5/3}\right)$ (*Pope*, 2000; *Vassilicos*, 2015).

This classical theory assumes that the turbulent flow is incompressible, homogeneous, isotropic, and at sufficiently high Reynolds numbers. Homogeneous isotropic turbulence (HIT) is an appealing problem to understand basic turbulence dynamics and energy transfer because its statistical properties are invariant in position and direction. Therefore, HIT has been extensively used in analytical studies, direct numerical simulations (DNS), and wind-tunnel experiments. For instance, Fig. 1.4 shows the flows generated in a box of turbulence in computational simulations or downstream behind grids in wind-tunnel experiments. However, the flow generated

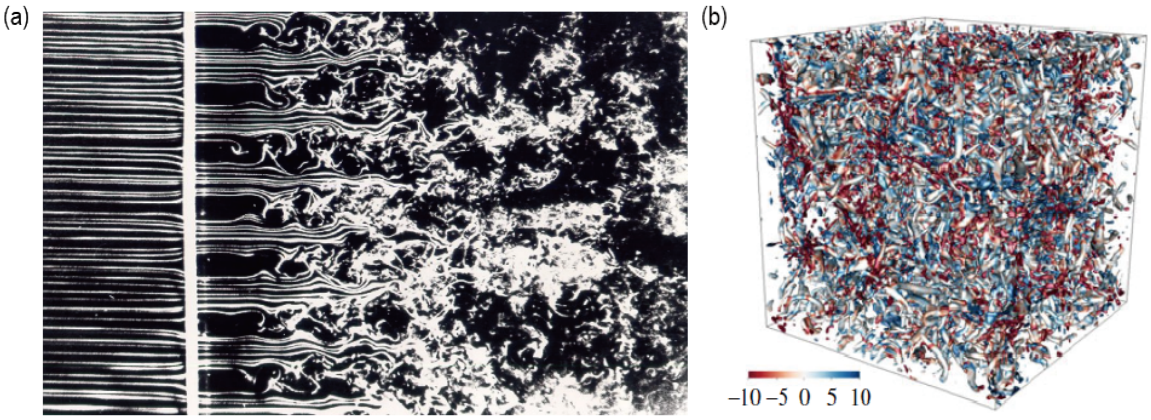

Figure 1.4: (a) Visualization of turbulence generated by grid experiments. Photograph by Thomas Corke and Hassan Nagib and reproduced from *Van Dyke and Van Dyke* (1982), with the permission of the Cambridge University Press. (b) Turbulent eddies of homogeneous isotropic turbulence in a periodic box, which is visualized by the Q-criterion and colored by dilatation. Reproduced from *Pan and Johnsen* (2017), with the permission of the Cambridge University Press.

by grids in wind-tunnel experiments is not homogeneous due to mean shear and/or experimental setups (e.g., walls in a test section), which causes inhomogeneity or distortion in the flow direction (*Tucker and Reynolds*, 1968; *Reynolds and Tucker*, 1975). Furthermore, anisotropy in Reynolds stresses persists even further downstream of the flow. Therefore, it is nearly impossible to generate HIT in experiments (*Ertunç et al.*, 2010). This problem is an idealization that helps us understand and analyze turbulent flows.

The turbulent kinetic energy (TKE) budget describes the energy balance in a turbulent flow. The TKE budget terms of transport, production, pressure-dilatation, and dissipation rate clarify the complex mechanism in the decay of TKE. In the case of shearless HIT, the properties of homogeneity and isotropy simplify the TKE equation by taking a volume average; as a result, terms involved in the spatial derivative and

the mean flow are canceled out to the following form (*Batchelor*, 1953):

$$\frac{dK}{dt} = \dot{\epsilon}, \tag{1.2}$$

where $K = \langle u_i u_i \rangle / 2$ is the total TKE per mass, u_i the velocity fluctuations, $\langle \cdot \rangle$ volume-averaged quantities, t time, and $\dot{\epsilon}$ the volume-averaged dissipation rate. This equation indicates that TKE decays only by viscous dissipation over time. The dissipation rate of TKE is defined as $\dot{\epsilon} = \nu \langle s_{ij} s_{ij} \rangle$, where s_{ij} is the strain rate tensor of velocity fluctuations, and ν is the kinematic viscosity. The dissipation rate can be approximated as $\dot{\epsilon} \sim u_{rms}^3 / L_f$, where L_f is the integral length scale and u_{rms} is the root-mean-squared velocity fluctuation (*Vassilicos*, 2015). The equilibrium dissipation quantity C_ϵ law is thus defined (*Batchelor*, 1953; *Sreenivasan*, 1984):

$$C_\epsilon = \dot{\epsilon} L_f / u_{rms}^3. \tag{1.3}$$

Fig. 1.5 shows the dissipation quantity C_ϵ as a function of Reynolds numbers based on the Taylor microscale λ for HIT in a periodic box, where the Taylor microscale is defined as

$$\lambda^2 = \frac{\langle u_i u_i \rangle}{\left\langle \left(\frac{\partial u_i}{\partial x_i} \right)^2 \right\rangle}. \tag{1.4}$$

Up to moderate Reynolds numbers ($Re_\lambda \leq 50$), the scaled dissipation rate decreases before approaching a constant beyond $Re_\lambda \approx 100$, C_ϵ. This behavior illustrates the fact that the dissipation rate depends on Re until the Reynolds number is sufficiently high ($Re_\lambda \approx 100$), at which point the dissipation rate no longer depends on the Reynolds number. These regimes correspond to the mixing transition, which changes the flow dynamics (*Dimotakis*, 2000). For $Re \gtrsim 100$, which is the transition Reynolds number, turbulent eddies follow -5/3 Kolmogorov power-law of the energy spectrum with length scales in an inertial range. Therefore, this equilibrium dissipation scaling

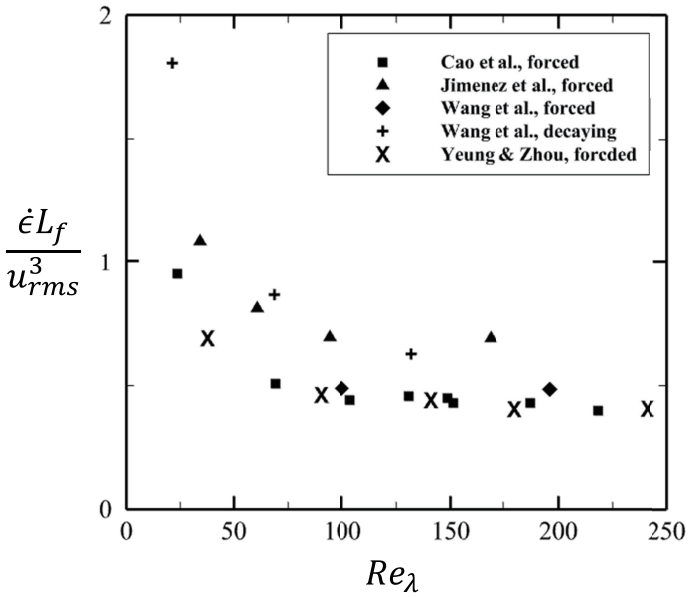

Figure 1.5: Dissipation quantity $C_\epsilon = \dot{\epsilon}L_f/u_{rms}^3$ vs. Reynolds number based on the Taylor microscale. Reproduced from *Sreenivasan* (1984), with the permission of AIP Publishing.

supports Kolmogorov's cascade theory. However, C_ϵ takes different values for turbulence generated by different types of grids, which shows its dependence on initial conditions (*Vassilicos*, 2015). Further scaling the dissipation rate as $\dot{\epsilon} \approx \nu u_{rms}^2/\lambda^2$, the ratio of integral length scale to the Taylor microscale is

$$L_f/\lambda \sim C_\epsilon Re_\lambda. \tag{1.5}$$

This equation implies that, for sufficiently high Reynolds numbers, the wider ranges of scales exist as $L_f \gg \lambda \gg \eta$ as the Reynolds number increases. It corresponds to Kolmogorov theory, where the Kolmogorov scale η is scaled as $L_f/\eta \sim Re_L^{9/4}$; therefore, the higher Reynolds numbers lead to broader scale separations, which requires higher energy to be dissipated. However, this conventional turbulence theory cannot be directly applied to turbulent flows in nature and engineering applications, which involve inhomogeneity and compressibility effects.

1.3 Compressible Turbulence

Compressible flow involves additional physics that are not observed in incompressible flow, such that Kolmogorov's theory is not directly applicable. The main effect of compressibility is that thermodynamics are coupled to the flow. As a result, velocity and thermodynamic variables fluctuate, which are decomposed into three modes: vorticity, acoustic, and entropy modes (*Kovasznay*, 1953; *Lele*, 1994). Hence, the thermodynamic state should be described along with the velocity field for compressible flow. For thermodynamic equilibrium turbulence, its state is determined by two independent thermodynamic quantities among the density, entropy, internal energy, and pressure, and then the others can be obtained by the equation of state (EOS) (*Durbin*, 2021). The variable fluctuations can be decomposed into solenoidal (rotational) and dilatational (irrotational) parts by Helmholtz decomposition. Fig. 1.6 illustrates solenoidal and dilatational modes of turbulence. The solenoidal part consists of vortical (rotational) structures, while the dilatational flow is irrotational and composed of sheet-like structures. *Federrath* (2018) investigated the effect of turbulence modes to form stars. Although turbulence contributes to the entire process of star formation, dilatational modes enhance star-formation rates by aggregating density. Therefore, the two modes of turbulence require different ways to analyze their characteristics. Fig. 1.7 presents the energy spectrum of solenoidal and dilatational modes for forced compressible HIT. While the solenoidal motions obey Kolmogorov theory and scales as the expected $-5/3$ power law, the dilatational motions fail the Kolmogorov scaling and require modification of the conventional theory (*Donzis and Jagannathan*, 2013; *Jagannathan and Donzis*, 2016).

Furthermore, compressibility effects appear in the evolution of TKE. TKE budget equation for shearless flow with no mean velocity and no external forces is described

as

$$\frac{\partial k}{\partial t} = -\frac{1}{\rho}\frac{\partial \left(p u_i\right)}{\partial x_i} - \frac{\partial}{\partial x_j}\left(\frac{1}{2} u_i u_i u_j\right) - 2\nu s_{ij} s_{ij}, \tag{1.6}$$

where $k = u_i u_i/2$ is the TKE and s_{ij} the strain-rate (*Pope*, 2000). The first term on the left-hand side $\frac{\partial k}{\partial t}$ is the local derivative of TKE, the first term on the right-hand side $\frac{1}{\rho}\frac{\partial (p u_i)}{\partial x_i}$ the pressure-dilatation, the second term on the right-hand side $\frac{\partial}{\partial x_j}\left(\frac{1}{2} u_i u_i u_j\right)$ denotes the transport, and the last term on the right-hand side $2\nu s_{ij} s_{ij}$ the dissipation rate, respectively. The dissipation rate is the main contributor to the TKE budget for both incompressible and compressible turbulence. For compressible flow, this term can be decomposed into incompressible ($\mu \omega_k \omega_k$) and compressible ($(\mu + \mu_b)\,\Theta$) contributions for homogeneous turbulence, where μ is the shear viscosity, μ_b the bulk viscosity, ω_k vorticity, and Θ the dilatation. The ratio of compressible and incompressible dissipations can serve as compressibility effects, which describe additional dissipation in the flow (*Lele*, 1994). Additionally, the pressure-dilatation term plays a crucial role in the exchange of energy between TKE and potential energy in the compressible flow. However, its contribution to the decay of TKE is negligible for shearless turbulence because it appears as a form of extra compressible dissipation, whereas the presence of shear intensifies the effects of the pressure-dilatation (*Sarkar*, 1992; *Lele*, 1994). Despite this, no theory describing the compressibility effects has been established yet, and thus, there is a need to improve the classical Kolmogorov theory for compressible flows.

1.4 Heterogeneous Flow: Free Shear Flow and Turbulent/Non-Turbulent Interface

The key feature of turbulence is mixing, which occurs owing to misaligned characteristics and/or variations in space and time. Turbulent mixing occurs in a three-stage process of entrainment, dispersion, and diffusion (*Pope*, 2000). Through this process,

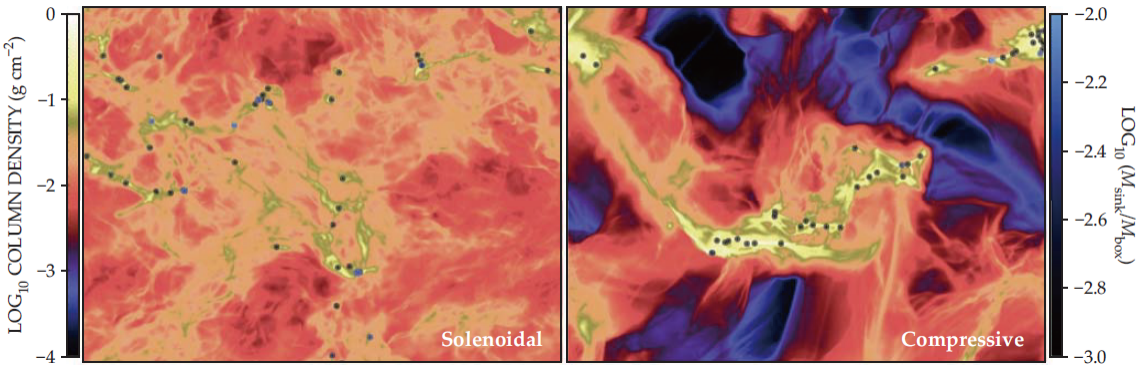

Figure 1.6: Density contours of solenoidal (left) and dilatational (right) modes. The black dots represent potential stars. The stars can combine more effectively in dilatational turbulence compared to solenoidal turbulence, which increases the rate of star formation by a factor of 15-20. Reproduced from *Federrath* (2018), with the permission of AIP Publishing.

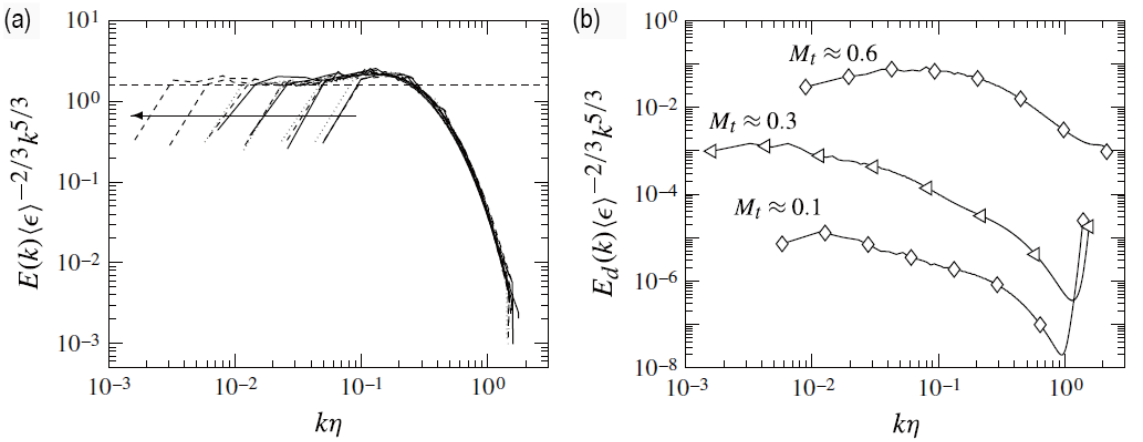

Figure 1.7: Energy spectrum of (a) solenoidal and (b) dilatational modes in forced compressible HIT normalized by the Kolmogorov -5/3 law for $Re_\lambda = 38-430$ at $Ma_t = 0.1, 0.3,$ *and* 0.6. Reproduced from *Donzis and Jagannathan* (2013), with the permission of the Cambridge University Press.

turbulent flow enhances the rate of mass, momentum, and energy transfer to the adjacent matter (solid, liquid, or gas) compared to laminar flow. According to *Dimotakis* (2005), turbulent mixing can be classified into three levels based on flow dynamics. Level-1 mixing involves passive scalars that do not affect flow dynamics, where the mixedness can be described as a fraction of molecular composition. Level-2 mixing, on the other hand, impacts the flow dynamics. Here, baroclinic vorticity is generated by misaligned quantities such as pressure-density or temperature-entropy gradients and develops instabilities and further mixing. For example, Rayleigh-Taylor instability, which occurs between two fluids with different densities with acceleration fields, can generate baroclinic vorticity and the growth of the mixing zone that is coupled with the flow dynamics. Level-3 mixing involves mixing that changes the flow itself, such as in combustion and supernova explosion. Nonlinear reactions in this mixing create tens to hundreds of species and their complex kinetics. Among these differences, Level-1 mixing has been widely investigated and has contributed to understanding mechanisms in many natural and engineering applications, such as the diffusion of pollutants in the air, weakly heated jets, and interactions between clouds and air (*Warhaft*, 2000).

However, heterogeneous flows involve additional transfer mechanisms, which means that the Kolmogorov theory cannot fully describe its effect. For instance, free-shear flows such as jets, wakes, and mixing layers are canonical problems for turbulent mixing caused by inhomogeneity effects. The flow with a mean velocity of U entrains an ambient fluid with the same properties, resulting in a statistically stationary and steady flow. Fig. 1.8 shows the turbulent/non-turbulent interface (TNTI) generated by mixing between ambient and turbulent flows. The TNTI is a finite interfacial layer, which is composed of two different layers: a viscous superlayer (VSL) and a turbulent sublayer (TSL) (*Corrsin and Kistler*, 1954; *Townsend and Taylor*, 1948). In the VSL, the vorticity in the turbulent region stretches to the irrotational region

by viscous diffusion (*Batchelor and Batchelor*, 1967), whereas the TSL is adjacent to the turbulent region, which is dominated by inertial effects. *da Silva and Taveira* (2010) studied the mean thickness of the mixing layer in planar turbulent jets, which scale as the Taylor microscale, λ, and is correlated with the radius of the large-scale eddies. In addition, large-scale motions induce entrainment, known as *engulfment*, where vorticity structures roll over the mixing layer towards the non-turbulent region and contribute to the mixing region growth. Therefore, the thickness of the layer is determined by the Taylor microscale (*Dimotakis*, 2000; *Bisset et al.*, 2002; *Gaskin et al.*, 2004; *Westerweel et al.*, 2005; *Hunt et al.*, 2006). On the other hand, some studies found that the *nibbling* process dispatches intense vortical structures (IVS) at small scales to the irrotational region by viscous diffusion, implying that the thickness of the TNTI corresponds to the Kolmogorov length scale η (*Mathew and Basu*, 2002; *Chauhan et al.*, 2014; *Breda and Buxton*, 2019; *Zecchetto and da Silva*, 2021). The characteristics that explain the growth of the mixing region in free-shear flows are still under debate due to the complex dynamics.

1.5 Shearless Turbulent Mixing

The presence of mean shear (or other forces) complicates the study of turbulence because the mean shear generates energy whose characteristics cause coupled interactions through nonlinear interactions. Shearless turbulence can be used to examine turbulent dynamics independently of mean forcing. Such flows with no mean shear can be generated in grid turbulence experiments or computational turbulent fields. When shearless turbulent flow is adjacent to non-turbulent flow (e.g., irrotational flow), mixing develops through the entrainment of large-scale eddies and viscous diffusion at small-scale eddies near the interface (*Townsend*, 1980; *Bhat and Narasimha*, 1996; *Hunt et al.*, 2006; *Bisset et al.*, 2002; *Mathew and Basu*, 2002; *Chauhan et al.*, 2014; *Zecchetto and da Silva*, 2021). Therefore, the thickness of the mixing layer

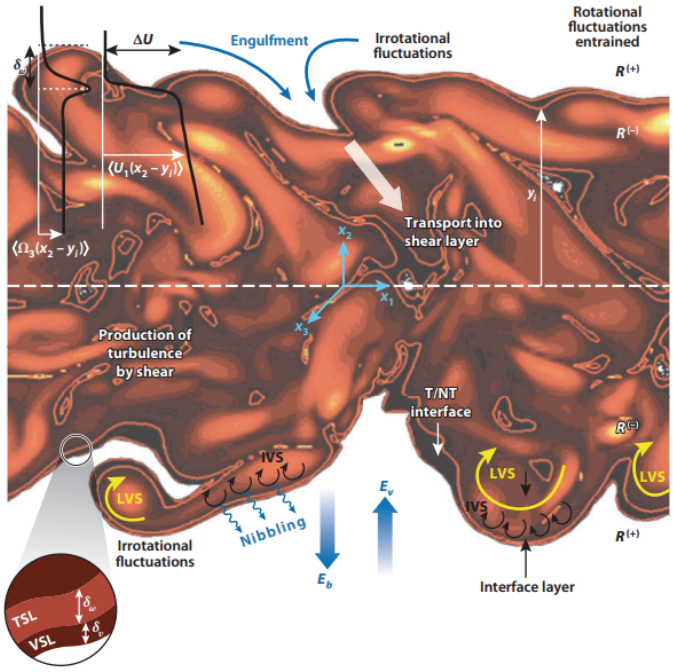

Figure 1.8: Schematic of turbulent/non-turbulent interface for a free-shear flow. Intense vorticity structures (IVS) and large-scale vortices (LVS) are observed near the interface, which consists of the viscous superlayer (VSL) and the turbulent sublayer (TSL). Reproduced from *Vassilicos* (2015), with the permission of the Annual Reviews.

is scaled by the Kolmogorov scale, whereas for the shear layer, it is correlated with the large vortical structures (*Holzner et al.*, 2007; *da Silva and Taveira*, 2010; *Silva et al.*, 2018). Additionally, *Veeravalli and Warhaft* (1989) investigated turbulent mixing layers between flows with different integral length scales and showed that the mixing occurs with strong intermittency and anisotropy. Turbulent diffusion plays a role in spreading the flow, resulting in non-Gaussian behavior in the mixing layer. Also, *Movahed and Johnsen* (2015) evaluated the role of density gradients on freely decaying turbulent mixing; they observed that turbulence is isotropic at the smallest scale (i.e., Kolmogorov scale), but anisotropic at intermediate scales (i.e., Taylor scale and larger). In the case of shearless turbulent mixing with gradients in turbulent intensity, *Tordella and Iovieno* (2011) investigated shearless turbulent mixing between fluids of different integral scales and kinetic energies at moderate Reynolds numbers ($Re_\lambda = 45 - 150$). They found that intermittency and skewness are caused by anisotropy in the gradients of the length scale and kinetic energy. In an experimental study of a shearless mixing layer initially composed of kinetic energy gradients, *Thormann and Meneveau* (2015) observed that large-scale intermittency is generated by the penetration of high-energy eddies. Consequently, the peak of flatness (i.e., the fourth-order statistics of velocity derivatives) appears in the low-energy region. The evolution of turbulent kinetic energy follows a power law in the streamwise distance, with the decay exponents depending on the turbulent intensity. However, the temporal decay of the turbulent kinetic energy and the mixing layer evolution in shearless turbulent flows with gradients in turbulent intensity are still not well understood. Furthermore, the effects of compressibility and geometry on turbulent mixing remain largely unexplored, as they are not accounted for in the classical theory of Kolmogorov.

1.6 Turbulence Models

Turbulence modeling is essential for predicting turbulent flows in various applications such as combustion, wall-bounded flows, weather forecast, and oceanic circulation because it is not feasible to simulate all the scales of turbulence due to the vast range of scales involved. These scales can extend from millimeters to meters or even kilometers in space, and from milliseconds to seconds or even days in time. Therefore, turbulence models are used to provide approximations and closure in turbulent flows, allowing for predictions to be made for engineering, atmospheric, and oceanic applications. DNS plays an important role in developing and improving turbulence modeling as it can provide insights into understanding the physics of fluid dynamics (*Moin and Mahesh*, 1998). Researchers have focused on developing turbulence modeling based on averaged characteristics of complex turbulent flows (*Rogallo*, 1981; *Rogers*, 1986; *Hunt et al.*, 1988; *Speziale*, 1991; *Shih*, 1997). DNS can also be used to validate and improve them and to directly test and provide accurate statistics (*Durbin*, 1991; *Rodi and Mansour*, 1993). Furthermore, it can be used to investigate and verify novel phenomenology in turbulence, which leads to the development of turbulence models (*Zeman*, 1990; *Parneix and Durbin*, 1996).

For analytical modeling, the turbulent stresses $\rho u_i^{'} u_j^{'}$ in Reynolds averaged Navier Stokes equations remain unknown and are determined by turbulence models. The fundamental approaches of turbulence modeling are the turbulent-viscosity and gradient-diffusion hypotheses (*Pope*, 2000). According to these hypotheses, the turbulent diffusivity and turbulent viscosity require specifications via modeling, such that the mean flow equations can be solved. For the turbulent-viscosity hypothesis, the Reynolds stresses are described as

$$\langle u_i u_j \rangle - \frac{2}{3} k \delta_{ij} = -\nu_T \left(\frac{\partial \langle U_i \rangle}{\partial x_j} + \frac{\partial \langle U_j \rangle}{\partial x_i} \right) \tag{1.7}$$

where U is the mean velocity, u the velocity fluctuation, k the kinetic energy, δ_{ij} the Kronecket delta, and ν_T the turbulent viscosity. The turbulent viscosity is written as $\nu_T \sim ul$ where l is the length scale in turbulence based on simple algebraic models such as the mixing-length model. On the other hand, the gradient-diffusion hypothesis defines the scalar equation by using the scalar flux vector $\left\langle \mathbf{u}\phi^{`} \right\rangle$ and the turbulent diffusivity Γ_T as

$$\left\langle \mathbf{u}\phi^{`} \right\rangle = -\Gamma_T \nabla \left\langle \phi \right\rangle \tag{1.8}$$

where ϕ is scalar. The diffusivity is determined by the velocity and time scales as $\Gamma_T \sim uT$, which can be related to the turbulent viscosity by the turbulent Prandtl number σ_T, i.e., $\Gamma_T = \nu_T/\sigma_T$. This approach is the simplest, where the mixing length and velocity u should be specified. The turbulent kinetic energy model is a one-equation model that scales the velocity component in Eq. (1.7) as the turbulent kinetic energy: $u = c_1 k^{1/2}$, where c_1 is a constant. The turbulent kinetic energy should be specified by solving the turbulent kinetic energy budget equations. In contrast, two-equation models use both turbulent kinetic energy and turbulent dissipation rate equations to close the problem.

Similarly, large eddy simulations (LES) reduce the computational cost by solving filtered Navier-Stokes equations. The LES filter is applied to a spatial and temporal field and removes a range of small scales, defined as sub-grid scales (SGS). Therefore, this method requires the modeling of unresolved SGS (*Pope*, 2000). The general filtering operation is defined as:

$$\overline{\mathbf{U}}(\mathbf{x}, t) = \int_{-\infty}^{\infty} G(\mathbf{r}, \mathbf{x}) \mathbf{U}(\mathbf{x} - \mathbf{r}, t) d\mathbf{r}, \tag{1.9}$$

where $\mathbf{U}(\mathbf{x}, t)$ is the spatial and temporal field, and G is the filter function, including

a cutoff length scale Δ. A residual field is defined as:

$$\mathbf{u}'(\mathbf{x},t) = \mathbf{U}(\mathbf{x},t) - \overline{\mathbf{U}}(\mathbf{x},t). \tag{1.10}$$

Note that this operator is different from the Reynolds decomposition; hence, $\overline{\mathbf{u}'} \neq 0$. To close the filtered equations, the anisotropic residual stress tensor should be modeled. It is defined as $\tau_{ij}^r = \tau_{ij}^R - \frac{2}{3}k_r\delta_{ij}$, where $\tau_{ij}^R = \overline{U_iU_j} - \bar{U}_i\bar{U}_j$ is the residual-stress tensor and $k_r = \frac{1}{2}\tau_{ij}^R$ is the residual kinetic energy.

The SGS fluctuations are correlated with the rate of turbulent energy transfer to smaller scales. Therefore, SGS models focus on the dissipation rate of energy, and use the linear eddy-viscosity model as follows:

$$\tau_{ij}^r = -2\nu_t\overline{S}_{ij}, \tag{1.11}$$

where $\bar{S}_{ij}$ is the filtered strain-rate tensor and ν_t is the eddy viscosity (*Pope*, 2000). SGS models have been developed to determine eddy viscosity. The Smagorinsky model was the first attempt to describe eddy viscosity as $\nu_t = (C_S\Delta)^2\overline{S}$, where the constant C_S is strongly dependent on the flow configuration. Furthermore, the dynamic model, also known as the dynamic Smagorinsky model (*Germano et al.*, 1991), improves the Smagroinsky model by dynamically determining local constants using two filters, which procedure enables simulating complex flows.

However, most turbulence models show discrepancies from DNS results, indicating that energy transfer from the large scales (resolved) to the small scales (unresolved) and dissipative mechanisms are not well described. Additionally, inhomogeneous compressible flows require consideration of additional energy transfer and dissipative mechanisms in turbulence models. Wall models of LES have been extensively studied to identify subgrid terms arising from inhomogeneity and anisotropy in wall-bounded flows. However, these models only examined the contribution of the mean strain rate

tensor to dissipation in the Smagorinsky eddy viscosity near the wall. Therefore, energy transfer in inhomogeneous and compressible turbulence should be considered in terms of kinetic energy and length scales to determine the eddy viscosity in LES.

1.7 Thesis Outline and Contributions

As introduced in this chapter, classical Kolmogorov theory cannot fully describe inhomogeneous compressible turbulence because this flow violates the assumptions of incompressibility, homogeneity, and in general isotropy. This thesis focuses on exploring compressible turbulent mixing with gradients in turbulent intensity, in flows with decaying turbulent kinetic energy (by contrast to forced turbulence), and the mixing region developing over time. Turbulent mixing involves various physical phenomena, such as entrainment, mass/momentum transfer, and diffusion, which are distinct from the behavior observed in homogeneous isotropic turbulence. Furthermore, in compressible turbulence, the presence of dilatation introduces additional mixing mechanisms that complicate the physics involved, requiring a modification of the conventional theory of turbulence. The hypotheses underlying this research are that compressibility and geometry (e.g., cylindrical vs. planar) inhibit mixing at gradients of turbulent intensity due to dilatational effects and diverging flows, respectively. Therefore, the objectives of this study are to investigate the role of compressibility and geometry on the evolution of turbulent kinetic energy and turbulent mixing in:

- Compressible turbulent/non-turbulent mixing in Chapter III. The study considers the case where shearless initially homogeneous and isotropic turbulent flow is adjacent to a stationary fluid. Direct numerical simulations are performed to investigate the development of mixing regions and the evolution of turbulent kinetic energy. The analysis focuses on the role of triple moments

of velocity fluctuations in the turbulent kinetic energy balance equation, which are not present in homogeneous and incompressible flow but expected to play an important role in inhomogeneous and compressible turbulence.

- Compressible turbulent mixing with gradients in turbulent intensity in Chapter IV. The study considers the case where shearless initially homogeneous and isotropic turbulent flows are juxtaposed with different intensities. Direct numerical simulations are performed to investigate energy transfer across the interface. The analysis focuses on intermittency and energy loss/gain caused by compressibility effects, which delay or enhance the decay rate of turbulent kinetic energy.

- Compressible turbulent/non-turbulent mixing in a cylindrical geometry in Chapter V. The study considers the case where shearless initially homogeneous and isotropic turbulent flow has planar and cylindrical shapes with different intensities. Direct numerical simulations are performed to investigate the geometrical effects on the development of mixing regions and the evolution of turbulent kinetic energy. The analysis focuses on the role of dilatation, which generates energy loss larger through the diverging interfaces.

This work contributes to a better understanding of turbulent mixing in terms of:

- Improving the process of generating initial turbulent velocity fields

- Determining the decay rate of turbulent kinetic energy for turbulent/non-turbulent and turbulent/turbulent mixing based on the parameters governing the problem (initial root-mean-squared velocity, Taylor microscale, and dilatation)

- Discovery of intermittency with non-Gaussian behavior, demonstrating compressibility effect

- Scaling of mixing region growth in time in turbulent/non-turbulent mixing and turbulent/turbulent mixing
- Scaling of dilatation in time in turbulent/non-turbulent mixing and turbulent/turbulent mixing
- Extension of the present theory for planar turbulent fronts to cylindrical.

CHAPTER II

Physical Model

In this chapter, we present the governing equations along with the numerical details. An improved method for generating a fully developed initial turbulent field is demonstrated to achieve an equilibrium state.

2.1 Governing Equations and Numerical Details

We perform direct numerical simulation (DNS) and solve the three-dimensional compressible Navier-Stokes equations for an ideal gas:

$$\frac{\partial \rho}{\partial t} + \frac{\partial}{\partial x_j}(\rho u_j) = 0 \tag{2.1}$$

$$\frac{\partial (\rho u_i)}{\partial t} + \frac{\partial}{\partial x_j}(\rho u_i u_j + p\delta_{ij}) = \frac{1}{Re}\frac{\partial \tau_{ij}}{\partial x_j} \tag{2.2}$$

$$\frac{\partial E}{\partial t} + \frac{\partial}{\partial x_j}[u_j(E+p)] = \frac{1}{Re}\left[\frac{\partial (u_j \tau_{ij})}{\partial x_j} + \frac{\partial}{\partial x_j}\left(\kappa_T \frac{\partial T}{\partial x_j}\right)\right] \tag{2.3}$$

$$p = \rho R T. \tag{2.4}$$

We additionally solve a transport equation to analyze mixing:

$$\frac{\partial (\rho Y_i)}{\partial t} + \frac{\partial (\rho u_j Y_i)}{\partial x_j} = \frac{1}{ReSc}\frac{\partial}{\partial x_j}\left(\rho \frac{\partial Y_i}{\partial x_j}\right). \tag{2.5}$$

Here, $E = \rho\left(e + u_i u_i/2\right)$ is the total energy per unit volume, $e = p/\left(\rho(\gamma-1)\right)$ the internal energy per unit mass, ρ the density, u_j the velocity, p the pressure, T the temperature, κ_T the thermal conductivity, γ the specific heats ratio, R the gas constant, Sc the Schmidt number, D the mass diffusivity, and Y_i the mass fraction of fluid $i = 1$ *or* 2. The specific heat ratio and Schmidt number are set to $\gamma = 1.4$ and $Sc = 1$, respectively. The scaled Reynolds number Re and viscous stress tensor τ_{ij} are defined as follows:

$$Re_{\lambda_0} = Re\left[\frac{\rho u_{rms_0}\lambda_0}{\mu}\right], \tag{2.6}$$

$$\tau_{ij} = \mu\left[\left(\frac{\partial u_i}{\partial x_j} + \frac{\partial u_j}{\partial x_i}\right) - \frac{2}{3}\frac{\partial u_k}{\partial x_k}\delta_{ij}\right]. \tag{2.7}$$

where λ_0 is the initial Taylor microscale, u_{rms_0} the initial root-mean-square velocity, and μ the dynamic viscosity. These equations are non-dimensionalized by the parameters of the initial HIT with $u_{ref} = 1$, $\rho_{ref} = 1$, and $l_{ref} = L/(2\pi)$. We use an explicit fourth-order Runge-Kutta scheme and high-order finite differences (sixth-order explicit central differences) in time and space, respectively, to discretize the governing equations. The flow under consideration has $Ma_t < 0.4$, so that no shocklets are produced (*Passot and Pouquet*, 1987; *Lee et al.*, 1991; *Benzi et al.*, 2008). Therefore shock capturing or artificial dissipation is not required. The split form is applied to the convective fluxes based on the form of *Blaisdell et al.* (1996):

$$\frac{\partial}{\partial x_j}\left(\rho u_j \phi\right) = \frac{1}{2}\left[\frac{\partial}{\partial x_j}\left(\rho u_j \phi\right) + u_j \frac{\partial}{\partial x_j}\left(\rho\phi\right) + \rho\phi\frac{\partial u_j}{\partial x_j}\right]. \tag{2.8}$$

Here, $\phi = (1,\ u_i,\ (E+p)/\rho,\ Y_i)$, and the flux of *Ducros et al.* (2000) is implemented. The non-conservative form is used for discretizing the diffusive terms:

$$\frac{\partial}{\partial x_j}\left(\mu\frac{\partial u_j}{\partial x_j}\right) = \mu\frac{\partial^2 u_j}{\partial {x_j}^2} + \frac{\partial \mu}{\partial x_j}\frac{\partial u_j}{\partial x_j}. \tag{2.9}$$

2.2 Dimensional Analysis

Turbulent mixing arises from the interaction of various physical parameters as a result of the misaligned properties and their spatial and temporal variations. Dimensional analysis helps understand the physics of mixing by examining the dimensions of physical parameters and their correlations. This is facilitated by dimensionless groups and scaling relationships, which simplify complex problems.

The key parameters in this work are the turbulent intensity, the turbulent length scale, the speed of sound, and viscosity, which are determined as the initial root-mean-squared velocity u_{rms_0}, the most energetic wave number k_0 or the initial Taylor microscale λ_0, the speed of sound $c = \sqrt{\gamma p/\rho}$, respectively. The viscosity ν is represented as the scaled Reynolds number in Eq. (2.6). These parameters introduce the primary dimensionless quantities that are Reynolds and turbulent Mach numbers. As the pressure is initially uniform as $p_0 = 4\pi L\rho$, the speed of sound is initially invariant (*Dimonte et al.*, 2004); therefore, the dimensionless quantities can describe flow parameters as follows:

$$u_{rms_0} = Ma_{t_0} \times \sqrt{\frac{\gamma p}{\rho}}, \tag{2.10}$$

$$Re = \frac{Re_{\lambda_0}}{\rho u_{rms_0} \lambda_0/\mu}, \tag{2.11}$$

where $\lambda_0 = 2/k_0$ and $\mu = 1$. For turbulent mixing, each field has its own u_{rms_0}, k_0 or λ_0, and c. In this study, we set the scaled Reynolds number, the speed of sound, and k_0 to be the same for each fluid, such that the changes in Reynolds and turbulent Mach numbers induce differences in u_{rms_0}. Therefore, this dimensional analysis isolates the effect of gradients in turbulent intensity.

2.3 Initialization of Turbulent Velocity Field

We present our rescaling procedure for the initial velocity field to produce an equilibrium turbulence state from $t = 0$. Initialization of the solenoidal velocity field with a Batchelor spectrum has been widely used for generating homogeneous isotropic turbulence (*Batchelor and Proudman*, 1956; *Lee et al.*, 1991; *Johnsen et al.*, 2010). A detailed procedure to generate the initial velocity field in terms of Fourier coefficients is described in *Johnsen et al.* (2010), with the Fourier transform represented as follows:

$$\hat{\mathbf{u}}_{\mathbf{k}} = \frac{1}{N} \sum_{j=0}^{N-1} u_j \left(\mathbf{x}\right) e^{-i\frac{2\pi j}{N}k}, \tag{2.12}$$

where u_j are the velocity components in a real vector space, N is the number of grid points, and k is the wavenumber.

However, the key issue with the resulting flow is that it takes finite time to evolve to an equilibrium state of turbulence; additionally, there is no clear relationship between the properties (Taylor scale, rms velocity) at that time in terms of those of the initial field. Fig. 2.1(a-b) shows energy spectra at $t = 0\tau$ and $t = 2\tau$ where $\tau = \lambda_0/u_{rms_0}$ is the eddy turnover time and the time evolution of the volume-averaged enstrophy for decaying homogeneous isotropic turbulence in a periodic box with a random solenoidal velocity field. As expected, the initial field does not have a -5/3 slope and does not contain a broad range wavenumbers. It takes a few eddy turnover times for the energy to get distributed over a broad range of wavenumbers; this initial transient is observable in the enstrophy in Fig. 2.1(c), which initially increases before reaching a maximum and, as the turbulence is developed, decreasing. We propose to take the velocity field at 2τ and rescale it to use it as our initial conditions with the desired Reynolds number because it is the field with the highest energy in the equilibrium state. Our process is based on the following steps:

Step 1. We define the most energetic wavenumber at $t = 0\tau$ and 2τ as k_0 and k^*,

respectively, and the difference between these two wavenumbers at $t = 0\tau$ and 2τ as the shift wavenumber, $k_s = k_0 - k^*$.

Step 2. To set the initial wavenumber with the highest energy contents to be the same as that of the random solenoidal velocity field, we shift the velocity components, v_j:

$$v_j(\mathbf{x}) = u_j(\mathbf{x})\, e^{i\frac{2\pi j}{N}k_s}. \tag{2.13}$$

Step 3. The Fourier transform of v_j can be performed as follows.

$$\hat{\mathbf{v}}_\mathbf{k} = \frac{1}{N}\sum_{j=0}^{N-1} v_j(\mathbf{x})\, e^{-i\frac{2\pi j}{N}k} = \frac{1}{N}\sum_{j=0}^{N-1} u_j(\mathbf{x})\, e^{-i\frac{2\pi j}{N}(k-k_s)}. \tag{2.14}$$

Step 4. We perform an inverse Fourier transform and set the magnitude of the root-mean-squared velocity to u_{rms}, thus producing the new rescaled velocity field.

This rescaling process produces an equilibrium turbulence field with the desired initial properties (Reynolds number, most energetic wavenumber). In Fig. 2.1(a-b), we observe that our rescaled initial field exhibits the expected $k^{-5/3}$ spectrum from the beginning over a wide range of wavenumbers. The spectral energy of the original initial field decays faster than that of the rescaled field in all ranges of wavenumbers because the original initial field starts decaying before reaching an equilibrium state of turbulence. We do observe an initial transient in enstrophy in the rescaled field with our procedure (10% compared to the initial state), though the enstrophy magnitude of the original approach at $t = 2\tau$ evolves to be 200% more of the initial enstrophy. In Fig. 2.1(d), the Reynolds number at $t = 2\tau$ for the original initial field is less than 50, which is significantly lower than the desired initial value of $Re_{\lambda_0} = 100$. Therefore, the rescaled field allows us to obtain correct turbulent statistics and achieve higher Re_{λ_0} at $t = 0\tau$ and describes the quasi-equilibrium state from the beginning with desired properties.

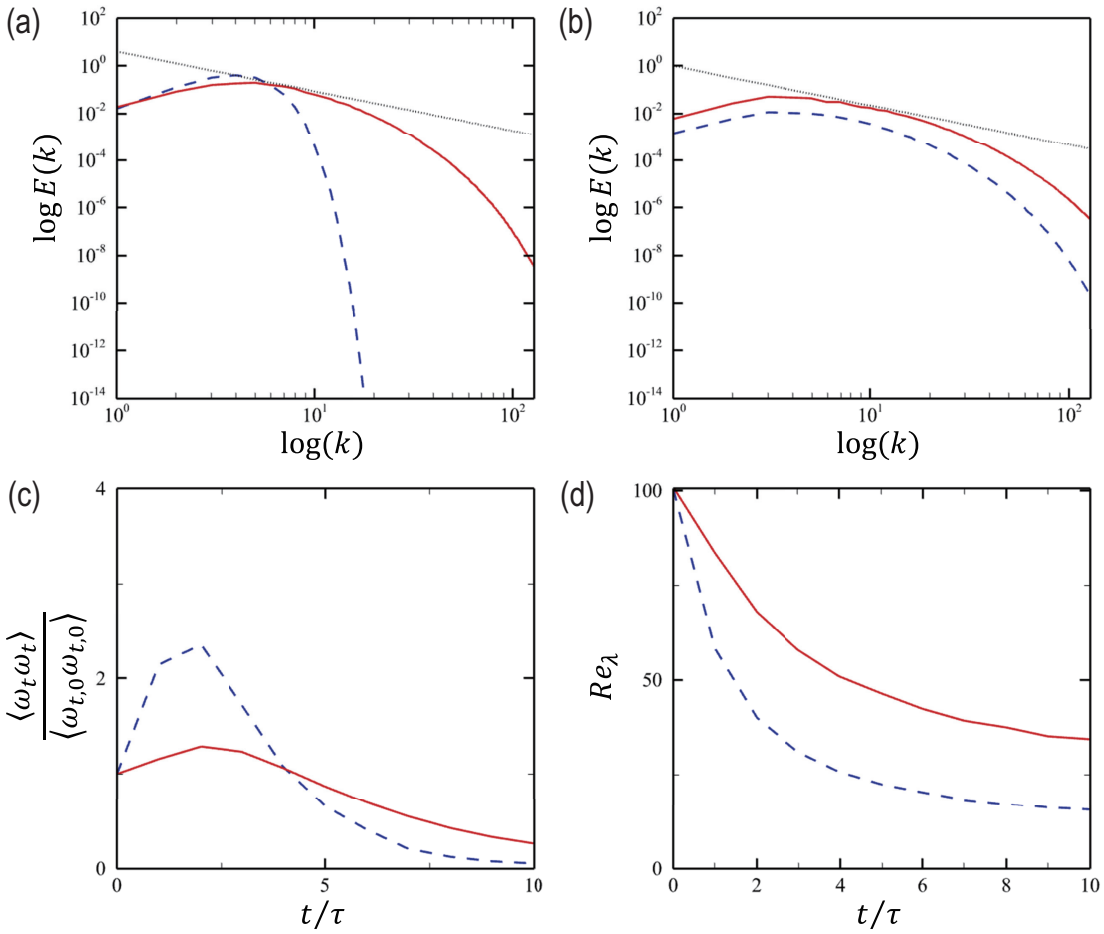

Figure 2.1: Energy spectra at (a) $t = 0\tau$, (b) $t = 2\tau$, (c) temporal evolution of enstrophy, and (d) Reynolds number for the single homogeneous isotropic turbulence in a periodic box. The turbulent kinetic energy is randomly distributed in the previous solenoidal velocity field with a Batchelor spectrum (dashed line). The solid line is obtained by applying the rescaling process. The dotted line represents the Kolmogorov scaling of $E(k) \sim k^{-5/3}$. All simulations are conducted in a cube box of $L = 2\pi$ with $256/L$ grid points for $Re_{\lambda_0} = 100$ and $Ma_{t_0} = 0.1$.

CHAPTER III

Decaying Compressible Turbulence Adjacent to an Irrotational Flow Region

3.1 Abstract

Shearless turbulent/non-turbulent mixing has primarily been studied in the incompressible limit. In this work, we investigate the role of compressibility on turbulent/non-turbulent mixing with no mean shear. We consider an initially isotropic region of turbulence next to a stationary fluid and seek to predict the evolution of the mixing region width and the turbulent kinetic energy using theory and direct numerical simulation. We find that the mixing region grows as a power law in time consistent with past theory for incompressible flow ($\sim t^{2/3}$). However, we demonstrate that the turbulent kinetic energy is affected by energy transport away from the mixing region due to dilatation, in addition to viscous dissipation. We establish the dependence of the turbulent kinetic energy on time and on the parameters governing the problem (Taylor scale, rms velocity, and initial dilatation). Compared to the incompressible case, dilatation gives rise to an increased decay rate of turbulent kinetic energy.

3.2 Introduction

At a sufficiently high Reynolds number in the incompressible limit, the classical Richardson-Kolmogorov theory describes the dynamics, energy transfer, and mixing of homogeneous, isotropic turbulence (*Kolmogorov*, 1941a,b, 1962). Under these conditions, turbulent eddies produced in the energy-containing range break up into ever smaller eddies until the corresponding Reynolds number is sufficiently small that differentials in viscous stresses dissipate the kinetic energy. Decaying homogeneous isotropic turbulence (HIT) has been extensively investigated (*Veeravalli and Warhaft*, 1989; *George*, 1992; *Stalp et al.*, 1999; *Hughes et al.*, 2001; *Donzis et al.*, 2005; *Krogstad and Davidson*, 2011) and well-known laws describing the time-evolution of key quantities such as the turbulent kinetic energy or length scales have been developed (*Batchelor and Townsend*, 1948a,b; *Corrsin*, 1951; *Mansour and Wray*, 1994; *Wang and George*, 2002; *Ishida et al.*, 2006; *George and Wang*, 2009; *Esteban et al.*, 2019; *Panickacheril John et al.*, 2022). Under such conditions, the energy equation can be written as

$$\frac{dK}{dt} = \dot{\epsilon}, \tag{3.1}$$

where $K = \langle u_i u_i \rangle / 2$ is the total TKE per mass, u_i the velocity fluctuations, $\langle \cdot \rangle$ volume-averaged quantities, t time, and $\dot{\epsilon}$ the volume-averaged dissipation rate (*Batchelor and Proudman*, 1956; *Comte-Bellot and Corrsin*, 1966). By scaling the dissipation rate by the energy-containing length scale ($\dot{\varepsilon} \sim K^{3/2}/\mathcal{L}$ where $\mathcal{L}$ is integral scale), the turbulent kinetic energy can be expressed as a power law in time (*Batchelor*, 1953; *Saffman*, 1967; *Gad-el Hak and Corrsin*, 1974; *Lee*, 1985; *Mohamed and LaRue*, 1990; *Burattini et al.*, 2006). For the decay of fully developed turbulence, conservation of angular momentum depends on the initial field; $u^2 l^5$ or $u^2 l^3$ is an invariant depending on whether a Batchelor or a Saffman spectrum is used, respectively, thus yielding different exponents for decaying turbulent kinetic energy, especially $a = -10/7$ for

Kolmogorov's law and $-6/5$ for Saffmans's law. However, the exponent of the decay law is still under debate because it depends on experiment setups, e.g., types of grid (*Batchelor and Townsend*, 1948a,b; *Chasnov*, 1994; *Briggs et al.*, 1996; *Lavoie et al.*, 2007; *Valente and Vassilicos*, 2012; *Djenidi et al.*, 2015). Moreover, these decay exponents are obtained for long time periods for forced turbulence; hence other quantities may play a role in decay, for instance, properties of the initial field. On the other hand, *George and Wang* (2009) described the decay as exponential in flows in which length scales are independent of time and the ratio of the integral length scale to the Taylor microscale is constant. This behaviour has also been observed in space-filling fractal grid experiments (*Seoud and Vassilicos*, 2007; *Hurst and Vassilicos*, 2007).

In nature and engineering, many turbulent flows are heterogeneous, such that a region of turbulent flow is adjacent to a non-turbulent region, possibly separated by a temporally growing mixing region. For instance, for problems such as air-sea interfaces, dry air near clouds, and instabilities along jets, a mixing zone develops between turbulent and non-turbulent regions and grows with time (*Garwood Jr*, 1979; *Andrejczuk et al.*, 2004; *Dimotakis*, 1991). In free-shear flows such as jets and wakes, the mean shear continuously feeds energy into the system, thereby sustaining turbulence. To better understand mixing independently of shear, researchers have examined shearless turbulence. In wind-tunnel experiments, nearly shearless turbulence can be generated by passing the flow through a grid, while in numerical simulations a random velocity field can be set up to develop into shearless homogeneous isotropic turbulence (*Veeravalli and Warhaft*, 1989; *Kang and Meneveau*, 2008; *Tordella and Iovieno*, 2011; *Ireland and Collins*, 2012; *Isaza et al.*, 2014; *Thormann and Meneveau*, 2015). Shearless turbulent mixing can be studied by co-flowing fluids with different turbulent properties (e.g., Reynolds number, length scale, intensity) in a planar configuration. Owing to the inhomogeneity of the flow, classical Kolmogorov theory does not immediately apply and must be modified (*Launder et al.*, 1973; *Haworth*

and Pope, 1987; *Yoder et al.*, 2015; *Buxton et al.*, 2019). A special case of shearless turbulent mixing is turbulent/non-turbulent mixing. *Corrsin and Kistler* (1954) first examined turbulent/non-turbulent interfaces (TNTIs). Mixing layers involve different dynamics at large- and small-scale. Large eddies near the TNTI entrain patches of irrotational flow through *engulfment*; the size of the mixing region as measured by vortical contents therefore strongly depends on this process (*Townsend*, 1980; *Bhat and Narasimha*, 1996; *Dimotakis*, 2000; *Gaskin et al.*, 2004; *Hunt et al.*, 2006; *Westerweel et al.*, 2009; *Bisset et al.*, 2002; *Lee et al.*, 2017). At smaller scales, viscous stresses impart vorticity to irrotational patches of fluid via *nibbling* (*Mathew and Basu*, 2002; *da Silva and dos Reis*, 2011; *Chauhan et al.*, 2014; *Breda and Buxton*, 2019; *Zecchetto and da Silva*, 2021). Viscous dissipation has been shown to affect the entrainment process (*Corrsin and Kistler*, 1954; *Westerweel et al.*, 2005; *Holzner et al.*, 2007); therefore, the dissipation rate and vorticity exhibit peaks within the mixing layer (*Teixeira and da Silva*, 2012). However, whether large- or small-scale flow features contribute the most to turbulent/non-turbulent mixing is still under debate (*da Silva et al.*, 2014a).

The thickness of the TNTI can be identified by a sharp decrease in vorticity and correlates to the length scale of the vorticity structures near the interface (*da Silva and Taveira*, 2010). The thickness has been postulated to be proportional to the Taylor microscale and Kolmogorov scale for shear and shear-free flows, respectively (*Bisset et al.*, 2002; *Holzner et al.*, 2007; *da Silva and Taveira*, 2010; *Silva et al.*, 2018). However, the temporal evolution of the mixing layer and turbulent kinetic energy (TKE) in turbulent/non-turbulent mixing has yet to be considered. *Barenblatt et al.* (1987) theoretically investigated the scaling of turbulent *bursts* starting with a finite thickness. Based on the dimensional analysis in the incompressible limit, he found that the mixing region thickness $h \sim t^{2/3}$ for $h(t) \ll h_0$, where h is the thickness of the mixing layer and h_0 is the initial thickness. The asymptotic solution has a different

exponent in time, which can be found by solving a nonlinear eigenvalue problem.

Investigations of turbulent/non-turbulent mixing have yet to take into account the role of compressibility. In compressible flow, acoustic, vortical, and entropy modes can interact with each other, giving rise to different dynamics and energy transport compared to the incompressible case (*Lele*, 1994). The ratio of dilatational to solenoidal root-mean-square (rms) velocities (δ) enables one to obtain universal scaling and better understand physics in compressible turbulence by acquiring statistical equilibria in the new parameter space of $\delta - Ma_t$ (*Donzis and John*, 2020). *Aluie* (2011) demonstrated the existence of a universal inertial range in compressible turbulence, which offers the possibility of scaling compressible flow according to the Kolmogorov theory. Also, a universal scaling method for energy spectra in compressible turbulent mixing was found using only solenoidal components resulting from Helmholtz decomposition (*John et al.*, 2019). Dilatation can affect the solenoidal velocity field by generating fluctuations in variables through acoustic waves (*Pan and Johnsen*, 2017). *Jagannathan and Donzis* (2016) suggested a scaling method for stationary compressible turbulence using the Reynolds and turbulent Mach numbers and showed that kinetic energy, pressure, and dilatation depend on the turbulent Mach number and follow a power law behavior in time. However, the implications of these compressibility effects on turbulent mixing, including turbulent/non-turbulent mixing, are currently unknown.

To address this gap, we investigate shearless turbulent/non-turbulent mixing where the turbulence is decaying and compressible. We develop scalings for turbulent kinetic energy decay and the time evolution of the mixing region thickness. These scalings are verified by DNS of decaying turbulence of different initial intensities juxtaposed with an initially staionary fluid with the same properties. We find that dilatational effects modify the TKE transport and that the resulting behavior can be quantified by accounting for these dilatational motions in the TKE transport equation. Addi-

tionally, an improved method for generating a fully developed initial turbulent field is presented. The remainder of the paper is organized as follows. The problem setup and governing equations are described in detail in Section 3.3. The flow dynamics at the turbulent/non-turbulent interface are examined in Section 3.4, and the turbulent kinetic energy evolution is analyzed in Section 3.5. Finally, our article ends with conclusions and recommendations for future studies.

3.3 Formulation of the Problem and Governing Equations

3.3.1 Formulation of the Problem and Initialization

To examine shearless turbulent/non-turbulent mixing, we consider the juxtaposition of an initially isotropic turbulent field with an initially quiescent field of the same fluid (i.e., the same thermodynamic and transport properties) and examine the subsequent evolution of this flow, which is effectively one dimensional in the mean (i.e., planar). The initial turbulent field can be described by its Taylor microscale λ_0, Taylor-based Reynolds number Re_{λ_0}, and turbulent Mach number Ma_{t_0}. The initial rms velocity is u_{rms}. In this work, we use theoretical analysis and DNS.

The method of *Rogallo* (1981) and *Lee et al.* (1991) is a common approach to initialize simulations of decaying homogeneous isotropic turbulence (HIT). In this method, a random solenoidal velocity field is prescribed with a given spectrum, e.g., for the Batchelor spectrum $E(k) \sim k^4/{k_0}^4 exp(-2k^2/{k_0}^2)$, where k_0 is the most energetic wavenumber, in a periodic cubic box of size $L = 2\pi$, and evolves to equilibrium turbulence. A drawback of this approach is the difficulty in establishing a relationship between the initial condition and the time when the turbulence achieves an equilibrium state or even the properties of the turbulence (Taylor scale, rms velocity) at that time. To address this difficulty, we develop a rescaling approach to initialize the problem such that the initial field is in equilibrium turbulence with well-defined

properties (Taylor scale, Reynolds number, and turbulent Mach number). As explained in greater detail in Appendix A, the initial random field is evolved for two eddy turn-over times τ until equilibrium turbulence is achieved. In Fourier space, the wavenumber is shifted by the difference between the initial field and the equilibrium field at 2τ before performing the inverse transformation. Finally, the rms value can be scaled to the desired value. This rescaled field with desired properties allows one to examine the equilibrium turbulent field with desired properties from $t = 0$, rather than having to wait a few eddy turnover times for a flow whose state is not clearly connected to the initial random field.

The computational domain is shown in Fig. 5.1. We juxtapose four cubic boxes of initially isotropic turbulence and another four cubic periodic boxes of the same fluid with zero velocity in the inhomogeneous direction z. The turbulent/non-turbulent interface is initially located at the center of the domain at $z = 0$. Periodic boundary conditions are used in the x- and y-direction, while zero gradient conditions are applied in the inhomogeneous direction at the domain end. The domain size of $8L$ is large enough to ensure that boundary effects do not influence the dynamics. A uniform grid is used with $N_{grid}/L = 256$, which is small enough to resolve all physics in turbulence.

The turbulence dynamics in the present problem are primarily governed by three dimensionless quantities: the initial Taylor-based Reynolds number $Re_{\lambda_0} = u_{rms}\lambda_0/\nu$, initial turbulent Mach number $Ma_{t_0} = u_{rms}/c$, and initial scaled Taylor microscale λ_0/L, where ν and c are the kinematic viscosity and the speed of sound, respectively. To understand the dependence of the turbulence dynamics on the governing parameters and to verify the analysis, we conduct a series of simulations described in Table 5.1. We consider initial Reynolds numbers varying between 100 and 215 such that the turbulence is initially fully developed according to *Dimotakis* (2000) and turbulent Mach numbers varying between 0.1 and 0.3. For this range of $Ma_{t,0}$, no shocklets are

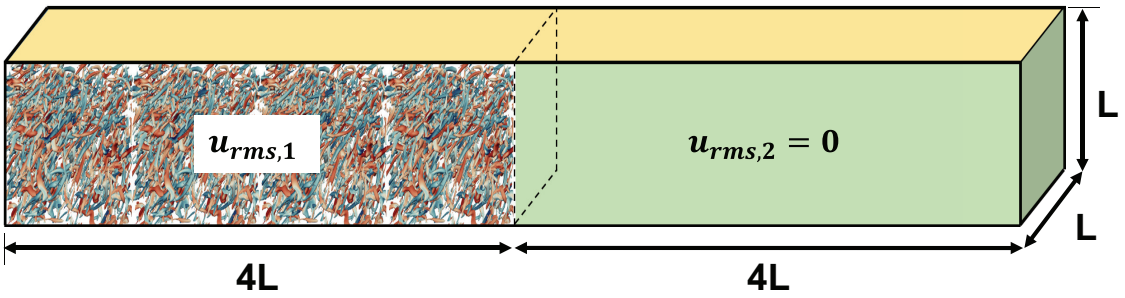

Figure 3.1: Schematic of the initial problem setup. The initial turbulent velocity field of intensity $u_{rms,_1}$ is juxtaposed to irrotational flow (green) with $u_{rms,_2} = 0$.

	$u_{rms,_1}$	$u_{rms,_2}$	$\lambda_{0,_1}/L$	$Re_{\lambda_{0,_1}}$	$Ma_{t_{0,_1}}$
case1	1	0	0.25	100	0.1
case2	2	0	0.20	160	0.2
case3	3	0	0.18	215	0.3
case4	1	0	0.25	160	0.1

Table 3.1: Summary of the simulations and relevant parameters.

produced. The dependence on the temperature and gas constant, which is expected to be negligible, is beyond the scope of the present study.

3.3.2 Governing Equations

In our simulations, We numerically solve the three-dimensional compressible Navier-Stokes equations for a perfect gas:

$$\frac{\partial \rho}{\partial t} + \frac{\partial}{\partial x_j}(\rho u_j) = 0 \tag{3.2}$$

$$\frac{\partial (\rho u_i)}{\partial t} + \frac{\partial}{\partial x_j}(\rho u_i u_j + p\delta_{ij}) = \frac{1}{Re}\frac{\partial \tau_{ij}}{\partial x_j} \tag{3.3}$$

$$\frac{\partial E}{\partial t} + \frac{\partial}{\partial x_j}[u_j(E+p)] = \frac{1}{Re}\left[\frac{\partial (u_j \tau_{ij})}{\partial x_j} + \frac{\partial}{\partial x_j}\left(\kappa_T \frac{\partial T}{\partial x_j}\right)\right] \tag{3.4}$$

with the ideal gas law:

$$p = \rho RT \tag{3.5}$$

where $E = \rho\left(e + u_i u_i/2\right)$ is the total energy per unit volume, $e = p/\left(\rho(\gamma - 1)\right)$ the internal energy per unit mass, ρ the density, u_j the velocity, p the pressure, T the temperature, κ_T the thermal conductivity, γ the specific heats ratio, R the gas constant, and Re the scaled Reynolds number,

$$Re_{\lambda_0} = Re\left[\frac{\rho u_{rms}\lambda_0}{\mu}\right]. \tag{3.6}$$

We set the specific heat ratio is $\gamma = 1.4$. The gas is Newtonian with viscous stress tensor τ_{ij}:

$$\tau_{ij} = \mu\left[\left(\frac{\partial u_i}{\partial x_j} + \frac{\partial u_j}{\partial x_i}\right) - \frac{2}{3}\frac{\partial u_k}{\partial x_k}\delta_{ij}\right]. \tag{3.7}$$

Additionally, we solve a transport equation for a passive scalar for analysis purposes:

$$\frac{\partial(\rho Y_i)}{\partial t} + \frac{\partial(\rho u_j Y_i)}{\partial x_j} = \frac{1}{ReSc}\frac{\partial}{\partial x_j}\left(\rho\frac{\partial Y_i}{\partial x_j}\right) \tag{3.8}$$

where $Sc = \mu_1/\rho_1 D$ is the Schmidt number, D the scalar diffusivity, and Y_i the mass fraction of fluid $i = 1$ *or* 2. In this study, the kinematic viscosity and the scalar diffusivity are equivalent, i.e., $Sc = 1$. These equations are nondimensionalized with the reference properties, $u_{ref} = 1$, $\rho_{ref} = \rho_1$, and $l_{ref} = L/(2\pi)$.

We use high-order finite differences on a uniform grid to solve the equations in space. Since the turbulent Mach numbers are low enough that no shocklets are produced, shock capturing is not necessary. The diffusive terms are expressed in non-conservative form and the split forms suggested by *Blaisdell et al.* (1996) along with the flux of *Ducros et al.* (2000) are applied to prevent energy pileup at high

wavenumbers,

$$\frac{\partial}{\partial x_j}\left(\rho u_j \phi\right) = \frac{1}{2}\left[\frac{\partial}{\partial x_j}\left(\rho u_j \phi\right) + u_j \frac{\partial}{\partial x_j}\left(\rho\phi\right) + \rho\phi\frac{\partial u_j}{\partial x_j}\right], \tag{3.9}$$

where $\phi = (1,\ u_i,\ (E+p)/\rho,\ Y_i)$. Sixth-order explicit central differences are used for all spatial derivatives and an explicit fourth-order Runge-Kutta scheme is applied for time marching.

3.3.3 Decaying Homogeneous Isotropic Turbulence

As a starting point, we consider freely decaying, homogeneous isotropic turbulence. The TKE decays according to the dissipation rate,

$$\frac{d\left\langle k\right\rangle}{dt} = -\langle\varepsilon\rangle, \tag{3.10}$$

where k is the TKE per unit mass, and $\langle\cdot\rangle$ is the spatial volume-averaged quantity. The dissipation rate

$$\langle\varepsilon\rangle \sim \nu\frac{\langle u_i u_i\rangle}{\lambda^2}, \tag{3.11}$$

where λ is the time-dependent Taylor microscale:

$$\lambda^2 = \frac{\langle u_i u_i\rangle}{\left\langle\left(\frac{\partial u_i}{\partial x_i}\right)^2\right\rangle}. \tag{3.12}$$

Under equilibrium turbulence, large-scale eddies break up into ever smaller eddies whose kinetic energy is dissipated by differentials in viscous stresses once they are small enough. For freely decaying turbulence, eddies whose sizes are significantly larger than the Kolmogorov scale (e.g., Taylor scale) can be assumed to be invariant in time *Davidson* (2015), i.e. $\lambda \simeq \lambda_0$. Therefore, the TKE decays exponentially at

early times at a sufficiently high Reynolds number,

$$\frac{\langle k \rangle}{\langle k_0 \rangle} = \exp\left[-\frac{c_k}{Re_{\lambda_0}}\left(t/\tau_0\right)\right] \tag{3.13}$$

where c_k is a constant and $\tau_0 = \lambda_0/u_{rms_0}$ is the initial eddy turnover time. Fig. 3.2 shows the temporal decay of TKE for homogeneous isotropic turbulence for initial Reynolds numbers 100, 160, and 215. A transient appears at early times ($t < 2\tau$) because it takes a finite time for the constant initial pressure and density to reach an equilibrium state. Thereafter, the TKE decays exponentially for all Reynolds numbers. This result is consistent with that of *George and Wang* (2009). At sufficiently high Reynolds numbers, the dissipation rate becomes independent of Reynolds number. Fig. 4.3 shows the dissipation quantity, $c_\varepsilon = \langle \epsilon \rangle L_f/u^3_{rms_0}$ where L_f is the volume-averaged integral scale for different Reynolds numbers considered in this study, with comparison to other experiments and simulations. As expected, the dissipation quantity approaches a constant value (*Sreenivasan*, 1998; *Vassilicos*, 2015), thereby showing that our simulations at $Re_{\lambda_0} = 160 and 240$ are expected to exhibit the behaviour described by Eq. 3.13. However, because we are considering decaying turbulence, the case $Re_{\lambda_0} = 100$ may show Reynolds-number dependence, particularly at late times. Our results are consistent with those from past computational studies (*Jiménez et al.*, 1993; *Wang et al.*, 1996; *Yeung and Zhou*, 1997; *Cao et al.*, 1999). At relatively low Reynolds numbers, the dissipation quantity c_ε decreases with increasing Reynolds numbers and tends to a constant beyond $Re_{\lambda_0} \approx 100$, which corresponds to the mixing transition (*Dimotakis*, 2000). Discrepancies are attributed to initialization and forcing. We find empirically that the dissipation quantity determines the constant c_k in the Eq. (3.13) as $c_k \approx c_\varepsilon Re_{\lambda_0}/3$.

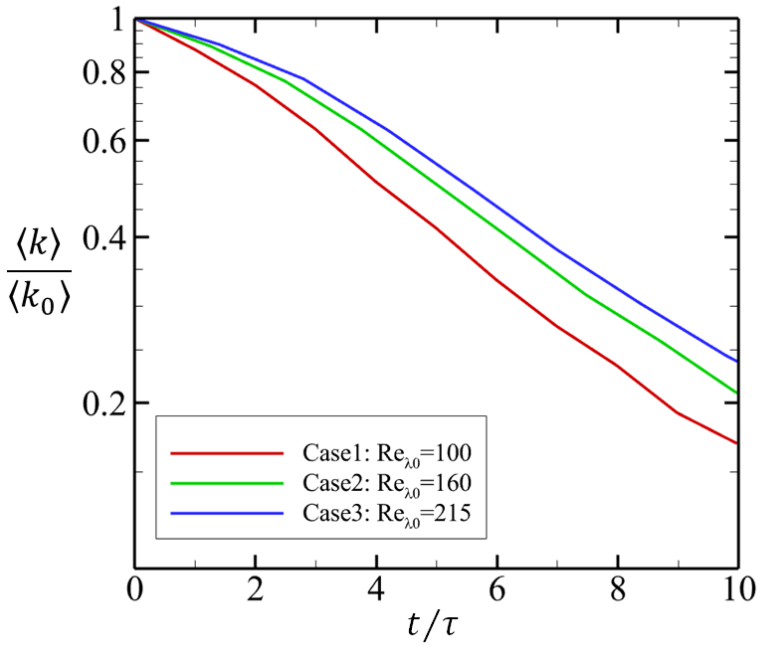

Figure 3.2: Time evolution of the turbulent kinetic energy in homogeneous isotropic turbulence for different Reynolds numbers.

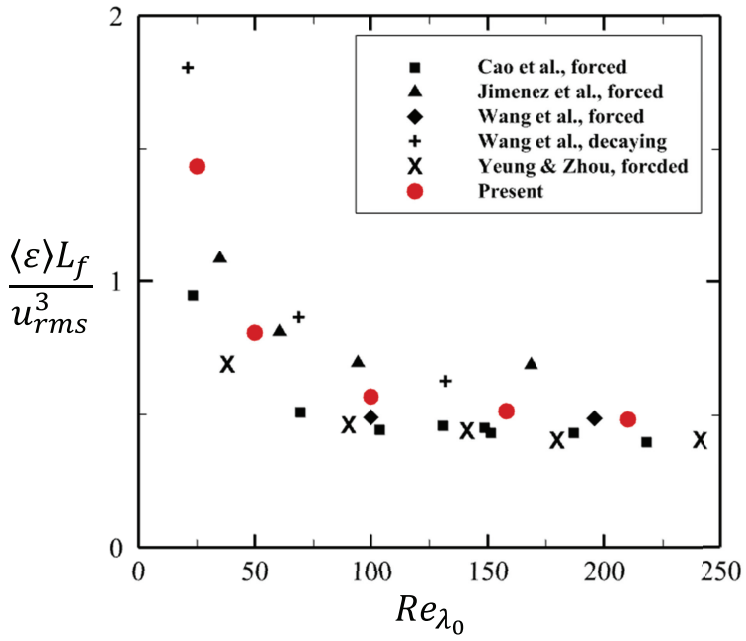

Figure 3.3: Dissipation quantity $\langle \epsilon \rangle \, L_f / u_{rms}^3$ vs. Reynolds number based on the initial Taylor microscale. Data from other various simulations are included.

3.4 Dynamics of Shearless Turbulent/Non-Turbulent Mixing

3.4.1 Qualitative Analysis in Turbulent/Non-Turbulent Mixing

We first examine the qualitative behavior of shearless turbulent/non-turbulent mixing. To visualize eddies, Fig. 4.4 (a, c, e, g) shows the Q-criterion (*Hunt et al.*, 1988) coloured by dilatation

$$Q = \frac{1}{2}\left[|\mathbf{\Omega}|^2 - |\mathbf{S}|^2\right], \tag{3.14}$$

where $\mathbf{S}$ is the strain-rate tensor and $\mathbf{\Omega}$ is the vorticity tensor. Iso-surfaces of scalar mass fraction are shown in Fig. 4.4 (b, d, f, h) coloured by vorticity magnitude. Turbulent eddies evolve into a wider range of scales, but eventually decay over time; Almost no eddies are visible based on the present Q-criterion by $t = 9\tau$. Over time, it is clear that some eddies have crossed beyond the $z = 0$ plane, indicating mixing. Roughly, it appears that eddies visible in the positive z region are smaller on average than those in the bulk region. The magnitude of dilatation remains approximately constant throughout the process, thus indicating that dilatational dissipation is slower than solenoidal dissipation (*Pan and Johnsen*, 2017). The size of the interfacial surface increases over time as the fluids mix; As expected, vorticity (magnitude) decreases significantly over the process. The spread of the 0.5 mass fraction contours indicates the turbulent and non-turbulent fluids mix over time as intermittent vortical structures in the turbulence stretch, the non-turbulent flow penetrates deep into the turbulent region (i.e., engulfment), and small-scale eddies diffuse at the interface (i.e., nibbling).

Fig. 4.5 shows two-dimensional contours of the mass fractions along the centre-plane at the same times for the $u_{rms,1} : u_{rms,2} = 1 : 0$ and $3 : 0$ cases, which have $Re_{\lambda_0} = 100$ and 215, respectively. For mixing with the larger turbulent intensity, a wider range of scales, including smaller scale motions, and extensive entrainment of

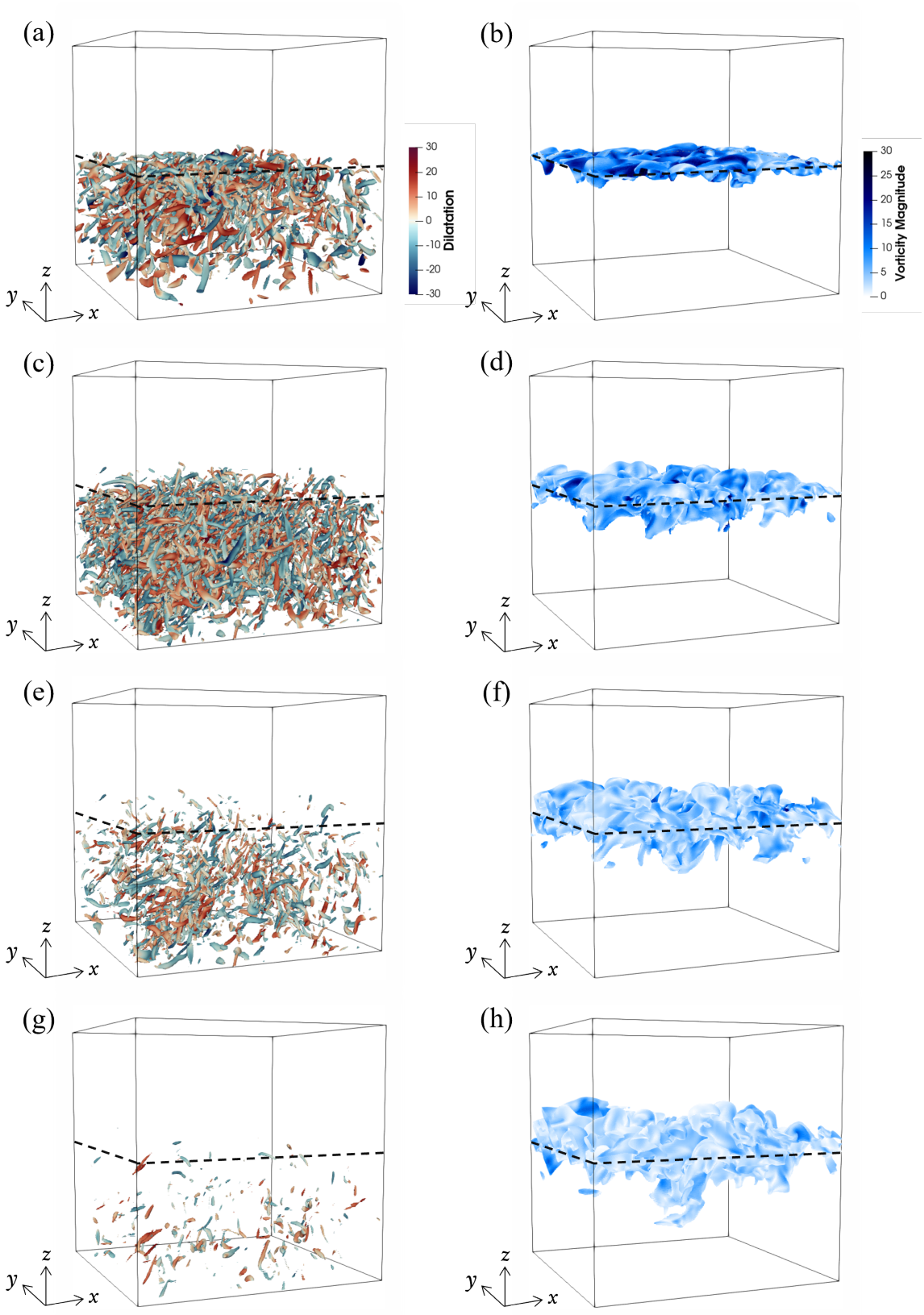

Figure 3.4: Q-criterion coloured by dilatation (left) and iso-surfaces of mass fraction $\langle Y_1 \rangle = 0.5$ coloured by vorticity magnitude (right) at $t = 1\tau$ (a, b), 3τ (c, d), 6τ (e, f) and 9τ (g, h) for case 1 ($u_{rms,1} : u_{rms,2} = 1 : 0, Re_{\lambda_0} = 100$, and $Ma_{t_0} = 0.1$).

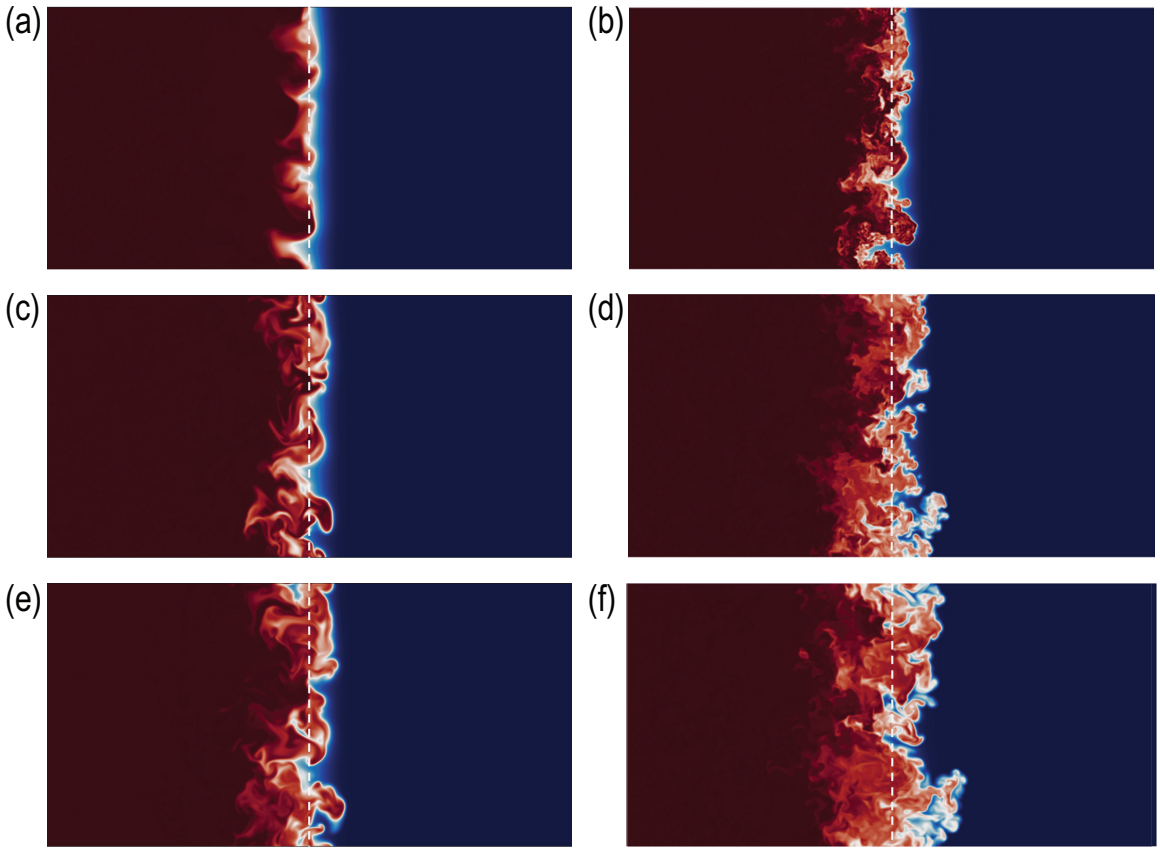

Figure 3.5: Two-dimensional contours of the mass fraction in the $x - z$ centreplane at $t = 0.412$ (a, b), 1.24 (c, d), and 2.06 (e, f) for $u_{rms,1} : u_{rms,2} = 1 : 0$ (left) and $u_{rms,1} : u_{rms,2} = 3 : 0$ (right). White dashed line: centreplane $(z = 0)$.

non-turbulent flow into the turbulent region, and vice-versa, are observed, which lead to more effective mixing and further spreading of the mixing region over time. The *ejection* of large-scale structures from the turbulent region can be discerned. These structures rapidly decay in the initially quiescent fluid.

3.4.2 Evolution of the Mixing Region

At sufficiently high Reynolds numbers, the mixing region width h is expected to follow a power law dependence in time, namely, $h \sim t^{\alpha}$ (*Youngs*, 1984; *Cook and Dimotakis*, 2001). Assuming incompressible flow and using dimensional analysis, *Barenblatt et al.* (1987) demonstrated that the interface position in the one-

dimensional propagation of a turbulent front into quiescent flow follows a power law $h \sim t^{2/3}$. However, in compressible flow, additional energy transport mechanisms are present, for instance, acoustic waves transporting TKE across the interface and dilatational TKE are observed in the non-turbulent region. Thus, identifying the edge of the interface requires additional considerations in the compressible case because the dilatational TKE is detected on the non-turbulent region. To be consistent with incompressible theory, we define the edge of the mixing region as the location where the TKE based on the solenoidal velocity (i.e., after Helmholtz decomposition) is less than a given threshold ϕ_I. We determine this ratio by examining the time dependence of the width of the mixing region, which is defined as $h = h_{\phi_I} - z_0$ where h_{ϕ_I} is the position of the mixing region edge ($k_{sol} = \phi_I$), and z_0 denotes $z = 0$. Letting $h \sim t^{\alpha}$, we find that the exponent α is sensitive to this threshold. When $\phi_I \approx 10^{-3}$, we recover the power law corresponding to the incompressible limit, with $\alpha = 2/3$; we thus use $\phi_I = 10^{-3}$ as the threshold for all cases. The time evolution of the mixing region width is shown in Fig. 4.6(a) for the different turbulent intensities and Mach numbers under consideration. The mixing region widths for the different turbulent intensities all increase at the same rate, with a temporal exponent of 2/3, consistent with *Barenblatt et al.* (1987).

3.4.3 Cumulative Energy Spectra

To better understand the evolution of the distribution of energy across scales within the mixing region, we examine the compensated spectra of the z-velocity fluctuation in the $x - y$ plane at different z-locations, defined

$$C_{w'}(k) = \frac{\int_0^k E_{w'}(k')dk'}{\int_0^\infty E_{w'}(k')dk'} \tag{3.15}$$

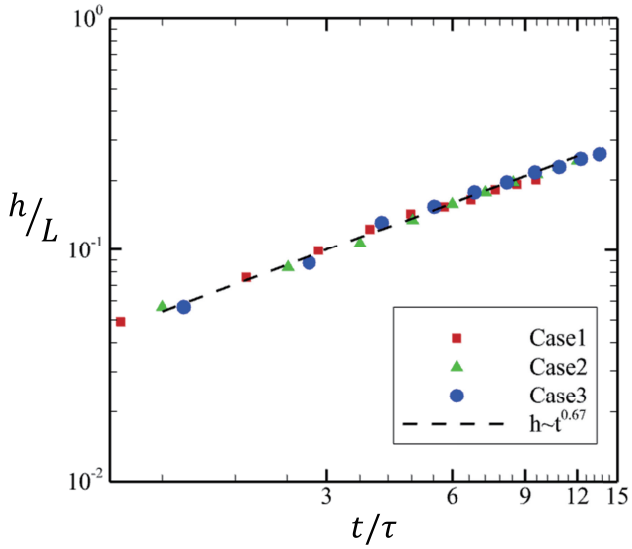

Figure 3.6: Temporal evolution of the mixing width relative to the centreplane ($z = 0$) for $u_{rms,_1} : u_{rms,_2} = 1 : 0$ (red), $u_{rms,_1} : u_{rms,_2} = 2 : 0$ (green), $u_{rms,_1} : u_{rms,_2} = 3 : 0$ (blue). The interface location is defined as the location in z where the solenoidal TKE $k_{sol} < \phi_I$. The black dashed line corresponds to a power law with the exponent of 0.67.

where k is the magnitude of the k_x and k_y. Fig. 4.9 compares the compensated spectra at the edge of the mixing region in the turbulent region ($\langle Y_1 \rangle = 0.95$) and at the center of the mixing region ($\langle Y_1 \rangle = 0.5$) for the baseline case to those corresponding to decaying homogeneous turbulence. The spectra indicate that the behavior at small wavenumbers is fully resolved for all cases as

$$\lim_{k \to 0} \frac{dC_{w'}(k)}{dk} \approx 0 \tag{3.16}$$

and energy transfer from smaller scales to larger scales is negligible (*Mueschke and Schilling*, 2009). At $\langle Y_1 \rangle = 0.95$, in Fig. 4.9(b), the evolution of the compensated spectra resembles that in the homogeneous case, although there is less energy at high wavenumbers, where energy is dissipated. By contrast, at $\langle Y_1 \rangle = 0.05$, the flow is non-turbulent as the distribution of scales is invariant over time. At the center of the mixing region where $\langle Y_1 \rangle = 0.5$ in Fig. 4.9(c), the discrepancy with

the homogeneous case is larger, and its slope is steeper compared to $\langle Y_1 \rangle = 0.95$, which indicates that small-scale eddies dissipate predominantly in the mixing region in shearless turbulent/non-turbulent mixing.

3.5 Turbulent Kinetic Energy Evolution

In the incompressible limit, upon volume averaging, the time-rate of the change of the TKE is equal to the negative of the dissipation rate in the Eq. 3.10. In the compressible case, the time-evolution of the TKE for shearless inhomogeneous flow consists of advection and dissipation:

$$\frac{\partial k(\mathbf{x},t)}{\partial t} = -\varepsilon_k(\mathbf{x},t) - \left|\frac{\partial q_j(\mathbf{x},t)}{\partial x_j}\right| \tag{3.17}$$

where k and ε_k are the local TKE and dissipation at $\mathbf{x}$, respectively, and q is the TKE flux (*Barenblatt et al.*, 1987). The pressure-dilatation term is negligible because it appears as dilatational dissipation and is rapidly self-canceled for shearless turbulence (*Lele*, 1994; *Sarkar*, 1992; *Freund et al.*, 2000). In the incompressible limit, upon volume averaging, the time-rate of the change of the TKE is equal to the negative of the dissipation rate in the Eq. (3.10). The TKE equation can be rewritten as follows:

$$\frac{\partial k(\mathbf{x},t)}{\partial t} = -\varepsilon_k(\mathbf{x},t) - \left|k(\mathbf{x},t)\frac{\partial u_j(\mathbf{x},t)}{\partial x_j}\right|. \tag{3.18}$$

Thus, the TKE changes due to dissipation and transport of kinetic energy into the non-turbulent region.

Dilatation plays an important role in turbulent/non-turbulent mixing. Fig. 4.7 shows the temporal evolution of the TKE for different intensities in our turbulent/non-turbulent mixing problems, as well as for the corresponding homogeneous cases. Fig. 4.7(a) indicates that after a short transient, the TKE decays exponentially in time.

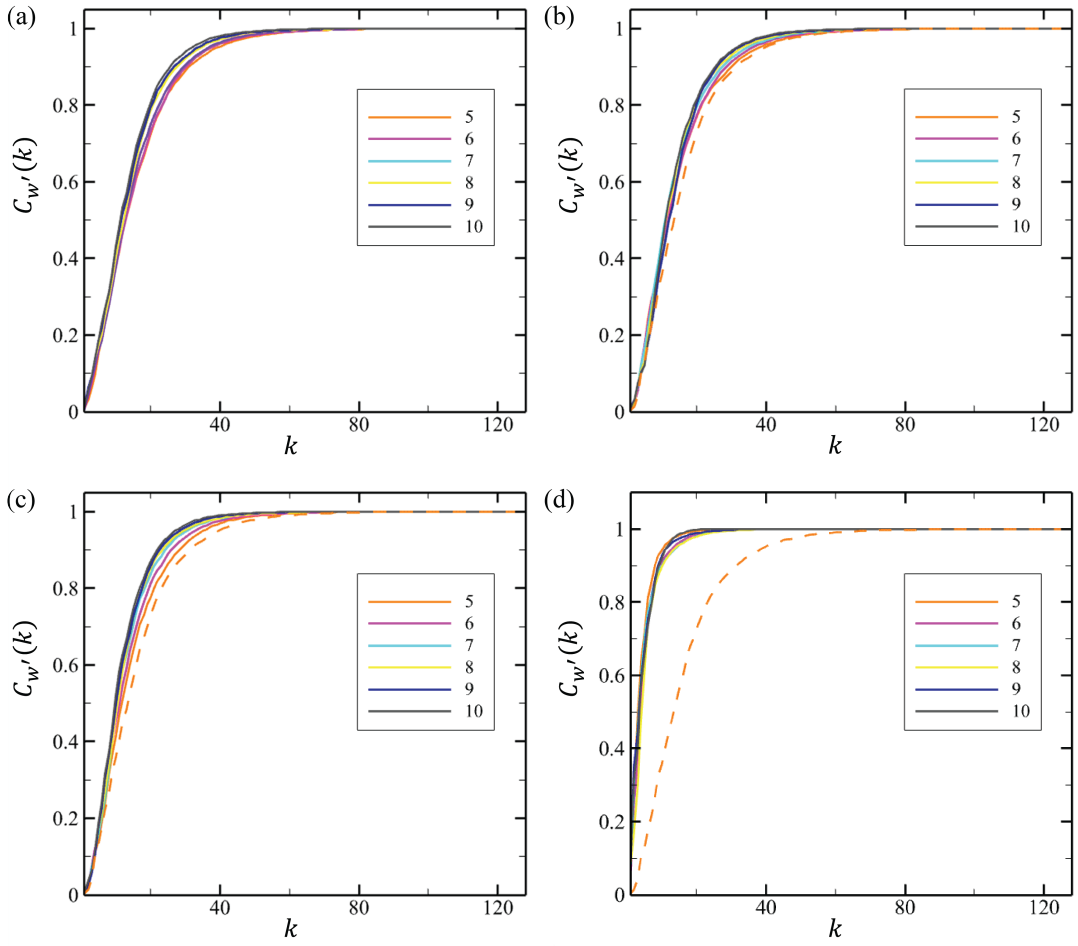

Figure 3.7: Cumulative energy spectra of turbulent kinetic energy corresponding to the z-velocity fluctuation at different times for (a) homogeneous isotropic turbulence in a periodic box and in the mixing region in turbulent/non-turbulent mixing at (b) $\langle Y_1 \rangle = 0.95$, (c) $\langle Y_1 \rangle = 0.5$, and (d) $\langle Y_1 \rangle = 0.05$. The dashed line represents homogeneous isotropic turbulence at $t = 5\tau$.

This result indicates that there is little change in the size distribution of eddies for freely decaying turbulence (*George and Wang*, 2009). The decay rate is higher for lower Reynolds numbers since the viscosity is higher. For all Reynolds numbers, the TKE decays more rapidly in turbulent/non-turbulent mixing. To elucidate the role of compressibility on turbulent/non-turbulent mixing, Eq. (4.18) can be integrated over volume based on the region $k_{sol} < \phi_I$ and time to obtain an expression for the TKE,

$$\frac{\langle k \rangle}{\langle k_0 \rangle} = exp\left[- \left(c_1 \left(t/\tau \right) + c_2 \int_0^t \left\langle \left| \frac{\partial u_z(t)}{\partial z} \right| \right\rangle dt \right) \right]. \tag{3.19}$$

We consider dilatation in the inhomogeneous direction z and assume that $\left\langle \left| k(\mathbf{x},t) \frac{\partial u_z(\mathbf{x},t)}{\partial z} \right| \right\rangle \approx \langle k(\mathbf{x},t) \rangle \times \left\langle \left| \frac{\partial u_z(t)}{\partial z} \right| \right\rangle$. The TKE depends on the rate of dilatation in Eq. 3.19 because of the inhomogeneity. Fig. 4.7(b) shows the evolution of TKE in scaled time with $c_1 \approx c_\varepsilon/3$ and $c_2/c_1 \approx \frac{1}{9}$ where c_ε is the dissipation quantity. We discuss below the more general dependence of c_1 and c_2 on the parameters governing the problem. The collapse of the TKE curves for turbulent/non-turbulent mixing onto those corresponding to the homogeneous case with the appropriate scaling in time indicates that dilatational transport (i.e., Eqs. (4.18) and (3.19)) accounts for the observed differences between turbulent/non-turbulent mixing and the homogeneous case as waves propagate from the turbulent into the non-turbulent region. For the cases with the lowest initial Reynolds number, some discrepancy is visible at late times, at which point the Reynolds number is relatively low, such that the behavior is Reynolds-number-dependent.

The effect of compressibility in this inhomogeneous flow is to transfer energy by dilatational TKE, which appears in the non-turbulent region. We focus on compressibility to complete the scaling for the turbulent kinetic energy in turbulent/non-

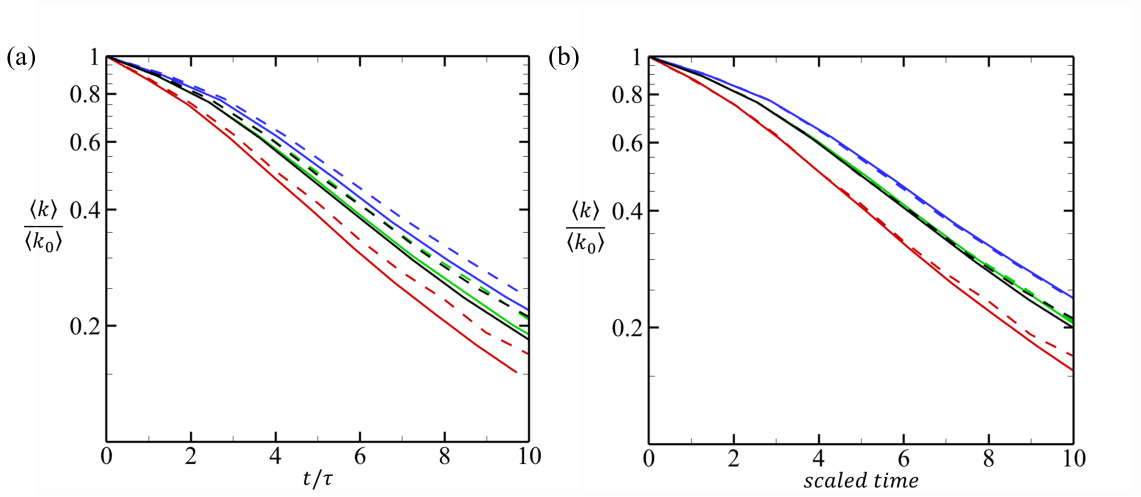

Figure 3.8: Time-evolution of the turbulent kinetic energy for case 1 ($u_{rms,1} : u_{rms,2} = 1 : 0$, $Re_{\lambda_0} = 100$, red), case 2 ($u_{rms,1} : u_{rms,2} = 2 : 0$, $Re_{\lambda_0} = 160$, green), case 3 ($u_{rms,1} : u_{rms,2} = 3 : 0$, $Re_{\lambda_0} = 215$, blue), and case 4 ($u_{rms,1} : u_{rms,2} = 1 : 0$, $Re_{\lambda_0} = 160$, black). Solid line: turbulent/non-turbulent mixing; dashed line: homogeneous case. Scaled time represents t/τ for homogeneous isotropic turbulence and $\frac{t}{\tau} + \frac{c_2}{c_1}\int_0^t \left\langle \left| \frac{\partial u_z(t)}{\partial z} \right| \right\rangle dt$ for turbulent/non-turbulent mixing where $\frac{c_2}{c_1} = \frac{1}{9}$ and $c_1 = \frac{c_\varepsilon}{3}$.

turbulent mixing. The volume- and time-averaged dilatation is

$$\theta = \frac{1}{t}\int_0^t \left\langle \left| \frac{\partial u_z}{\partial z} \right| \right\rangle / \left\langle \left| \frac{\partial u_z}{\partial z} \right| \right\rangle_0 dt. \tag{3.20}$$

Fig. 5.7 shows the temporal evolution of θ for turbulent/non-turbulent mixing with different magnitudes of u_{rms}. Since the volume-average dilatation does not change significantly with time, the scaling of Eq. (3.19) can be modified as

$$\frac{\langle k \rangle}{\langle k_0 \rangle} = \exp\left[-c_1 \frac{t}{\tau}\left(1 + \frac{c_2}{c_1}\Phi_0 \tau\right)\right] = \exp\left[-\frac{c_\varepsilon}{3}\frac{t}{\tau}\left(1 + \frac{1}{9}\Phi_0 \tau\right)\right] \tag{3.21}$$

where $\Phi_0 = \left\langle \left| \frac{\partial u_z}{\partial z} \right| \right\rangle_{t=0}$ is the initial volume-averaged dilatation.This equation indicates that dilatation enhances the decay of turbulent kinetic energy in inhomogeneous compressible turbulence, albeit via TKE leaving the mixing region. There are two factors scaling time in Eq. (5.16). The first corresponds to viscous dissipation and

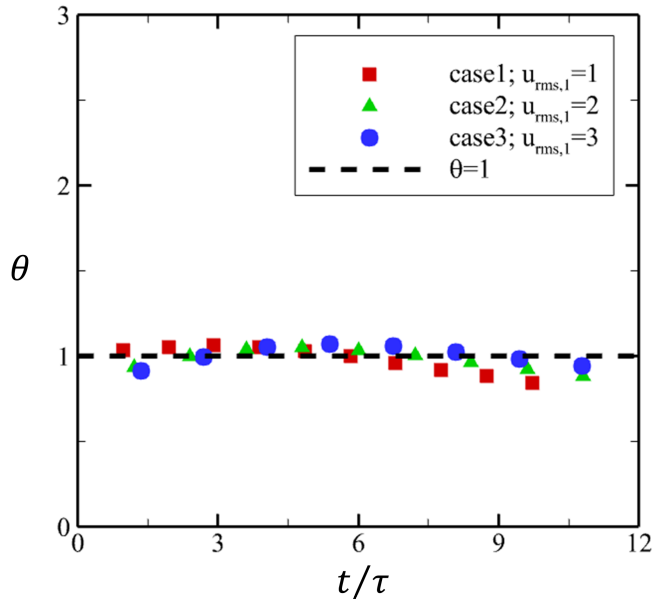

Figure 3.9: Time-evolution of dilatation for case 1 ($u_{rms,1} : u_{rms,2} = 1 : 0$, $Re_{\lambda_0} = 100$, red and square), case 2 ($u_{rms,1} : u_{rms,2} = 2 : 0$, $Re_{\lambda_0} = 160$, green and triangle), and case 3 ($u_{rms,1} : u_{rms,2} = 3 : 0$, $Re_{\lambda_0} = 215$, blue, circle).

the second accounts for energy losses by dilatation as energy is transported out of the mixing region.

We can therefore scale turbulent/non-turbulent mixing with different turbulent intensities, Reynolds numbers, and turbulent Mach numbers. Case 1 in Table 5.1 is set as the reference with $u_{ref} = 1$, $\lambda_{ref} = 0.05$, $Ma_{t,ref} = 0.1$, and $Re_{\lambda_{ref}} = 100$ representing fully developed compressible turbulence. The decay rates $c_\varepsilon/3$ and the length scales for fully developed turbulence are dependent on Reynolds number; thus a modification factor for the length scale, λ_0/λ_{ref}, is introduced,

$$\frac{\langle k \rangle}{\langle k_0 \rangle} = \exp\left[-\frac{c_{\varepsilon_{ref}}}{3}\frac{\lambda_0}{\lambda_{ref}}\frac{t}{\tau}\left(1+\frac{1}{9}\Phi_0\tau\right)\right]. \tag{3.22}$$

Fig. 4.2 shows the time-evolution of the TKE for both turbulent/non-turbulent mixing and the homogeneous case to verify this scaling. All the different cases collapse into a single curve and display the exponential decay predicted by Eq. (3.22), thus

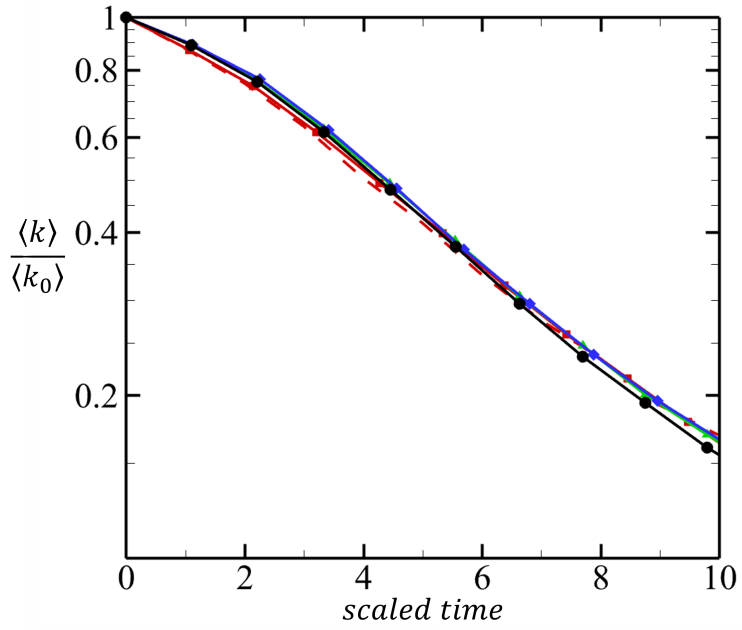

Figure 3.10: The decay of the volume-averaged turbulent kinetic energy as a function of time scaled by the Eq. (3.22) for case 1 ($u_{rms,1} : u_{rms,2} = 1 : 0$, $Re_{\lambda_0} = 100$, red), case 2 ($u_{rms,1} : u_{rms,2} = 2 : 0$, $Re_{\lambda_0} = 160$, green), case 3 ($u_{rms,1} : u_{rms,2} = 3 : 0$, $Re_{\lambda_0} = 215$, blue), and case 4 ($u_{rms,1} : u_{rms,2} = 1 : 0$, $Re_{\lambda_0} = 160$, black). Solid line: turbulent/non-turbulent mixing; dashed line: homogeneous case. Scaled time represents $\frac{\lambda_0}{\lambda_{ref}} \frac{t}{\tau} \left(1 + \frac{1}{9}\Phi_0 \tau\right)$ for turbulent/non-turbulent mixing.

verifying the proposed scaling.

3.6 Conclusions

In this work, we use theory and DNS to investigate compressible turbulent/non-turbulent mixing. We consider the juxtaposition of an initially isotropic turbulent field to a stationary fluid and examine mixing in decaying, shearless, heterogeneous turbulence. The decay rate of turbulence differs from that of homogeneous isotropic turbulence because of turbulent kinetic energy transport away from the mixing region due to dilatational effects. The mixing region grows as a power law in time consistent with past theory ($\sim t^{2/3}$). We demonstrate that the turbulent kinetic energy

depends on viscous dissipation and energy transport away from the mixing region due to dilatation. Thus, compared to the incompressible case, dilatation gives rise to an increased decay rate, We establish the dependence of the turbulent kinetic energy on time and the parameters governing the problem (Taylor scale, rms velocity, and initial dilatation); the DNS results agree well with the theory. This study on turbulent/non-turbulent mixing serves as a starting point for more general studies of shearless turbulent mixing, including possibly the role of density gradients and acceleration.

CHAPTER IV

Shearless Compressible Turbulent Mixing

4.1 Abstract

The classical turbulence theory of Kolmogorov for homogeneous isotropic turbulence does not directly apply to mixing between regions of different turbulent intensities, including if the turbulence is compressible. This study investigates the role of compressibility and inhomogeneity on turbulent mixing with gradients in turbulent intensity using direct numerical simulation (DNS). Two shearless turbulent fields with different root-mean-square velocities (u_{rms})are initially juxtaposed, such that mixing occurs between the higher- and lower-intensity regions over time. We are specifically interested in the role of inhomogeneity (via the ratio of turbulent intensities) and compressibility on the growth of the mixing region and on the turbulent kinetic energy in the mixing region. We find that the mixing region growth in a power-law in time. Dilatation in the inhomogeneous direction causes turbulent kinetic energy to decay at a rate lower than that in the higher-intensity region but higher than that in the lower-intensity region. These decay rates can be predicted from energy budget analysis by observing that the volume-averaged dilatation does not significantly change over time.

4.2 Introduction

Stratified turbulence plays an important role in geophysical fluid dynamics including oceanic and atmospheric flows, which exhibit variations of the mean density and turbulent intensity. For example, turbulence in a cloud increases the fraction of aerosol droplets and generates mixing at the cloud-air interface. During this process, the air entering the cloud accompanies heat and moisture fluxes through the interface (*Penc and Albrecht*, 1987) and develops different types of clouds. Entrainment, which is caused by turbulent intensity gradients, is critical in the development of atmospheric clouds (*Driedonks and Tennekes*, 1984; *Baker et al.*, 1984; *Blyth*, 1993; *Pruppacher et al.*, 1998; *Mellado*, 2017). This phenomenon has a significant impact on precipitation and can lead to different types of changes in weather, which physics can be used to develop global climate models (*Emanuel and Živković-Rothman*, 1999; *Cenedese and Adduce*, 2010; *Sahany et al.*, 2012; *Takahashi et al.*, 2021). Similarly, in the ocean, turbulence is induced by surface winds (*Skyllingstad et al.*, 2000). Gradients in velocity fluctuations and mean density as well as internal wave breaking or topography can give rise to vertically developing mixing regions. Mixing in the ocean creates vertical circulation that is critical for maintaining marine ecosystems and influencing weather patterns by transferring momentum and energy from the bottom of the ocean to the surface (*Garrett*, 1979; *Young et al.*, 1982; *Caldwell and Mourn*, 1995; *St. Laurent and Garrett*, 2002; *Rascle et al.*, 2006). Therefore, to improve our understanding of the global climate system, it is essential to isolate the effects of each factor in stratified flows, including turbulent intensity differences. However, predicting such flows is challenging due to the wide range of temporal and spatial scales, as well as their inherent nonlinearity. For instance, because atmospheric circulation is multiscale features, from the large motions of the cloud to interactions between small particles of the air, theory and experiments are limited (*Bryan et al.*, 1975; *Kousky et al.*, 1984; *Garreaud and Aceituno*, 2007; *Reichler*, 2009; *Knietzsch et al.*,

2015; *Hassan and Nayak*, 2020). High-fidelity simulations are challenging due to the exceedingly high Reynolds numbers and the lack of well-characterized initial conditions. Therefore, parameterization and averaged properties of large-scale motions are used to develop global circulation models representing oceanic and atmospheric circulation and predicting the global climate system (*Grotch and MacCracken*, 1991; *Randall*, 2000; *Satoh*, 2004; *Weart*, 2010). However, the predictive performance of such calculations relies on the quality of the models.

A strategy to understand specific elements of geophysical turbulence and possibly develop models is to use direct numerical simulations, in which all the dynamical scales are resolved (*Randall*, 2000; *Matsushima et al.*, 2021). A starting point for such studies is the canonical problem of homogeneous isotropic turbulence (HIT), whether forced or decaying (*Rogallo*, 1981; *Jiménez et al.*, 1993; *She et al.*, 1993; *Overholt and Pope*, 1996; *Moin and Mahesh*, 1998; *Gotoh and Fukayama*, 2001; *Yeung et al.*, 2006; *Kaneda and Ishihara*, 2006; *Donzis et al.*, 2008; *Ishihara et al.*, 2009). HIT can be generated both computationally and experimentally. Conventional turbulence theory describes this cascade process and proposes scalings of the statistics in the inertial subrange and dissipative scales based on the assumptions of an equilibrium state of HIT at sufficiently high Reynolds numbers (*Kolmogorov*, 1941a,b). For HIT, the decay of the turbulent kinetic energy (TKE) is described by the TKE equation:

$$\frac{d\langle k\rangle}{dt} = -\langle\varepsilon\rangle, \tag{4.1}$$

where $\langle\cdot\rangle$ represents the spatial volume-averaged quantity, $k = u_i u_i/2$ is the TKE per unit mass, and ε is the dissipation rate (*Batchelor*, 1953). Several studies demonstrated that the decay of TKE obeys the power law in time as follows (*Batchelor*, 1953; *Saffman*, 1967; *Gad-el Hak and Corrsin*, 1974; *Lee*, 1985; *Mohamed and LaRue*,

1990; *Burattini et al.*, 2006):

$$k \sim (t - t_0)^n, \tag{4.2}$$

where t is the time, and n is the decay rate. Kolmogorov derived the -10/7 decay law (*Kolmogorov*, 1941b) and an analytical approach to derive the power-law exponents using energy spectra, which is consistent with the Kolmogorov decay law (*Comte-Bellot and Corrsin*, 1966). Many studies on HIT have considered the self-similarity hypothesis of Kolmogorov, which describes universal statistics on a small scale (*Kolmogorov*, 1941a,b). However, the decay rate in the grid turbulence is highly dependent on the experimental setup, such as the type of grids or the initial conditions. Moreover, perforated plates generating shearless turbulence do not exhibit a power-law behavior away (*Veeravalli and Warhaft*, 1989), whereas grid turbulence follows self-similarity in space and time. *Dubrulle* (2000) showed that structures deviate from a power law with nonlinear exponents because of finite-size effects. Furthermore, under certain conditions, the TKE decays as an exponential function (*Kida and Orszag*, 1992; *Hurst and Vassilicos*, 2007; *George and Wang*, 2009; *Krogstad and Davidson*, 2012; *Pouransari et al.*, 2016). Further investigations are required to better understand the decay of TKE in HIT.

Most flows in nature and engineering depart from HIT conditions, such that Kolmogorov's assumptions (incompressible homogeneous isotropic flow at a sufficiently high Reynolds number) are not valid. Many turbulent flows are heterogeneous; for instance, the root-mean-square velocity, length scale, and/or density could vary more or less rapidly from one region of the flow to another. This inhomogeneity gives rise to a turbulent mixing region as turbulent eddies from one region interact with eddies from another region. For example, in free-shear flows such as wakes, jets, and mixing layers, the mean velocity gradient drives the turbulent mixing. The mixing region evolves through the entrainment of large-scale motions, i.e., vortices, and diffusion at the interface between the turbulent and the quiescent parts of the flow, across which

mass, momentum, and energy are transferred. Such inhomogeneous turbulent flows induce intermittent zone, which is characterized by a non-uniform spatial distribution in the statistics of variations and energy dissipation (*Bisset et al.*, 2002). The intermittent zone shows a non-Gaussian statistical distribution, deviating from the classic theory of turbulence and requiring anomalous scaling (*Toschi et al.*, 1999; *Laval et al.*, 2001; *Gualtieri et al.*, 2002; *Matsushima et al.*, 2021). Researchers such as *Jiménez et al.* (1993) and *She et al.* (1990) found that these intermittent statistics are relevant to coherent vortical structures in incompressible, isotropic turbulence. Furthermore, intermittent regions are found in free-shear flows, accompanied by entrainment near the interface of the mixing region and non-uniform distributions of velocity fluctuation. *Matsushima et al.* (2021) investigated the shearless turbulent mixing layer with differences in TKE and found that intermittent fluctuations caused by TKE diffusion are stronger in the mixing region at small scales, affecting the scaling exponents. Therefore, the classical theory should be further modified for predicting turbulent mixing with considering inhomogeneity.

Compressibility introduces additional challenges in the study of turbulence, as energy couples to the dynamics. Compressible flows are involved in turbulent fluctuations of thermodynamic properties, which can be decomposed into acoustic, vorticity, and entropy modes (*Kovasznay*, 1953). The effects of these fluctuations are dynamically combined between any two modes, which causes other modes (*Lele*, 1994). In addition to modes of fluctuations, non-zero dilatation gives rise to additional energy transfer mechanisms. *Lee et al.* (1991) discovered that, for decaying compressible turbulence, the dilatational component is more intermittent and has a skewed distribution of TKE. Moreover, the dilatational component is coupled to the solenoidal velocity field such that there is energy transfer between the two modes. However, compressibility effects combine nonlinearly (*Moyal*, 1952; *Chu and Kovásznay*, 1958), such that each effect must be considered separately to determine its role in turbulence.

On the other hand, classical theory can be extended for compressible HIT because an inertial range with universal statistics exists for compressible turbulence at high Reynolds numbers (*Aluie*, 2011). However, analysis of the dilatational component requires additional approaches because it does not adhere to Kolmogorov similarity (*Jagannathan and Donzis*, 2016; *John et al.*, 2019; *Donzis and John*, 2020). *Kida and Orszag* (1990) found that the solenoidal velocity field is not influenced by compressibility effects such that the energy spectrum is that expected for incompressible flow, whereas the energy spectrum corresponding to the dilatational component depends on the turbulent Mach number. Furthermore, *Kida and Orszag* (1992) and *Jagannathan and Donzis* (2016) investigated the statistics of decaying compressible turbulence for different Reynolds and turbulent Mach numbers and discovered that the dilatation scaling depends on the turbulent Mach number. *Donzis and John* (2020) suggested that the ratio of dilatational and solenoidal root-mean-square velocities enables universal scaling for compressible flow. However, phenomenology in compressible and heterogeneous flows is poorly understood, and universal scaling to describe intermittent features in turbulence is still being investigated. Therefore, compressible turbulent mixing, which has been overlooked in conventional turbulence studies, must be considered.

The objective of this study is to understand the role of compressibility on shearless turbulent mixing and of gradients in turbulent intensity on the TKE. We conduct DNS of two juxtaposed regions of shearless turbulence with different intensities and examine the dependence of the mixing region growth and TKE on the intensity ratio. The remainder of this paper is organized as follows. The problem under consideration is described in Section 4.3. The dynamics of compressible turbulent mixing, including the mixing region growth and inhomogeneity in turbulent mixing, are examined in Section 4.4. Section 4.5 revises the scaling for the decay of TKE and dilatation. Section 4.6 summarizes the findings.

4.3 Problem Setup and Governing Equations

4.3.1 Problem Setup

We investigate compressible turbulent mixing in the presence of gradients in turbulent intensity. Fig. 5.1 shows a schematic of the problem under consideration. Two shearless HIT fields of the same fluid but with different intensities are juxtaposed, with the inhomogeneous direction being z. The domain size is $L \times L \times 8L$ with the inhomogeneous direction being z. The domain size is $L \times L \times 8L$, which is sufficiently large to prevent the boundaries from influencing the mixing region. The interface between the lower- and higher-energy regions is initially located at $z = 0$, and each half of the domain is made up of 4 L^3 boxes. Table 5.1 lists the initial conditions, where three cases are considered based on the initial root-mean-squared velocity, Taylor-scale Reynolds number, and turbulent Mach number. The initial Reynolds and turbulent Mach numbers are defined as follows:

$$Re_\lambda = \frac{u_{rms}\lambda}{\nu}, \quad Ma_t = \frac{u_{rms}}{\langle c \rangle}, \tag{4.3}$$

$$u_{rms} = \sqrt{\frac{\langle u_i u_i \rangle}{3}}, \quad \lambda = \frac{\langle u_i^2 \rangle}{\left\langle \left(\frac{\partial u_i}{\partial x_i} \right)^2 \right\rangle}, \tag{4.4}$$

where $\langle \cdot \rangle$ represents volume-averaged quantities, u_{rms} is the root-mean-square velocity, c the sound speed, ν the kinematic viscosity and λ the Taylor microscale. The equations are non-dimensionalized using the reference properties, which are $u_{rms,_1} = 1$ in the lower-energy region, $\rho_{ref} = \rho_1$, and $l_{ref} = L/(2\pi)$. We apply a zero-gradient boundary condition in the inhomogeneous direction and a periodic boundary condition in others. A uniform grid is used with 256 points per L, which is sufficient to resolve all the dynamical scales of motion (*Movahed and Johnsen*, 2015; *Pan and Johnsen*, 2017).

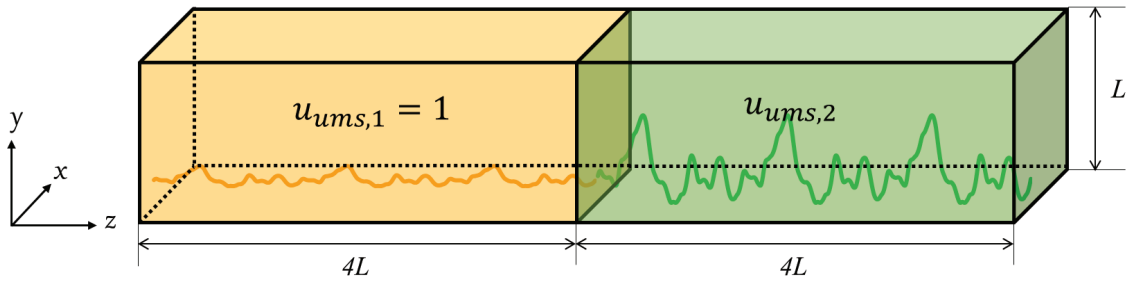

Figure 4.1: Schematic of the computational setup for compressible turbulent mixing with gradients in turbulent intensity. The two fluids have the same properties but different root-mean-square velocity magnitudes. The initial turbulent field in a cube of L^3, which is initially homogeneous isotropic, is juxtaposed in an inhomogeneous direction z.

	$u_{rms,1}$	$u_{rms,2}$	$Re_{\lambda_{0,1}}$	$Re_{\lambda_{0,2}}$	$Ma_{t_{0,1}}$	$Ma_{t_{0,1}2}$
case1	1	1	100	100	0.1	0.1
case2	1	2	100	156	0.1	0.2
case3	1	3	100	211	0.1	0.3

Table 4.1: Initial conditions of root-mean-square velocity magnitudes u_{rms}, the corresponding Reynolds numbers Re_{λ_0}, and turbulent Mach numbers Ma_{t_0} of fluid 1 and 2, respectively.

A passive scalar is used to quantify the mixing region growth by initializing the interfaces as follows:

$$Y_1(z) = \frac{1}{2}\left[1 - erf\left(\frac{z - z_0}{H}\right)\right], \tag{4.5}$$

where $z_0 = 0$ and $H = 8L/128$ (*Movahed and Johnsen*, 2015). The value of H enables resolving the steep interface on the $N = 128$ grid in the z direction and avoiding using additional numerical methods to describe discontinuity and minimize artificial dissipation (*Johnsen et al.*, 2010). Therefore, the mixing region departs from a finite initial thickness.

To examine energy fluxes through interfaces, the control volume is defined with the half domain $4L \times L \times L$. Fig. 4.2 shows a schematic of the mixing region and the left/right regions of the mixing region in the entire domain. The regions are divided based on the mass fraction of the passive scalar, where the left and right interfaces

Figure 4.2: Schematic of the control volume. Quantities are volume-averaged on the mixing region (red), the left (yellow) and right (orange) sides of the mixing regions. The total volume considered is $L \times L \times 4L$.

are located at $\langle Y_i \rangle = 0.05$ and $\langle Y_i \rangle = 0.95$. The regions are denoted as region 1, mixing region, and region 2.

4.3.2 Governing Equations

The three-dimensional compressible Navier-Stokes equations are solved along with the ideal gas law.

$$\frac{\partial \rho}{\partial t} + \frac{\partial}{\partial x_j}(\rho u_j) = 0 \tag{4.6}$$

$$\frac{\partial (\rho u_i)}{\partial t} + \frac{\partial}{\partial x_j}(\rho u_i u_j + p\delta_{ij}) = \frac{1}{Re}\frac{\partial \tau_{ij}}{\partial x_j} \tag{4.7}$$

$$\frac{\partial E}{\partial t} + \frac{\partial}{\partial x_j}[u_j(E+p)] = \frac{1}{Re}\left[\frac{\partial (u_j \tau_{ij})}{\partial x_j} + \frac{\partial}{\partial x_j}\left(\kappa_T \frac{\partial T}{\partial x_j}\right)\right] \tag{4.8}$$

$$p = \rho R T \tag{4.9}$$

Here, $E = \rho\left(e + u_i u_i/2\right)$ is the total energy per volume, $e = p/\left(\rho(\gamma - 1)\right)$ the internal energy per mass, ρ the density, u_j the velocity, p the pressure, T the temperature, γ the specific heats ratio, R the gas constant, κ_T the thermal conductivity, and Re the scaled Reynolds number; $Re_{\lambda_0} = Re\left[\frac{\rho_1 u_{rms,1} \lambda_{0_1}}{\mu_1}\right]$. The specific heat ratio is set to $\gamma = 1.4$, and a Newtonian gas with viscous stress tensor τ_{ij} is considered:

$$\tau_{ij} = \mu\left[\left(\frac{\partial u_i}{\partial x_j} + \frac{\partial u_j}{\partial x_i}\right) - \frac{2}{3}\frac{\partial u_k}{\partial x_k}\delta_{ij}\right]. \tag{4.10}$$

The transport equation for the passive scalar is also solved for analysis purposes:

$$\frac{\partial(\rho Y_i)}{\partial t} + \frac{\partial(\rho u_j Y_i)}{\partial x_j} = \frac{1}{ReSc}\frac{\partial}{\partial x_j}\left(\rho \frac{\partial Y_i}{\partial x_j}\right), \tag{4.11}$$

where $Sc = \mu_1/\rho_1 D$ is the Schmidt number, D the mass diffusivity, and Y_i the mass fraction of fluid $i = 1$ *or* 2. In this study, the kinematic viscosity and diffusivity are equal; that is $Sc = 1$. These equations are non-dimensionalized based on the parameters of a fluid with less turbulent energy: $u_{ref} = 1$, $\rho_{ref} = \rho_1$, and $l_{ref} = L/(2\pi)$. An explicit fourth-order Runge-Kutta scheme and high-order finite differences (i.e., sixth-order explicit central differences) are used in time and space to solve the above equations. The problem under consideration does not involve shocklets, because the turbulent Mach numbers are relatively low ($Ma_t < 0.4$). Thus, shock capturing or artificial dissipation is not required. The split form is applied in the convective fluxes based on the form used by *Blaisdell et al.* (1996):

$$\frac{\partial}{\partial x_j}(\rho u_j \phi) = \frac{1}{2}\left[\frac{\partial}{\partial x_j}(\rho u_j \phi) + u_j \frac{\partial}{\partial x_j}(\rho \phi) + \rho\phi \frac{\partial u_j}{\partial x_j}\right]. \tag{4.12}$$

Here, $\phi = (1,\ u_i,\ (E+p)/\rho,\ Y_i)$, and the flux of *Ducros et al.* (2000) is implemented. The non-conservative form is used for discretizing the diffusive terms:

$$\frac{\partial}{\partial x_j}\left(\mu \frac{\partial u_j}{\partial x_j}\right) = \mu \frac{\partial^2 u_j}{\partial {x_j}^2} + \frac{\partial \mu}{\partial x_j}\frac{\partial u_j}{\partial x_j}. \tag{4.13}$$

These forms prevent aliasing errors by minimizing the unphysical pile-up of energy at high wavenumbers, resulting in nonlinear stability and a better simulation of compressible turbulence (*Pirozzoli*, 2011).

4.3.3 Initialization and the Decay of Shearless Homogeneous Isotropic Turbulence

We use shearless HIT with no mean velocity to avoid coupled reactions accompanied by shear or energy production and to isolate the effect of intensity gradients in turbulent mixing. The initialization process suggested in Chater II is used for generating shearless HIT with an equilibrium state of turbulence with desired properties from the start. This rescaled shearless HIT is not interrupted by shear force or TKE production and decays only by dissipation. For shearless turbulence, the dissipative scale diffuses fastest, while eddies of the energy-containing length scale break and transfer energy to the smaller eddies; therefore, the Taylor microscale is invariant in time during the decay process (*Davidson*, 2015). Hence, the temporal evolution of TKE is derived as an exponential function of time ($\tau = \lambda_0/u_{rms_0}$ is an initial eddy turnover time) for shearless turbulence at sufficiently high Reynolds numbers:

$$\frac{\langle k \rangle}{\langle k_0 \rangle} = exp\left[-\frac{c_\varepsilon}{3}\left(t/\tau\right)\right]. \tag{4.14}$$

where $c_\varepsilon = \langle \varepsilon \rangle \, l_f/u^3_{rms_0}$ and l_f denotes the volume-averaged integral scale as determined in Chapter III.

4.4 Dynamics of Compressible Turbulent Mixing

4.4.1 Qualitative Results

We first examine the qualitative behavior of compressible turbulent mixing with turbulent intensity gradients. Fig. 4.3 shows two-dimensional contours of mass fractions of the passive scalar for mixing with differences in u_{rms} magnitudes at different times to observe the growth of the mixing region. In Fig. 4.3(a,d,g), for turbulent mixing with no intensity gradients, i.e., homogeneous isotropic turbulence, the

growth is symmetric about the mid-plane ($z = 0$). However, as the intensity differences increase to $u_{rms,1} : u_{rms,2} = 1 : 2$ and $1 : 3$, the mixing regions evolve more extensively, and more small-scale eddies develop. At later times in Fig. 4.3(g,h,i), larger-scale structures are observed as small-scale eddies are dissipated. Additionally, with increasing u_{rms}, there is more asymmetry in the mixing as the higher-energy flow penetrates deeper into the lower-energy region, which enhances the growth rate of the mixing region. Furthermore, the penetration of the higher-energy flow pushes the interface of $\langle Y_i \rangle = 0.5$ towards the lower-energy region and causes more fluctuations in the lower-energy region, which also lead to enhanced mixing. Therefore, such qualitative results provide insight into the growth of the mixing region with the behavior of eddies depending on turbulent intensity.

To identify compressibility in turbulence, contours of vorticity magnitude and dilatation for Case 3 ($u_{rms,1} : u_{rms,2} = 1 : 3$) are presented in Fig. 4.4. The dilatation component in compressible turbulence is comprised of different structures from vortical (rotational) structures. The contour of vorticity shows the rotational structures, where the more intense eddies are visible in the higher-energy region. In contrast, sheet-like structures of the dilatation in the compressible flow are observed, which can induce additional mixing mechanisms. Therefore, as compressibility in turbulence is qualitatively confirmed, further quantitative analysis for dilatation is explored in the following sections.

4.4.2 Mixing Region Growth

The mixing region develops as turbulent eddies from one region exchange momentum and energy with eddies from the other side. The mass fraction of the passive scalar determines the mixing region width, which is defined as the distance between $0.05 \leq \langle Y_i \rangle \leq 0.95$ (*Movahed and Johnsen*, 2015). This method is effective for analyzing turbulence behavior because the fluctuations of the turbulent flow make it

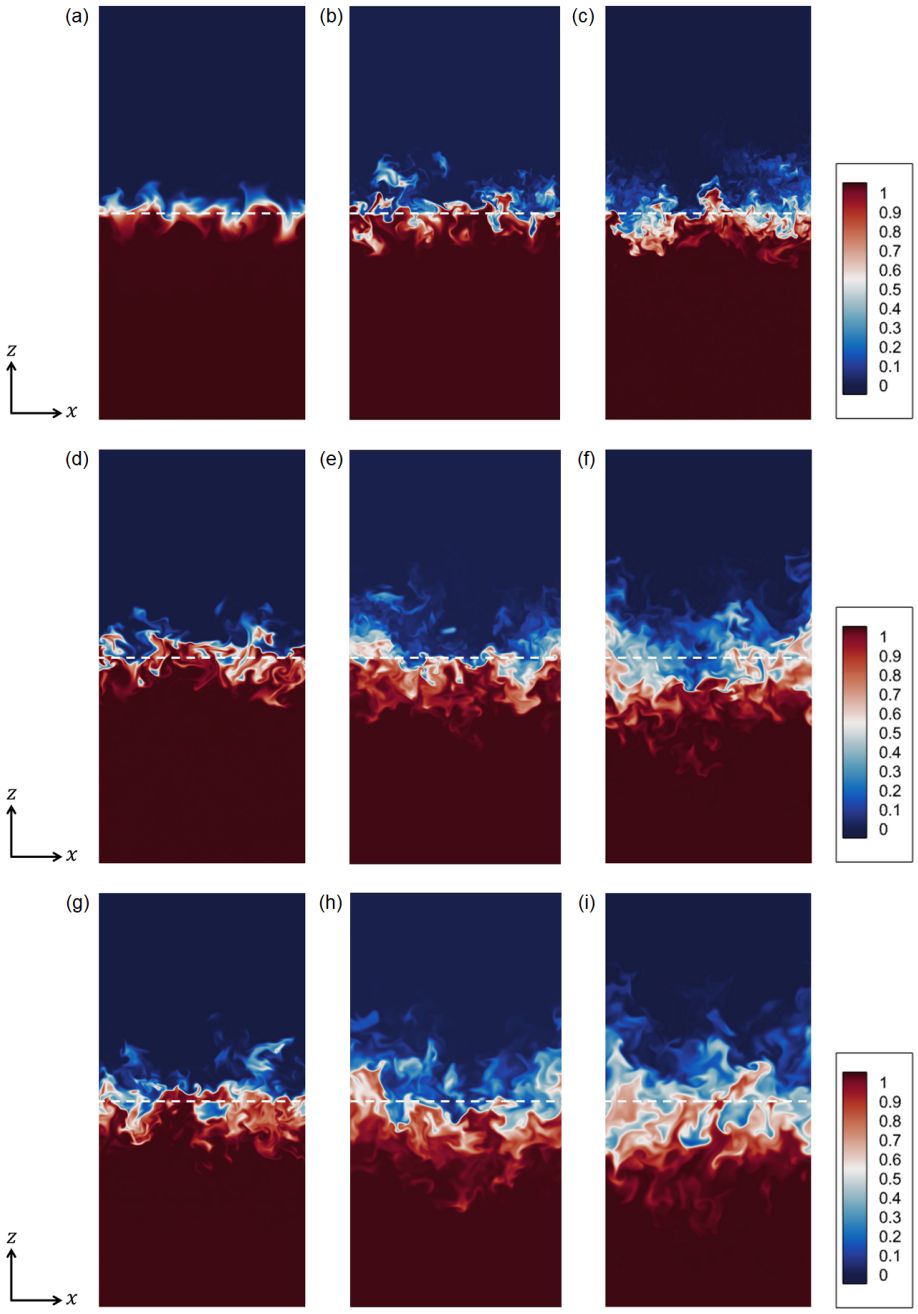

Figure 4.3: Two-dimensional contours of the mass fraction of passive scalar at $t = 0.142$ (a,b,c), $t = 1.236$ (d,e,f), and $t = 2.06$ (g,h,i) for Case 1 $(u_{rms,1} : u_{rms,2} = 1 : 1)$ (a,d,g), Case 2 $(u_{rms,1} : u_{rms,2} = 1 : 2)$ (b,e,h), and Case 3 $(u_{rms,1} : u_{rms,2} = 1 : 3)$ (c,f,i). The mixing develops in an inhomogeneous direction z, which is the vertical direction, and the white line at the center corresponds to the mid-plane $(z = 0)$. The blue and red colors represent the higher-intensity region $\langle Y_i \rangle = 0$ and the lower-intensity region $\langle Y_i \rangle = 1$, respectively.

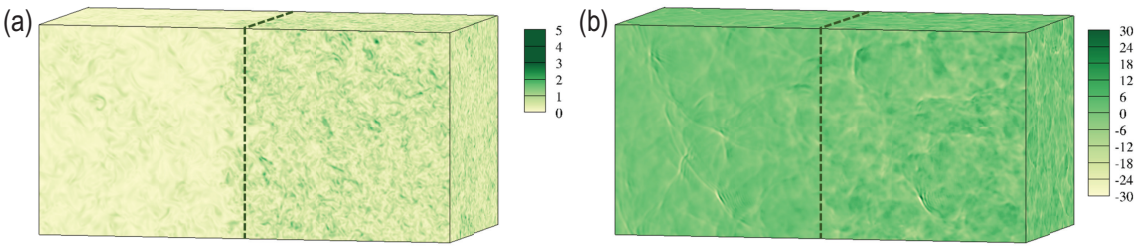

Figure 4.4: Contours of (a) vorticity magnitude and (b) dilatation at $t = 2\tau$ for Case 3 ($u_{rms,1} : u_{rms,2} = 1 : 3$). The area of $L \times 2L$ shows the mixing region with the black dotted line at $z = 0$. The smaller scales are observed in the higher-intensity region for vortical and sheet-like compressible structures.

difficult to have a consistent criterion for distinguishing features from the different regions. Fig. 4.2 illustrates a schematic diagram of the mixing region and the left/right regions of the mixing region in the entire domain, which are divided based on the mass fraction of the passive scalar. It is advantageous to analyze the mixing physics such as energy transfer through the interfaces. For shearless turbulence, the mixing region obeys self-similarity and develops as a power law. Fig. 4.5 shows the temporal evolution of the mixing region on the left and right sides of the mixing region and the total mixing region for mixing with different gradients, which are denoted as $h_L = z_0 - z_{Y_1=0.05}$, $h_R = z_{Y_1=0.95} - z_0$, and $h_t = h_L + h_R$, respectively. The mixing region widths propagate as a power law with the same exponent 0.43 in time scaled by Taylor microscale and eddy turnover time. The total mixing region width, which is $h_t = h_L + h_R$, is scaled as

$$h_t/\lambda_0 = c_h \times \left(t/\tau\right)^{0.43} \tag{4.15}$$

where $c_h \approx 5.0$. The mixing region width is scaled by the initial Taylor microscale, which collapses all cases with different intensity gradients; therefore, large-eddy motions dominate the growth of the mixing region.

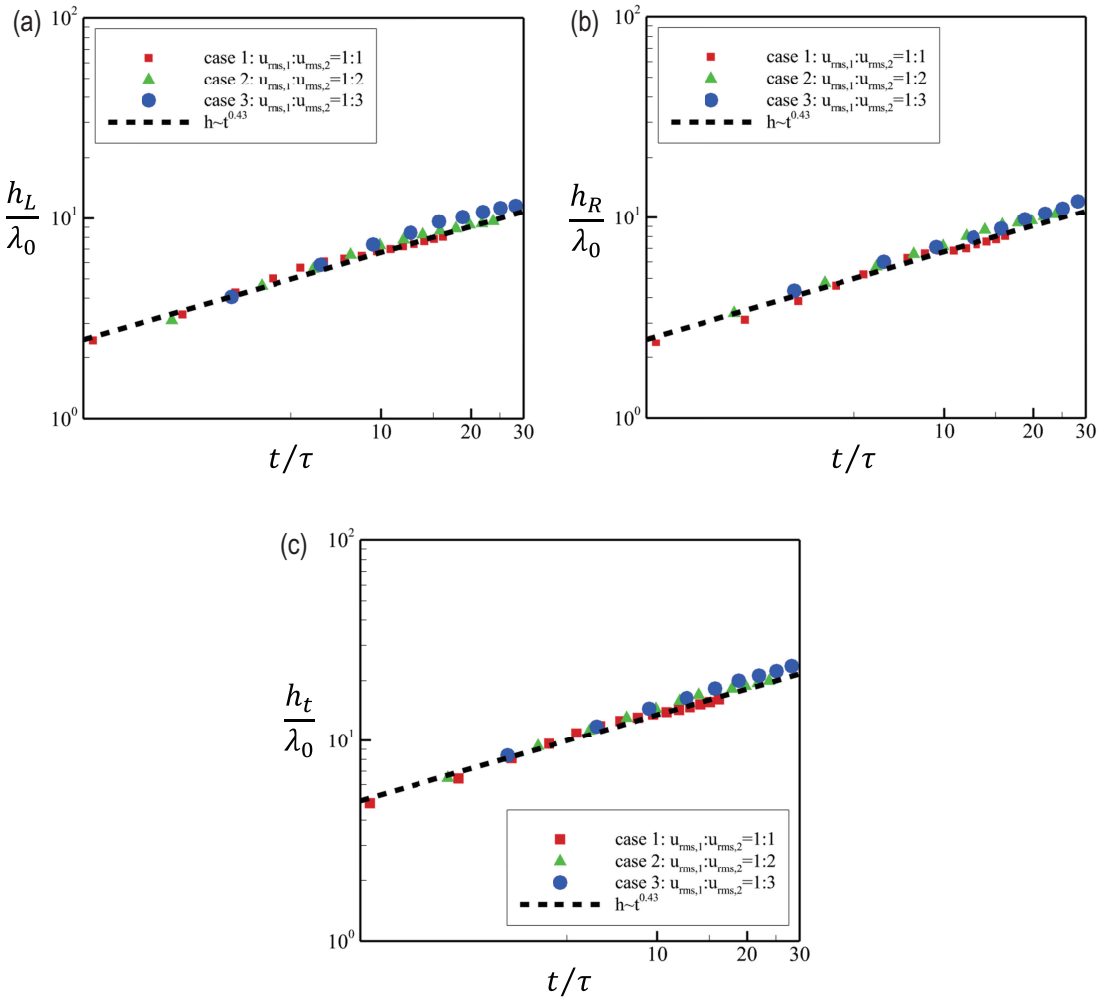

Figure 4.5: Evolution of the mixing region with respect to time normalized by eddy turnover time. The widths between the mid-plane $z = 0$ and the (a) left or (b) right interfaces grow as a power law of exponent 0.43. (c) The total mixing region width has the same growth rate, which is all normalized by the initial Taylor microscales for Case 1 (red, square), Case 2 (green, delta), and Case 3 (blue, circle).

4.4.3 Inhomogeneity in Turbulent Mixing

Inhomogeneous flow such as the turbulent/turbulent interface exhibits intermittent large-scale eddies penetrating into the other region while small-scale nibbling occurs. The entrainment of large-scale motions is a manifestation of anisotropy in the flow, as the energy dissipation rate is spatially non-uniform. In Fig. 4.6, the kurtosis K in the inhomogeneous direction z within the mixing width is shown for Case 1 ($u_{rms,_1} : u_{rms,_2} = 1 : 1$) and 3 ($u_{rms,_1} : u_{rms,_2} = 1 : 3$) at different times. For Case 1, kurtosis is relatively constant, showing minor fluctuations close to what is expected for Gaussian statistics ($K = 3.26$). In contrast, Case 3 exhibits the increase of kurtosis on the lower intensity side early on (until $t \approx 3\tau$) in the turbulent mixing. To determine the cause of this intermittent behavior, Fig. 4.7(a-b) shows probability density functions (PDFs) of dilatation for Case 1 and 3, which are obtained at different locations. For the homogeneous case, the PDFs follow a Gaussian distribution at all locations. However, for the inhomogeneous cases, we observe long tails of the PDF deviating from a Gaussian distribution. Additionally, at the center of the mixing region where $\langle Y_1 \rangle = 0.5$, the PDF is tilted in the negative direction, which indicates that compressibility, i.e., dilatation, transfers energy along the gradient. Fig. 4.7(c-d) shows PDFs of vorticity and dilatation at $t = 2\tau$ and $\langle Y_1 \rangle = 0.5$, at which point two flows are evenly mixed. The PDFs of directional vorticities represent the solenoidal part of the velocity fields. The vorticity PDFs in Fig. 4.7(c) do not follow Gaussian distributions but present bell-shaped, symmetric, and isotropic distributions. Nonetheless, the PDFs of dilatation are asymmetric and tilted in the negative direction, as presented in Fig. 4.7(d). Therefore, these results demonstrate that inhomogeneity in intensity gradients causes intermittent behavior within the lower-energy region of turbulent mixing.

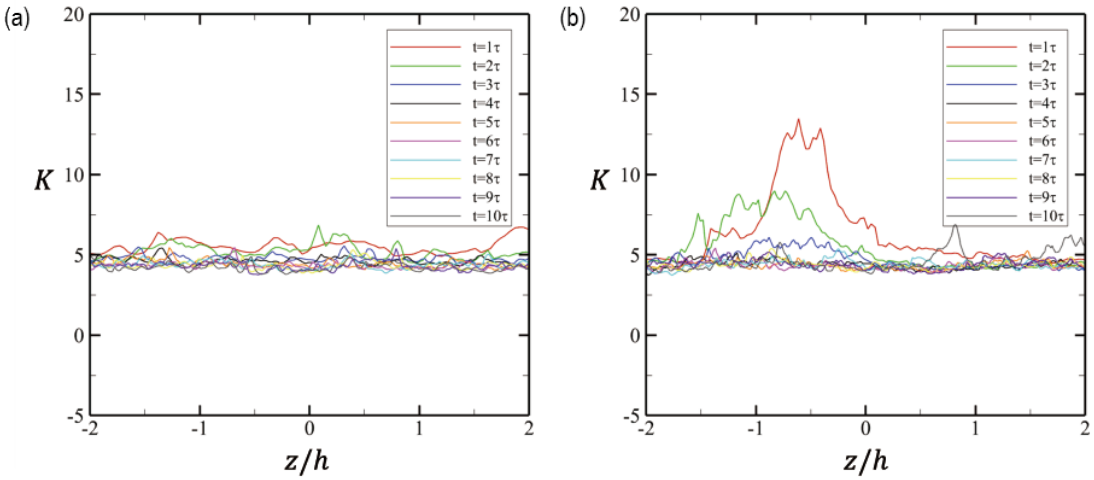

Figure 4.6: Kurtosis in the inhomogeneous direction z at different times for (a) Case 1 ($u_{rms,_1} : u_{rms,_2} = 1 : 1$) and ($b$) Case 3 ($u_{rms,_1} : u_{rms,_2} = 1 : 3$).

4.5 Decay of Turbulent Kinetic Energy in Compressible Turbulent Mixing

4.5.1 Scaling for the Decay of Turbulent Kinetic Energy in Shearless Turbulence

We consider the control volume with region 1, mixing region, and region 2 to examine the energy transfer through the interface, as illustrated in Fig. 4.2. Subsequently, the total TKE in turbulent mixing can be estimated by the sum of the TKE with coefficients in each region as follows:

$$\frac{\langle k_t \rangle}{\langle k_{t,0} \rangle} = \sum_{n=1,m,2} a_n \frac{\langle k_n \rangle}{\langle k_{n,0} \rangle} = a_1 \frac{\langle k_1 \rangle}{\langle k_{1,0} \rangle} + a_m \frac{\langle k_m \rangle}{\langle k_{m,0} \rangle} + a_2 \frac{\langle k_2 \rangle}{\langle k_{2,0} \rangle} \tag{4.16}$$

where the indices 1, m, and 2 represent the region left of the mixing region, the mixing region, and the region right of the mixing region. The coefficients a_n are determined based on the volume of each region.

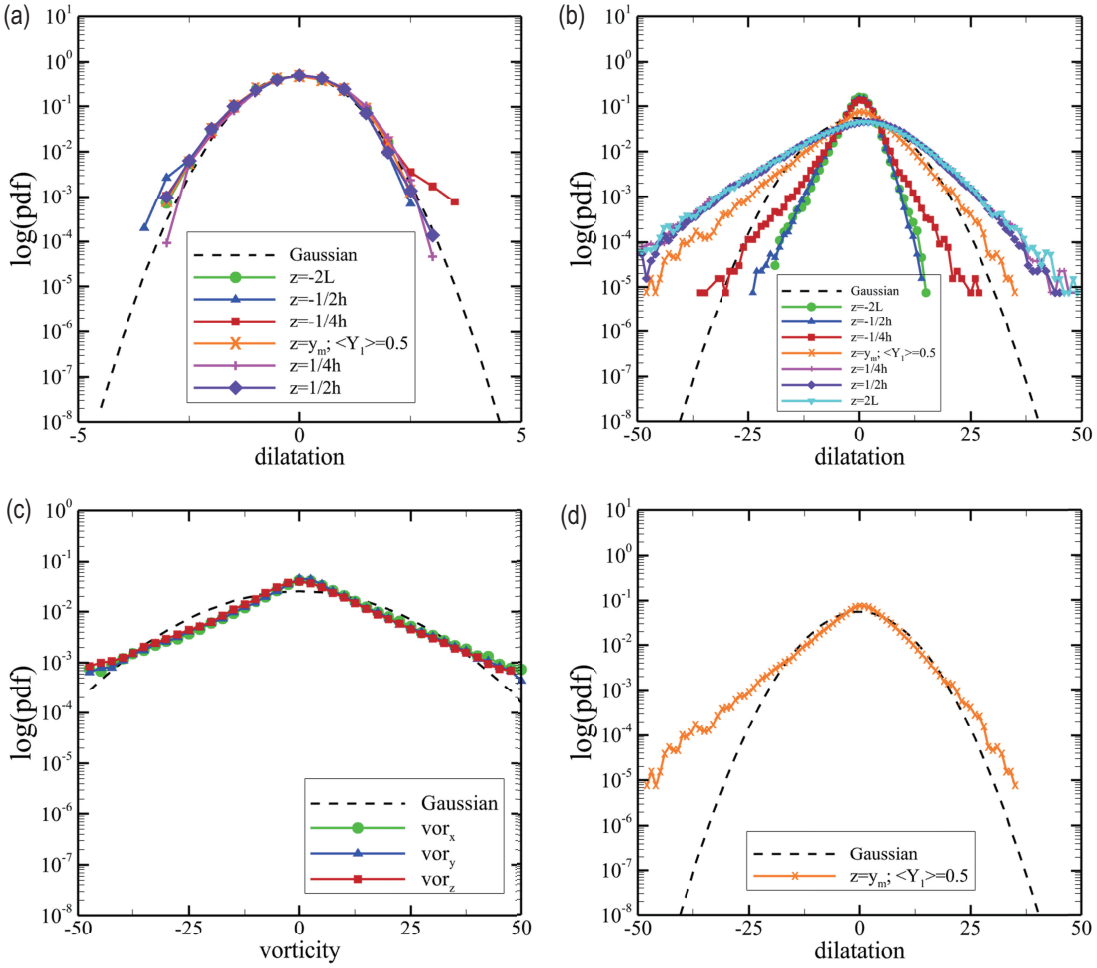

Figure 4.7: Probability density functions (PDFs) of dilatation at different locations in z for (a) Case 1 ($u_{rms,1} : u_{rms,2} = 1 : 1$) and (b) Case 3 ($u_{rms,1} : u_{rms,2} = 1 : 3$) at $t = 2\tau$. At the center of the mixing region, where the mass fraction $\langle Y_i \rangle = 0.5$, (c) the PDFs of vorticity in x, y, and z directions and (d) the PDF of dilatation are compared for Case 3 at $t = 2\tau$.

$$a_1 = \frac{(2L - h_L)}{4L}, \quad a_2 = \frac{(2L - h_R)}{4L}, \quad a_m = \frac{(h_L + h_R)}{4L} \tag{4.17}$$

where the summation of coefficients is unity; $a_1 + a_2 + a_m = 1$, and Eq. (4.15) can be used for h_L and h_R.

In Chapter III, we investigate the decay of TKE in shearless turbulent and non-turbulent mixing. The TKE decays by viscous dissipation in the same manner as HIT, but additional energy loss occurs because of compressibility effects and inhomogeneity. Thus, both the triple moment transport and TKE dissipation budgets play a role in the temporal decay of TKE. The triple moment transport, that is the energy flux, can be decomposed into advection and dilatation of the TKE. As the volume is averaged while considering the mixing region growth, the advection term is equal to zero and only the dilatation of TKE remains in the flux. Therefore, the TKE budget equation is reduced as follows:

$$\frac{\partial k(\mathbf{x}, t)}{\partial t} = -\varepsilon_k(\mathbf{x}, t) - \left| k(\mathbf{x}, t) \frac{\partial u_j(\mathbf{x}, t)}{\partial x_j} \right|. \tag{4.18}$$

We apply this equation to shearless compressible turbulent mixing with gradients in turbulent intensity. For turbulent mixing, the energy flux term, which is reduced as the dilatational TKE, has different signs towards each interface because energy fluxes through the energy gradients, i.e., from the higher- to lower-energy regions; therefore, the higher-energy region is deprived of energy, which is accumulated in the lower-energy region. Hence, the dilatational TKE accelerates the decay process in the higher energy region because of the energy loss, whereas the decay rate decreases in the lower energy region because the transferred energy is accumulated. Consequently, the energy flux term in Eq. (4.18) can be described as a difference in dilatation between region 1 and 2, which is negative in the region 2 (energy loss) and positive in the region 1 (energy gain), respectively. The temporal decay of the TKE is described as

an exponential function of time and dilatation differences between the higher- and lower-energy regions:

$$\frac{\langle k \rangle}{\langle k_0 \rangle} = exp\left[-\left(c_1 \left(t/\tau\right) \pm c_2 \int_0^t \left\langle \left| \frac{\partial u_z(z,t)}{\partial z} \right| \right\rangle_2 - \left\langle \left| \frac{\partial u_z(z,t)}{\partial z} \right| \right\rangle_1 dt \right) \right], \quad (4.19)$$

where c_1 is acquired as dissipation quantity, and c_2 depends on the flow conditions. Here, we assume that $\int_{z_0}^{h} \left| k(\mathbf{x},t) \frac{\partial u_j(\mathbf{x},t)}{\partial x_j} \right| dz \approx \int_{z_0}^{h} k(\mathbf{x},t) dz \times \int_{z_0}^{h} \left| \frac{\partial u_j(\mathbf{x},t)}{\partial x_j} \right| dz$. The temporal decay of TKE is shown in Fig. 4.8 for turbulent mixing with different intensity gradients in the region 1, the mixing region, and region 2, respectively. The TKE in each region decays as an exponential function in time but shows different decay rates depending on the turbulent intensity. Case 1 corresponds to homogeneous isotropic turbulence and has no change in the decay rate compared to HIT. However, for Cases 2 and 3, the decay rates depend on the intensity of region 2. As energy is transferred from the higher energy region 2 into region 1, the turbulence decays more slowly in the region 1 because of transferred energy; thus, the decay rates decrease compared to the HIT case. Conversely, in the mixing region and region 2, the TKE decays faster than HIT due to energy loss; thus the decay rates increase. Therefore, these differences between HIT and flows in each region indicate energy loss/gain transferred by dilatation, which is described as dilatation differences with different signs in Eq. (4.19). Fig. 4.8(d-f) shows the decay of TKE as a function of scaled time, as calculated using the scaling law in Eq. (4.19) with $c_1 = c_\varepsilon/3$ and $c_2/c_1 \approx 2/9$. As a result, the discrepancy between HIT and turbulent mixing in regions 1 and 2 can be compensated by considering dilatation, and the flows in turbulent mixing decay at the same rate as that in HIT. Therefore, the proposed scaling law expresses the decay of TKE in compressible turbulent mixing by considering energy gain or loss by dilatation in the lower- and higher-energy regions, respectively.

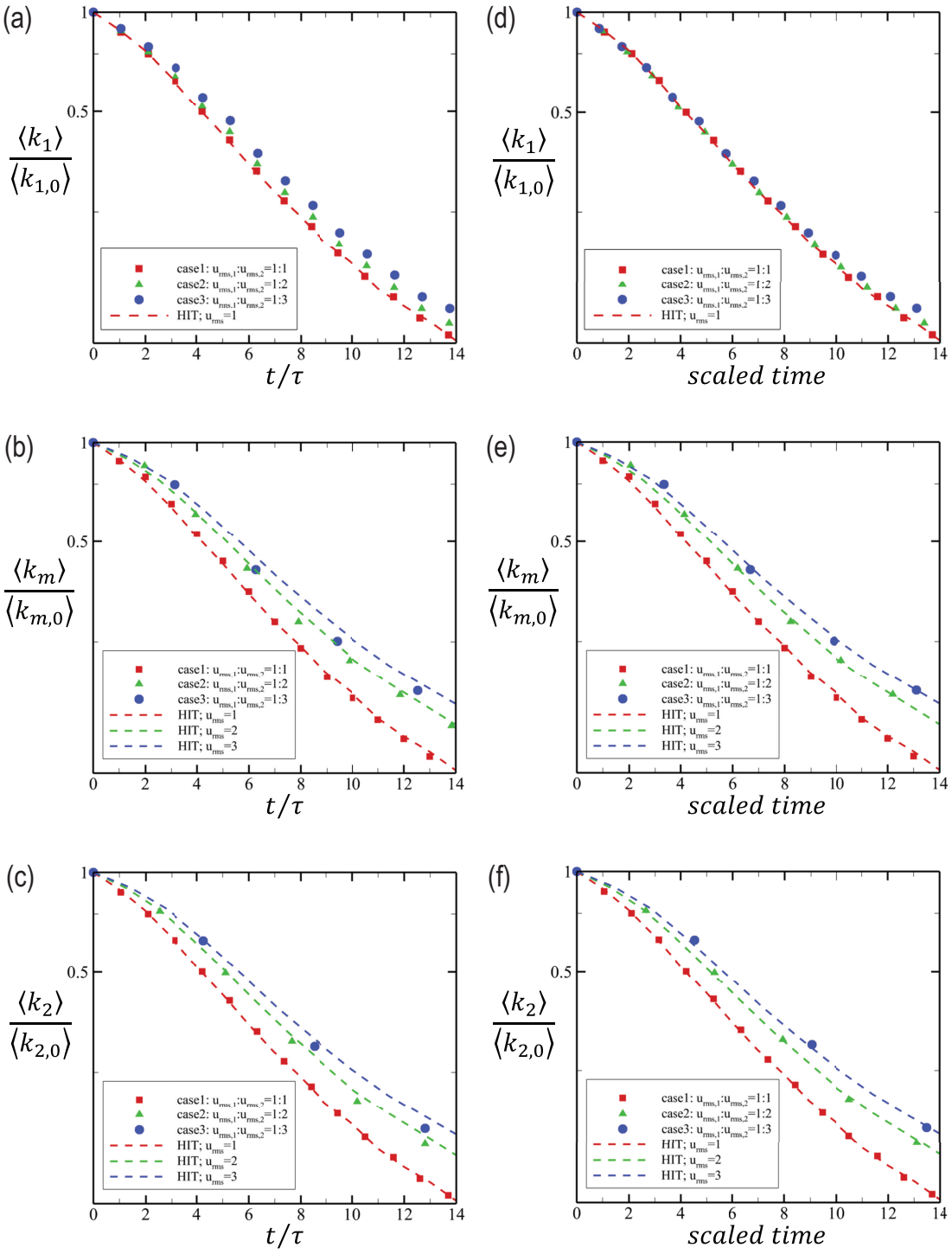

Figure 4.8: Temporal evolution of TKE in region 1 (*a,d*), the mixing region (*b,e*), and region 2 (*c,f*) for case 1 (red, square), case 2 (green, delta), and case 3 (blue, circle) as a function of time normalized by eddy turnover time (*a,b,c*) and the scaled time applying Eq. 4.19 (*d,e,f*). The results are compared with HIT (dotted lines).

4.5.2 Scaling of Dilatation in Shearless Turbulent Mixing

Dilatation affects the decay of TKE in turbulent mixing via energy transfer from the higher- to the lower-energy regions, as described in Eq. (4.19). Therefore, we evaluate the volume-averaged dilatation in regions 1 and 2. The volume-averaged dilatation integrated in time defined as

$$\theta = \frac{1}{t}\int_0^t \left\langle \left| \frac{\partial u_z}{\partial z} \right| \right\rangle / \left\langle \left| \frac{\partial u_z}{\partial z} \right| \right\rangle_0 dt. \tag{4.20}$$

Fig. 4.9 shows θ and turbulent Mach numbers as a function of time. The time-averaged dilatation does not significantly change with respect to time and remains close to 1.0. Therefore, by applying $\theta = 1$, the scaling for the decay of TKE in Eq. (4.19) can be revised as follows:

$$\frac{\langle k \rangle}{\langle k_0 \rangle} = exp\left[-\frac{c_\varepsilon}{3}\frac{t}{\tau}\left(1 \pm \frac{2}{9}\Phi_0\tau\right)\right], \tag{4.21}$$

where $\Phi_0 = \left\langle \left| \frac{\partial u_z}{\partial z} \right| \right\rangle_0$ is the initial volume- and time-averaged dilatation. The dilatation in compressible turbulent mixing contributes to enhancing or decreasing the decay rate. However, at late times ($t \gtrsim 6\tau$), θ decreases slightly with time, deviating from the value of unity. The results indicate that θ goes below unity when $Ma_t \lesssim 0.05$. In the regime of $Ma_t \lesssim 0.05$, The proportion of dilatational energy in the total energy decreases significantly (*Sethuraman and Sinha*, 2020); thus the compressibility is not strong enough to transfer energy. Therefore, the scaling law for decaying TKE in shearless turbulent mixing can effectively predict the physics as long as the turbulent Mach number is greater than 0.05.

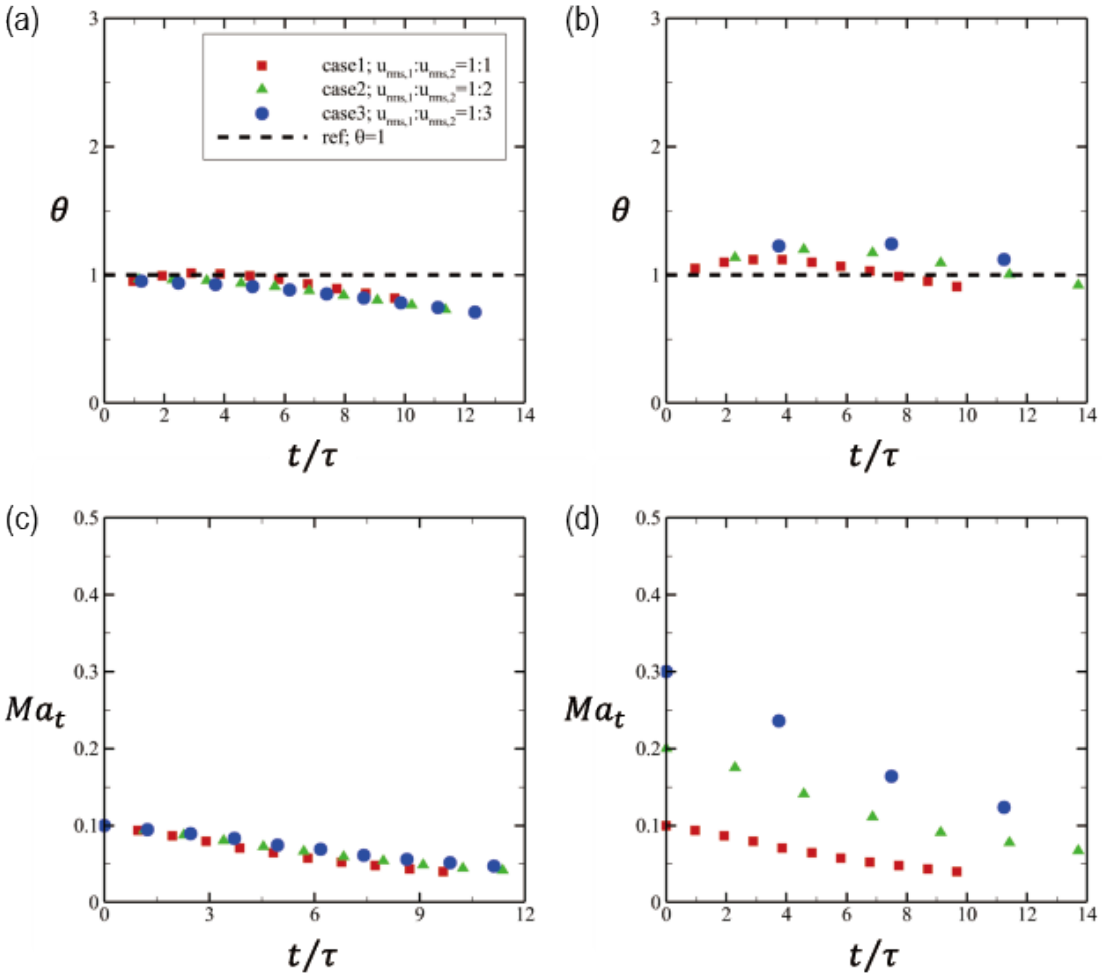

Figure 4.9: Time evolution of the volume- and time-averaged dilatation (a,b) and turbulent Mach numbers (c,d) for case 1 (red, square), case 2 (green, delta), and case 3 (blue, circle), averaged in region 1 (a,c) and region 2 (b,d), respectively.

4.6 Conclusions

We conduct DNS to investigate the effects of compressibility on turbulent/turbulent mixing with different turbulent intensities and develop a scaling for the growth of the mixing region and the decay of TKE for shearless compressible turbulent mixing. Kolmogorov's classical turbulence theory, which assumes incompressible, homogeneous, isotropic turbulence, cannot be applied to compressible turbulent mixing. To evaluate the effect of inhomogeneity in turbulent intensities, we initially juxtapose HIT fields with different u_{rms} magnitudes. We use shearless turbulence to isolate the role of turbulent intensity gradients in turbulent mixing while eliminating the effect of mean shear. Along the turbulent/turbulent interface, higher-intensity fluid penetrates deeper into the lower-intensity region. Deviations in the kurtosis suggest intermittent behavior. The PDFs of dilatation are skewed toward the negative, thus indicating a greater propensity toward compression. We observe the mixing region develops as a power law in time with the exponent 0.43, which scales consistently with the initial Taylor microscale and eddy turnover time.

In turbulent/turbulent mixing, the TKE evolution in the mixing region depends on net energy fluxes due to the differential in turbulent kinetic energy, which is transferred via dilatational TKE across the confines of the mixing region. As a result, the TKE decays as an exponential function of both the time and dilatation, which are derived from the viscous dissipation and dilatation of TKE. The energy transfer from the higher- to the lower-energy regions causes a change in the decay rate of TKE. In the higher-intensity region, energy loss enhances the decay rate, whereas the decay rate decreases in the lower-intensity region because of the accumulated energy. The new scaling for the temporal evolution of TKE describes these energy fluxes as differences in dilatation between the higher- and lower-energy regions. Furthermore, the averaged dilatation θ is invariant in time for $Ma_t \lesssim 0.05$, which leads to completing the scaling in terms of the initial dilatation. Therefore, the decay of TKE can be

determined as an exponential function of time, dissipation quantity (Reynolds number), initial u_{rms}, initial Taylor microscale, and initial dilatation. In future work, we will focus on the geometrical effects of compressible turbulent mixing.

CHAPTER V

Geometrical Effects of Compressible Turbulent Mixing

5.1 Abstract

While turbulent/non-turbulet mixing has been investigated in planar geometries including in the compressible regime, convergence and divergence effects (e.g., cylindrical or spherical geometries) on the mixing are unknown. Direct numerical simulations (DNS) are performed to determine the role of geometrical effects on the mixing of turbulence adjacent to the non-turbulent flow. A cylindrical region of shear-free homogeneous isotropic turbulence (HIT) with different root-mean-square velocities (u_{rms}) are initialized in an otherwise stationary flow. Over time, the turbulent kinetic energy (TKE) decays and a mixing region develops. Dimensional analysis is performed to determine the temporal growth of the mixing region. A self-similarity behavior with $t^{1/2}$ is observed for the cylindrical case, compared to the well-known result of $t^{2/3}$ for the planar case. This result agrees well with the DNS. The exponentially decaying scaling of TKE in time accounting for energy transfer by dilatation and viscous dissipation is extended to account for the diverging geometry. This scaling is valid for the cylindrical geometry because the dissipation rate depends on the initial HIT field and therefore is the same for the cylindrical and planar cases. However, the

role of the geometrical effect becomes apparent in energy transfer by dilatation.

5.2 Introduction

In a variety of flows including jets, wakes, and mixing layers, a region of turbulence is adjacent to the non-turbulent region (e.g., irrotational or laminar), such that mixing occurs between the two regions. At the turbulent/non-turbulent interface (TNTI), a turbulent mixing region develops as enstrophy in the turbulence is transported into the non-turbulent region, and the turbulence entrains non-turbulent patches of fluid into the turbulent region. The entrainment of large scales and turbulent diffusion on small scales determine the interface dynamics by transferring mass, momentum, and energy. The large-scale motions hold the dynamics in the turbulent/non-turbulent mixing layer, whereas the intensive vortical structures diffuse towards the non-turbulent region. According to these large- and small-scale dynamics, the growth was shown to be self-similar, which makes it possible to scale the mixing quantities (*Ishihara et al.*, 2013; *Kwon et al.*, 2014; *da Silva et al.*, 2014a,b; *Eisma et al.*, 2015): the temporal evolution of the mixing layer is proportional to the Taylor microscale (*Dimotakis*, 2000; *Bisset et al.*, 2002; *Gaskin et al.*, 2004; *Westerweel et al.*, 2005; *Hunt et al.*, 2006), while it was shown to scale with the Kolmogorov scale in shearless turbulence (*Mathew and Basu*, 2002; *Chauhan et al.*, 2014; *Breda and Buxton*, 2019; *Zecchetto and da Silva*, 2021). However, it remains under debate which length scale determines the mixing mechanisms in the TNTI.

Turbulent/non-turbulent mixing in a planar geometry was explored in Chapter III. They observed that additional energy transfer away from the mixing region occurs since there is no reciprocal transfer from the non-turbulent region and derived an expression for the time evolution of the turbulent kinetic energy (TKE). The effect of geometry (e.g., cylindrical or spherical) on TNTI has been investigated (*Bell*, 1951; *Plesset*, 1954; *Mikaelian*, 1990; *Kumar et al.*, 2003; *Mikaelian*, 2005; *Yu and Livescu*,

2008; *Lombardini and Pullin*, 2009; *Mankbadi and Balachandar*, 2012; *Lombardini et al.*, 2014a,b). The interfacial instability that develops in a non-planar geometry involves different physics. For instance, the distances between vortical structures are changed for diverging or converging interfaces, which affects their interactions. *Lombardini et al.* (2014a) studied turbulent mixing evolving from the interaction of a shock with a perturbed interface between fluids of different densities in a spherical geometry. Owing to the interface geometry, the growth of the interface is radially accelerated or decelerated, and its rate is different from that in a planar geometry because the interface converges or diverges as a result of the shock. *Yu et al.* (2021) used direct numerical simulation (DNS) and large-eddy simulation to investigate the evolution of an initially spherical region of incompressible homogeneous isotropic turbulence. They found that the turbulence remains homogeneous in the deep region near the center and obeys Saffman's decay law. They observed the intermittent ejection of integral-scale structures, e.g., vortex rings, from the interface. Furthermore, *Lombardini et al.* (2014b) observed anisotropy at large scales in spherical turbulent mixing. Although directional Taylor microscales exhibit radial anisotropy, the flow is isotropic at the Kolmogorov scale. *Mathew and Basu* (2002) found that small-scale structures are dominant in entrainment at the TNTI of a cylindrical jet flow. The cylindrical flow showed behavior different from that of a planar mixing layer because vortex rings are generated and break down near the interface.

Compressibility complicates the analysis as thermodynamics are coupled to the flow dynamics (*Lele*, 1994). Pressure-dilatation acts as compressible dissipation and acts to reduce the growth of TKE (*Sarkar et al.*, 1991; *Sarkar*, 1992). Energy transfer to the far field by acoustic radiation is generated for inhomogeneous compressible flows. These compressibility effects produce changes in pressure and velocity fields, which can be decomposed into solenoidal and dilatational parts. The behaviour of the solenoidal velocity field is similar to that of an incompressible flow; thus, its quan-

tities can be scaled well with classical turbulence theory (*Jagannathan and Donzis*, 2016). However, the dilatational part of the flow fails universality in scaling with the Kolmogorov theory (*Donzis and John*, 2020). Therefore, the scaling of compressible flow should be further studied.

The role of compressibility on turbulent mixing is discussed in Chapter III for planar geometries, i.e., a planar turbulent front. The growth rate of the mixing layer is expected to follow a power law with the exponent of 2/3, which corresponds to the analysis of *Barenblatt et al.* (1987). In compressible turbulent mixing with gradients in intensity, dilatation transfers energy from higher- to lower-energy regions, which enhances the decay of TKE. This investigation is extended to determine the geometrical effects of turbulent mixing. The goal of this work is to understand the role of geometry in compressible turbulent/non-turbulent mixing, in particular on the mixing region growth and the turbulence in the mixing region. The focus is on cylindrical geometries: an initially cylindrical region of shearless homogeneous isotropic turbulence is placed in a stationary fluid and left to freely evolve. Dimensional analysis and direction numerical simulation are used to predict the time evolution of the mixing region growth and of the turbulent kinetic energy of the flow, while energy budget analysis is used to examine the mechanisms responsible for this behavior. This paper is organized as follows. The problem under consideration and governing equations are described in Section 5.3. Section 5.4 introduces the geometrical effects on the development of the mixing region and the decay of TKE for planar and cylindrical geometries. Section 5.5 summarizes the findings.

5.3 Problem Setup

We examine differences in the propagation of a turbulent front in two dimensions (2D cylindrical geometry) compared to one dimension (1D planar geometry). Fig. 5.1 shows schematics of the initial turbulent fields for 1D planar and 2D cylindrical

geometries. Each turbulence field is initialized in a periodic cube of size $L = 2\pi$, generated by the initialization of *Rogallo* (1981) and the rescaled process of *An and Johnsen* (2018). This field achieves an equilibrium state with the desired properties from the beginning. The characteristic length d_0 for the 2D case is the diameter, while for the 1D case, it is the width. Uniform grids of 512 points per L are used, which are sufficient to resolve all dynamic scales of motion (*Movahed and Johnsen*, 2015; *Pan and Johnsen*, 2017). Periodic boundary conditions are applied in all directions. The turbulence has initial root-mean-square velocity u_{rms}, while the outer region is stationary with zero velocity. Table 5.1 lists the initial conditions. Turbulent physics with different initial root-mean-square velocities and the corresponding Reynolds numbers and turbulent Mach numbers are explored, but the density, pressure, and temperature are set to be constant: $P_0 = T_0 = 8\pi^2$. The initial Reynolds numbers based on the Taylor microscale and turbulent Mach number are defined as follows:

$$Re_\lambda = \frac{u_{rms}\lambda}{\nu}, \quad Ma_t = \frac{u_{rms}}{\langle c \rangle}, \tag{5.1}$$

$$u_{rms} = \sqrt{\frac{\langle u_i u_i \rangle}{3}}, \quad \lambda = \frac{\langle u_i^2 \rangle}{\left\langle \left(\frac{\partial u_i}{\partial x_i} \right)^2 \right\rangle} \tag{5.2}$$

where $\langle \cdot \rangle$ denotes a volume-averaged quantity, u_{rms} the root-mean-square velocity, c the sound speed, ν the kinematic and λ the Taylor microscale.

In shearless turbulence, the flow decays only as a result of viscous diffusion, with no superposed effects caused by the shear force or energy production. Therefore, only the dissipation rate in the TKE budget plays a role in decaying the TKE as follows:

$$\frac{\langle k \rangle}{\langle k_0 \rangle} = exp\left[-\frac{c_\varepsilon}{3} \left(t/\tau \right) \right], \tag{5.3}$$

where $k = u_i u_i/2$ is the TKE per mass, $c_\varepsilon = \langle \epsilon \rangle L_f / u_{rms}^3$ the dissipation quantity, L_f the volume-averaged integral scale, and τ the initial eddy turnover time. For

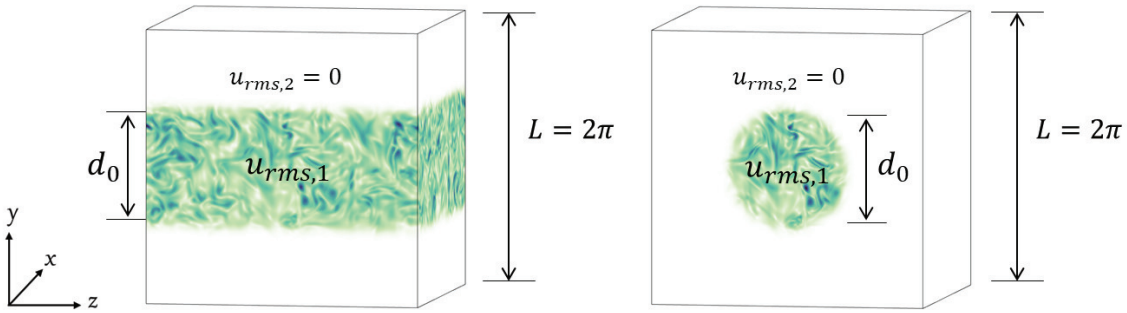

Figure 5.1: Configurations of initial setups for shearless, compressible turbulence with different geometries, planar and cylindrical, in a cube of volume L^3. The initial root-mean-square velocity magnitude $u_{rms,_1}$ varies, but the viscosity is constant.

	geometry	d_0/L	λ_0/L	$u_{rms,_1}$	$Re_{\lambda_{0,1}}$	$Ma_{t_{0,1}}$
case1	plane (1D)	0.5	0.25	1	100	0.1
case2	plane (1D)	0.5	0.20	2	156	0.2
case3	cylinder (2D)	0.5	0.25	1	100	0.1
case4	cylinder (2D)	0.5	0.20	2	156	0.2

Table 5.1: Summary of initial parameters for the different cases under consideration.

shearless flow, the Taylor microscale can be assumed to be constant in decaying shearless turbulence in an early process.

5.4 Results

5.4.1 Evolution of the Mixing Region

We examine the time evolution of the mixing region width and seek to determine its scaling in time. Fig. 5.2 shows a schematic diagram of the mixing region for the 2D geometry. The outer, inner, and initial radii are r_{out}, r_{in}, and r_0, respectively, and outer and inner mixing region widths are defined as $h_{out} = r_{out} - r_0$ and $h_{in} = r_0 - r_{in}$, respectively. We consider both diverging and converging of the outer and inner interfaces, which are not observed in the 1D geometry. As described in

Chapter III, for turbulent/non-turbulent mixing, the turbulence has vortical structures, which entrain the non-turbulent region, and diffuses at small scales across the TNTI, which generates fluctuations in the non-turbulent flow and advances the interface toward the non-turbulent region; consequently, the mixing region grows. For the outer mixing region h_{out}, the propagation of the interface separating the turbulent and non-turbulent regions can be described as a power law because the mixing region in shearless turbulent mixing is self-similarity in time. We can use dimensional analysis to develop a scaling for the outer width of the mixing region.

$$Q_{1d} = k_0 d_0 [L^3 T^{-2}] \; or \; Q_{2d} = k_0 A_0 [L^4 T^{-2}],$$
$$t[T],$$
$$h_{out}[L]$$

$$h_{out,1d} \sim Q_{1d}^{1/3} t^{2/3} \tag{5.4}$$

$$h_{out,2d} \sim Q_{2d}^{1/4} t^{1/2} \tag{5.5}$$

Here, Q is the initial TKE per mass, and d_0 and $A_0 = \pi r_0^2$ are the initial diameter of the plane and initial area of the cylinder, respectively. For turbulence with a 1D geometry, the mixing region grows as a power law of 2/3 in time for $h(t) \ll r_0$ (*Barenblatt et al.*, 1987). For the 2D geometry, dimensional analysis suggests that the growth rate is 1/2.

Fig. 5.3 shows the temporal evolution of the outer and inner mixing regions for 1D planar and 2D cylindrical turbulence geometries. The DNS results with different u_{rms} magnitudes show consistency with the dimensional analysis of Eqs. (5.4) and (5.5), which follow the power law with the expected exponents. For the 1D geometry in Fig. 5.3(a-b), the outer and inner interfaces symmetrically propagate at a rate of 2/3, which is consistent with the dimensional analysis of Eq. (5.4). Likewise, in Fig.

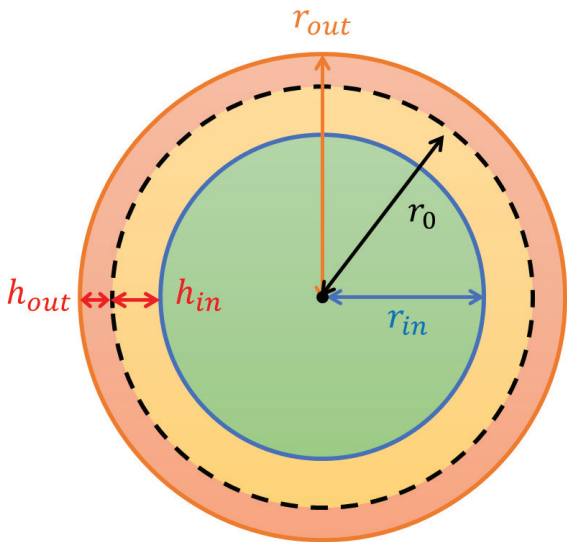

Figure 5.2: Schematic of the mixing region for the 2D geometry. Based on the initial radius r_0, the outer and inner mixing region widths are defined as $h_{out} = r_{out} - r_0$ and $h_{in} = r_0 - r_{in}$, respectively.

5.3 (c), the outer mixing region width in the 2D case develops as a power law of 1/2, as obtained in Eq. (5.5). However, in contrast to the 1D geometry, the radii of the inner interface gradually decrease. For the inner mixing region width h_{in}, the radius r_{in} decreases as the interface propagates toward the center of the cylinder.; therefore, the converging geometry enhances the mixing, and h_{in} grows faster than the width of the outer mixing region h_{out}. The growth exponent of the inner interface obtained from the DNS is $4/5$. Therefore, the scalings of the mixing region widths for 1D planar and 2D cylindrical turbulence can be summarized as follows:

$$h_{out,1d} = h_{in,1d} \sim \left(t/\tau\right)^{2/3}, \tag{5.6}$$

$$h_{out,2d} \sim \left(t/\tau\right)^{1/2}, \tag{5.7}$$

$$h_{in,2d} \sim \left(t/\tau\right)^{4/5}. \tag{5.8}$$

Here, the turbulence characteristics are determined by the parameters of the initial TKE Q, initial Taylor microscale λ_0, and the eddy turnover time τ. The scaling

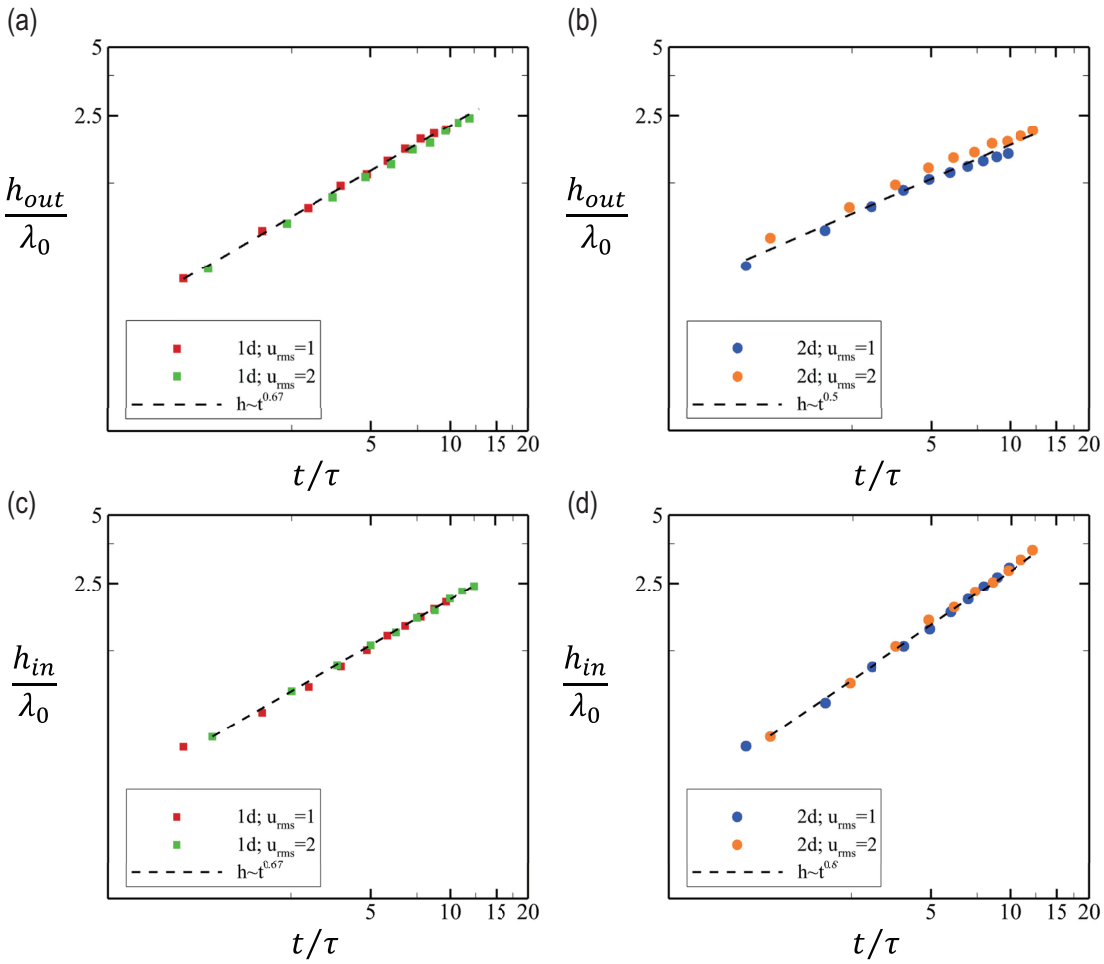

Figure 5.3: Growth of the mixing region width relative to d_0 for the (a, c) 1D and (b, d) 2D geometries. The thickness of the outer (a, b) and inner (c, d) layers are separately evaluated. The mixing region width h propagates as a power law with exponents of 2/3 and 1/2 for the 1d and 2d cases, respectively.

indicates that the evolution of the mixing region is influenced by the large-scale structures with a length scale of the Taylor microscale.

To estimate the radius of the inner interface r_{in} in cylindrical turbulent mixing, we leverage the characteristics of the passive scalar. Fig. 5.3(a-b) show that the passive scalar exhibits symmetric development of the mixing region for the outer and inner interfaces in the 1D geometry. Thus, we hypothesize that fluxes of mass and energy generate mass and energy exchanges through the surface of the interface, which are

conserved in the volume of the mixing region. This hypothesis implies that the areas of the outer and inner mixing regions are the same in the cylindrical turbulent mixing of the passive scalar; $(r_{out}^2 - r_0^2)\,\pi = (r_0^2 - r_{in}^2)\,\pi$. This approach makes it possible to derive the inner radius r_{in} as follows:

$$r_{in}^2 = 2r_0^2 - r_{out}^2. \tag{5.9}$$

The time evolution of the inner radius r_0 is compared with the results from Eq. (5.9) in Fig. 5.4. This approach using Eq. (5.9) accurately predicts the propagation of the inner interface at early times ($t \leq 5\tau$), but the inner radius deviates from the estimation at later times. It is presumed that the interactions between vortical structures are enhanced as the inner radius decreases. These interactions produce larger structures near the TNTI and accelerate the growth of the mixing compared to the outer region of the mixing layer, in which the distance between turbulent structures gradually increases over time.

5.4.2 Decay of Turbulent Kinetic Energy

Because the TKE decays only by viscous dissipation for shearless HIT, the TKE balance equation can be reduced as follows:

$$\frac{d\,\langle k\rangle}{dt} = -\langle\varepsilon\rangle, \tag{5.10}$$

where $\langle\cdot\rangle$ represents the spatial volume-averaged quantity, and k and ε denote the TKE per mass and the dissipation rate, respectively. For shearless turbulence, the smallest scale, that is the dissipative (Kolmogorov) scale, diffuses predominantly; therefore, scales larger than the dissipative scale are invariant during the decay process. Hence, the Taylor microscale sets to be constant ($\lambda \approx \lambda_0$). As a result, the decay of TKE is obtained as an exponential function of time, and the decay rate is

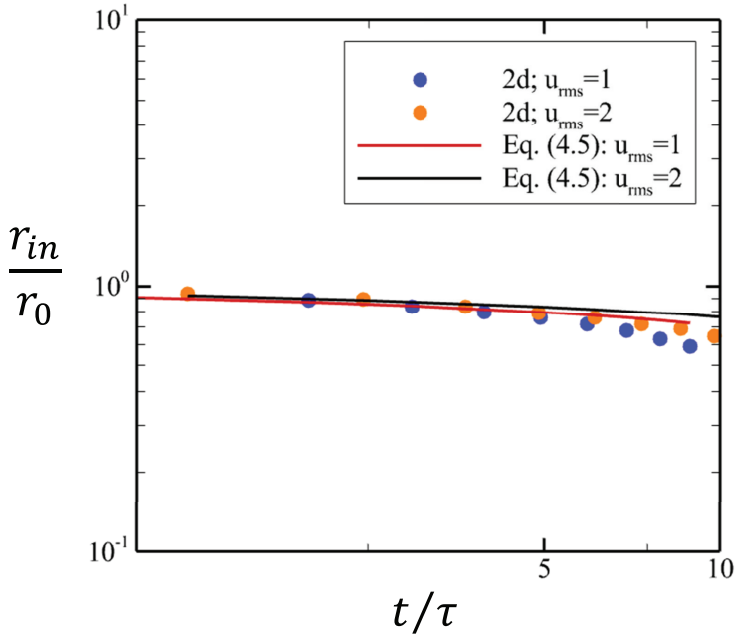

Figure 5.4: Time evolution of the inner radius r_{in} for turbulent mixing with different u_{rms} magnitudes in a 2D geometry. The DNS results (circles) are compared with the results from Eq. (5.9) (solid lines).

determined by the dissipation quantity c_ε as Eq. (5.3), as determined in Chapter III.

In Chapter III, we demonstrate that TKE convection due to dilatational motions must be accounted for in the propagation of planar turbulence. It is further expected that a diverging geometry would need to be taken into account in the energy balance. The temporal decay of TKE for the 1D and 2D cases with different initial u_{rms} magnitudes are shown in Fig. 5.5 with comparison to HIT. As expected from Eq. 5.3, the HIT decays exponentially over time, whereas turbulence decaying near a non-turbulent region decays more rapidly. In particular, the 2D geometry exhibits the fastest decay rate. To determine the reason for the discrepancy in the decay rates, we examine the TKE equation for inhomogeneous compressible turbulence:

$$\frac{\partial k(\mathbf{x},t)}{\partial t} = -\varepsilon_k(\mathbf{x},t) - \left| k(\mathbf{x},t)\frac{\partial u_j(\mathbf{x},t)}{\partial x_j} \right|, \tag{5.11}$$

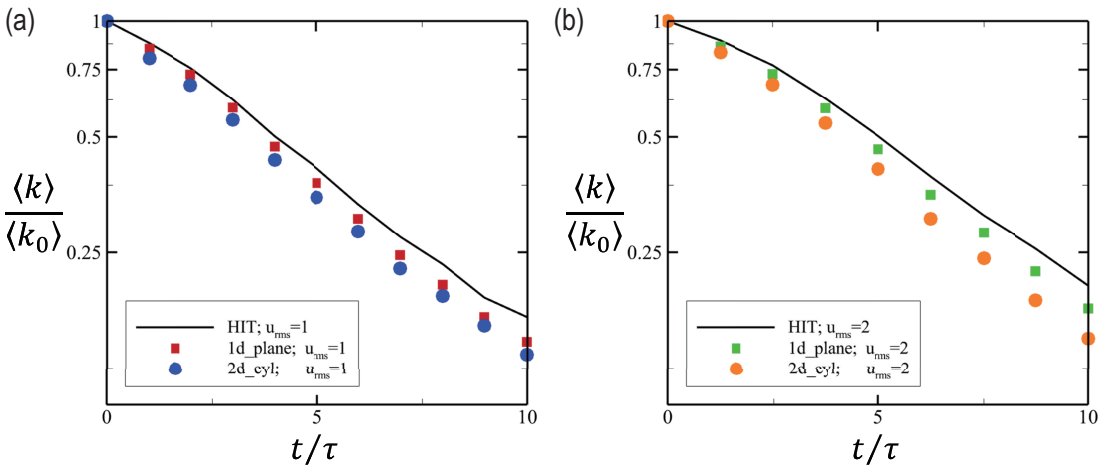

Figure 5.5: Temporal decay of TKE for 1D planar (square) and 2D cylindrical (circle) turbulence geometries. Two different u_{rms} magnitudes are considered, that are (a) $u_{rms} = 1$ and (b) $u_{rms} = 2$, which are compared with homogeneous isotropic turbulence (black, solid line).

where the temporal decay of the TKE is equivalent to the dissipation rate and dilatational TKE. Fig. 5.6 shows the dissipation rate as a function of time for the 1D and 2D geometries with different initial turbulent intensities. The dissipation rate is determined by the initial turbulent intensity and length scale and thus the Reynolds number and turbulent Mach number. However, the dissipation rate is relatively insensitive to the initial geometry (1D planar vs. 2D cylindrical). Therefore, the discrepancy in TKE between the 1D and 2D cases can thus be attributed to compressibility effects for inhomogeneous flows, i.e., the last term in Eq. (5.11). This equation can be rewritten for 1D planar and 2D cylindrical turbulence as follows:

$$\frac{\langle k \rangle}{\langle k_0 \rangle} = exp\left[-\left(c_1 \left(t/\tau \right) + c_2 \int_0^t \left\langle \left| \frac{\partial u_z(t)}{\partial z} \right| \right\rangle dt \right) \right], \tag{5.12}$$

$$\frac{\langle k \rangle}{\langle k_0 \rangle} = exp\left[-\left(c_1 \left(t/\tau \right) + c_2 \int_0^t \left\langle \left| \frac{1}{r} \frac{\partial (r u_r(t))}{\partial r} \right| \right\rangle dt \right) \right]. \tag{5.13}$$

For homogeneous turbulence, fluxes going one way are on average canceled by fluxes

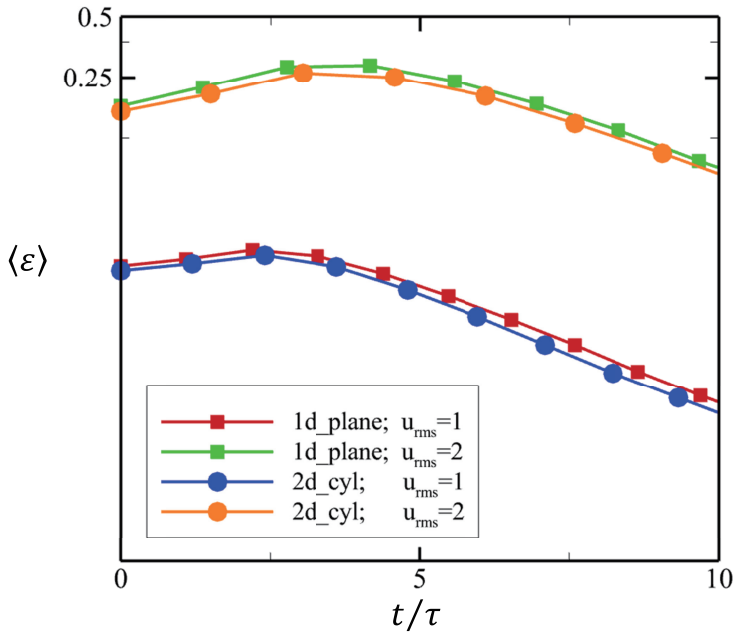

Figure 5.6: Dissipation rate as a function of time for 1D (square) and 2D (circle) geometries with $u_{rms} = 1$ and 2.

going the opposite way; thus, the volume-average is zero. However, at TNTIs, no such cancellation exists in the inhomogeneous direction. Therefore, the derivatives in those directions in the divergence of the velocity field, namely z and r derivatives for the 1D and 2D cases, respectively, are considered, that are dilatation in Eqs. (5.12) and (5.13).

We define the time- and volume-averaged dilatation in the turbulence region for 1D and 2D geometries as follows:

$$\theta_{1d} = \frac{1}{t}\int_0^t \left\langle \left| \frac{\partial u_z}{\partial z} \right| \right\rangle \Big/ \left\langle \left| \frac{\partial u_z}{\partial z} \right| \right\rangle_0 dt, \tag{5.14}$$

$$\theta_{2d} = \frac{1}{t}\int_0^t \left\langle \left| \frac{1}{r}\frac{\partial (r u_r(t))}{\partial r} \right| \right\rangle \Big/ \left\langle \left| \frac{1}{r}\frac{\partial (r u_r(t))}{\partial r} \right| \right\rangle_0 dt. \tag{5.15}$$

Fig. 5.7 shows the time evolution of the θ for the 1D and 2D cases with different

turbulent intensities. We observe that the volume- and time-average dilatation does not significantly change over time regardless of the geometry, which value is unity ($\theta = 1$). Therefore, Eqs. (5.12) and (5.13) can be rewritten as follows:

$$\frac{\langle k \rangle}{\langle k_0 \rangle} = exp\left[-\frac{c_\varepsilon}{3}\frac{t}{\tau}\left(1 + \frac{c_2}{c_1}\Phi_0\tau\right)\right]. \tag{5.16}$$

Here, Φ_0 is the initial volume-averaged dilatation, where $\Phi_0 = \left\langle \left| \frac{\partial u_z}{\partial z} \right| \right\rangle_{t=0}$ and $\left\langle \left| \frac{1}{r}\frac{\partial (r u_r(t))}{\partial r} \right| \right\rangle_{t=0}$, for the 1d and 2d cases, respectively. The dilatation contributes to increasing the decay rate of the TKE by a factor of $\frac{c_2}{c_1}\Phi_0\tau$. This increase in decay TKE rate is caused by dilatation, which transfers TKE from the turbulent to non-turbulent region, and leads to the enhanced decay rate. However, θ decreases to less than unity at a later time ($t > 7\tau$) because dilatation variance is almost dissolved when the turbulent Mach number is less than 0.05 (*Sethuraman and Sinha*, 2020); thus compressibility effects are not strong enough to transfer the TKE. Furthermore, the 2D case with a lower u_{rms} deviates from the reference value ($\theta = 1$) faster than in the 1D case owing to the larger energy losses through dilatation. Therefore, the scaling in Eq. (5.16) is valid for sufficiently high Ma_t and is consistent with the scaling law for turbulent/non-turbulent mixing and turbulent mixing.

To demonstrate the validity of the proposed scaling, Fig. 5.8 shows the time evolution of the TKE based on Eq. (5.16). All the cases with different geometries and initial u_{rms} magnitudes have the same decay rate as HIT because energy losses in compressible turbulence are well-compensated by the scaling shown in Eq. 5.16. For the 1D planar interface, the coefficient $c_2/c_1 = 1/9$ since this geometry is that of turbulent/non-turbulent mixing considered in Chater III. However, for the 2D case, this coefficient is empirically obtained as $\frac{1}{3}$. This larger coefficient is because the energy transfer in the radial direction has a larger effect on the decay of the TKE compared with the planar transfer.

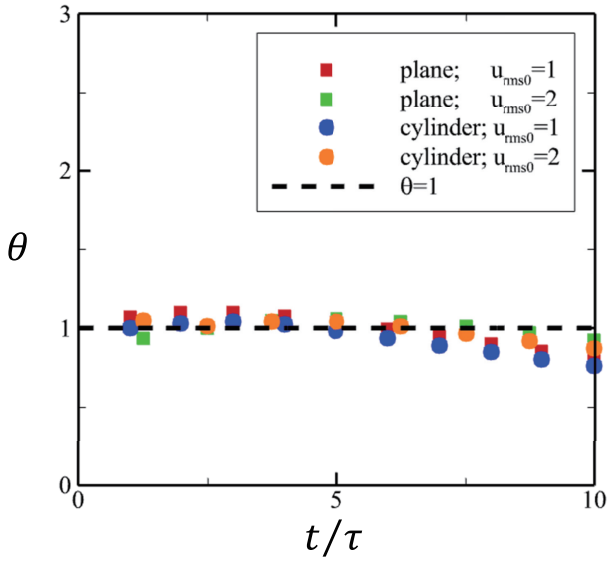

Figure 5.7: Time evolution of the time- and volume-averaged dilatation (θ) for 1D (square) and 2D (circle) geometries for two $u_{rms,1} = 1$ and 2. The reference value is unity (black, dashed line).

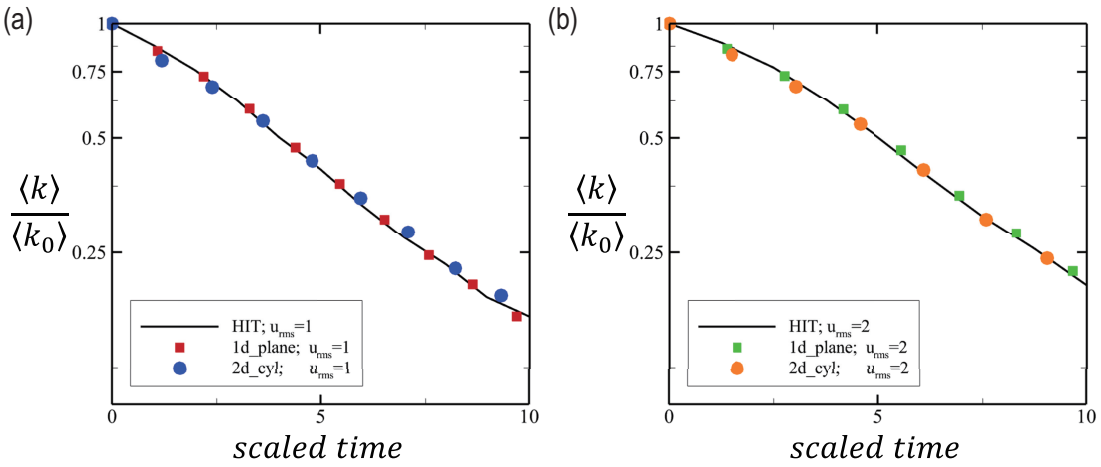

Figure 5.8: Time evolution of the TKE with (a) $u_{rms} = 1$ and (b) $u_{rms} = 2$. The turbulent flows of 1D (square) and 2D (circle) geometries are compared with HIT (black, solid line).

5.5 Conclusions

This study investigates the role of geometry in shearless, compressible, turbulent/non-turbulent mixing, where a turbulent front propagates into a non-turbulent region. Direct numerical simulations are conducted for two different geometries: initially planar (1D) and cylindrical (2D). The time evolution of the mixing region width and the turbulent kinetic energy is of particular interest as the Reynolds and turbulent Mach numbers are varied.

Simulations show that the non-turbulent flow is entrained by the turbulent flow, and the mixing region grows as the non-turbulent fluid patches are drawn into the turbulent region, and enstrophy is transported by viscous diffusion across the TNTI. During this turbulent diffusion process, the turbulent/non-turbulent interface propagates into the non-turbulent region as a mixing region develops. The mixing region width h evolves as a power law in time with time exponents depending on the geometry. Dimensional analysis arguments suggest a $t^{1/2}$ growth for the 2D geometry, by contrast to the $t^{2/3}$ growth observed in the 1D case. These results are confirmed by the DNS results and hold for different initial turbulent intensities.

For compressible flows, the geometry of turbulence affects the TKE decay. Because there is no reciprocal TKE flux coming from the non-turbulent region, energy transfer from the turbulent to the non-turbulent regions occurs in turbulent/non-turbulent interfaces. We show that this transfer is affected by the initial geometry as dilatation for the 2D case propagates in the radial direction, which generates a larger effect compared to the 1D case. As a result, the TKE decays exponentially in time with the enhanced decay rate, described by initial dilatation with coefficients of 1/9 for 1D and 1/3 for 2D geometries. The results of this study can help clarify the physics of turbulent mixing in 2D geometries and develop models for various applications with non-planar geometries.

CHAPTER VI

Conclusion and Future Directions

This chapter summarizes the Ph.D. study presented in this thesis and suggests future directions for further understanding turbulence physics.

6.1 Summary and Concluding Remarks

Turbulent mixing plays an important role in many applications such as geophysical flows in the ocean or atmosphere, astrophysical flows like supernova remnants and mixing with molecular clouds, and engineering applications such as jets and boundary layer flow. However, the classical theory of homogeneous isotropic turbulence does not directly apply to problems with inhomogeneous directions of compressibility effects due to additional energy transfer mechanisms. The goal of this work is to understand the role of inhomogeneity and compressibility effects in turbulent mixing. To achieve this goal, we improve the process of generating the initial velocity field and conduct direct numerical simulations of shearless compressible turbulent mixing, which allowed us to

- Investigate inhomogeneity and compressibility effects in turbulent/non-turbulent mixing, thereby describing mixing region growth and the decay of turbulent kinetic energy. The mixing region develops as large-scale vortical structures entrain the irrotational flow, and the turbulent flow diffuses into the non-turbulent

region. We find that the interface separating turbulence from the non-turbulent region propagates as a power-law of $t^{2/3}$. During this process, fluctuations are generated in the non-turbulent flow. Dilatation transfer their turbulent kinetic energy (TKE) from the turbulent to the non-turbulent region, leading to an increased rate of decaying TKE compared to homogeneous isotropic turbulence (HIT). This energy loss is described as a triple moment transport of velocity in the turbulent energy balance equation. We suggest a new scaling law for the temporal decay of turbulent kinetic energy by considering the dilatational TKE, which predicts the physics in turbulent/non-turbulent mixing well.

- Extend the study of turbulent/non-turbulent mixing to investigate compressible turbulent mixing at gradients in turbulent intensities. Shearless turbulent fields are juxtaposed with different turbulent intensities, where turbulence decays by viscous diffusion. The use of shearless turbulence enables us to isolate the effect of intensity gradients in turbulent mixing. We find that the gradients in turbulent intensity cause flow penetration from higher to lower energy regions with intermittency, which is represented as spatially non-uniform kurtosis, the fourth-order moments of velocity derivatives. The probability density functions (PDFs) showed that the intermittency originates from the compressibility effect, i.e., dilatation. The PDFs of dilatation exhibit a negatively skewed distribution in contrast to the symmetric PDFs of vorticity. Moreover, turbulent mixing shows non-Gaussian behavior, whereas the PDFs of homogeneous isotropic turbulence follow a Gaussian distribution as described in Kolmogorov's theory. This result supports the new proposed scaling of decaying TKE, which describes energy transfer by dilatation in inhomogeneous flows. Furthermore, we improve this scaling for compressible turbulent mixing with different turbulent intensities. We use a passive scalar to quantify turbulence behavior, such as the mixing region width and the location of the interface separating

the mixing region and turbulent flows with higher and lower intensities. Since energy transfer by dilatation occurs through these interfaces, the higher- and lower-energy regions are involved in energy loss and gain, respectively, which are taken into account in the scaling. In addition, we find that time-averaged dilatation is invariant in time, and therefore describes the time-delay and time-advance of decaying turbulent kinetic energy in the higher- and lower-energy regions, respectively.

- Study the geometrical effects of turbulent/non-turbulent mixing. We consider turbulent flow in initially cylindrical geometry and compare it to the planar case from Chapter III. We investigate the temporal evolution of the mixing region and find that the propagation of interfaces separating turbulent flow from non-turbulent flow follows a power law in time of $t^{1/2}$, by contrast to $t^{2/3}$ in the planar case. These exponents are consistent with dimensional analysis. Geometrical effects modify energy transfer by dilatation, i.e., dilatation. We compare the decay of homogeneous isotropic turbulence and inhomogeneous compressible turbulence with planar and cylindrical geometries and find that larger energy loss occurs in cylindrical turbulence. The dissipation rates that determine the decay rate are invariant in time but depend on the root-mean-square velocity magnitude. Therefore, the discrepancy in energy loss is caused by energy flux, which is the dilatation-TKE. The magnitude of energy flux from turbulence to non-turbulent flow is larger for the cylindrical geometry than the plane, due to diverging geometry. Hence, geometrical effects appear in the scaling as different coefficients of dilatation, which explain the enhanced decay rate of TKE.

DNS of shearless flow is a powerful tool for improving turbulence modeling, as it allows the isolation of each effect in turbulent flow and eliminates coupled interactions with kinetic energy production. Our findings can contribute to providing a phenomenological understanding of shearless compressible turbulent mixing, partic-

ularly in predicting turbulent kinetic energy and mixing region width. We observe that dilatation generates additional energy transfer from higher- to lower-energy regions, affecting decay rates along with viscous dissipation. Furthermore, the time- and volume-averaged dilatation remains constant over time, introducing a novel parameter for the decay of turbulent kinetic energy in terms of the initial dilatation. The initial dilatation offsets the decay rates changed by the energy loss/gain in the higher- and lower-intensity regions. In contrast to inhomogeneity and compressibility effects, the mixing region width follows the analysis of incompressible flow. These findings provide phenomenological information to modify turbulence models for inhomogeneous and compressible flow. DNS results and the new scaling for the temporal evolution of turbulent kinetic energy and mixing region can be used to evaluate velocity and length scales in turbulence models. In particular, velocity components such as kinetic energy in the eddy viscosity model and turbulent viscosity hypothesis must account for energy transfer mechanisms caused by dilatation to obtain more accurate predictions for compressible turbulent mixing.

6.2 Future Research Directions

6.2.1 Improvements in the Generation of the Initial Turbulence Field and Numerical Schemes

The main characteristic of compressible flow is the coupling to the thermodynamics, which change the volume of fluid and involve energy exchange (*Lele*, 1994). In this thesis, we propose an improvement to the generation of the initial turbulent velocity field by rescaling the field in a spectral space in a way that the quasi-equilibrium state is obtained with desired properties. Further study should be needed for fluctuations of thermodynamic properties such as pressure, density, and temperature, which can be initially correlated with the velocity fields. Additionally, eddy shocklets

are not considered in the present work but are expected to become important for higher turbulent Mach numbers ($Ma_t \gtrsim 0.4$). Such a flow regime would introduce additional compressible dissipation. Such a regime would increase the decay rate of turbulent kinetic energy and generate additional mechanisms of turbulent mixing. To describe these physics, different numerical schemes are required to represent sharp discontinuities caused by shocklets; for instance, high-order accurate weighted essentially non-oscillatory (WENO) schemes can then be applied. This method enables the investigation of compressibility effects on turbulent mixing, which enhances inhomogeneity and involves different physics from the work presented in this paper, such as shock-turbulence interaction. Furthermore, there may be a need to develop improved shock-capturing schemes that do not introduce excessive dissipation.

6.2.2 Extension of the Scaling for the Decay of Turbulent Kinetic Energy

Mixing is commonly observed in various natural and engineering applications at regions of gradients in velocity and/or composition. Moreover, in Rayleigh-Taylor (RT) and Richtmyer-Meshkov (RM) instabilities, interfacial perturbations grow, and the mixing zone evolves. Density gradients, in addition to turbulent intensity gradients, can modify mechanisms in terms of vortical structures, energy transfer, and dissipation, but the contributions of each effect are poorly understood. For example, a supernova remnant consisting of multiple materials with different densities and turbulent fluctuations (*Castro et al.*, 2012; *Slane et al.*, 2015) experiences turbulent mixing as the shell expands and merges with the surrounding molecular clouds. However, it remains unclear how each parameter in this astrophysical flow contributes to developing hydrodynamic instabilities and mixing regions. Therefore, further study for turbulent mixing with different parameters should be conducted to predict the growth of the turbulent mixing zone and late behavior in RT and RM instabilities, which consists of several elements: gradients in density and/or turbulence intensity,

as well as gravity or shock. The current scaling for the temporal evolution of TKE describes compressible turbulent mixing with turbulent intensity gradients under the same initial density and length scales with no external forces. However, these parameters can generate non-linear interactions with the effect of turbulent intensity gradients and contribute to developing the mixing region. The role of gradients in density and length scale in turbulent mixing was investigated for shearless turbulent mixing. *Movahed and Johnsen* (2015) found that density gradients cause anisotropy in the Taylor scale, but the Kolmogorov scale remains isotropic. Furthermore, intermittency and skewness caused by anisotropy in length scale and kinetic energy gradients are observed in *Tordella and Iovieno* (2006, 2011). It may be possible to incorporate these effects into scaling for the growth of the mixing region and the decay of TKE. The density difference is expected to generate enhanced penetration, following a wider growth of the mixing region, and length scales near the interface may change the thickness of the mixing layer. There are terms in the TKE balance equation to describe these effects, which would no longer be negligible.

6.2.3 Spherical Geometry of Turbulence

The Kolmogorov theory is insufficient for describing turbulent flows involving compressibility, inhomogeneity, and geometrical effects. The TNTI, where the turbulent flow is adjacent to laminar regions, has been widely investigated for planar geometry, which accounts for one-dimensional non-uniformity. However, most applications in our lives involve turbulent mixing with non-planar geometries such as pipe flows, jet flows, and atmospheric and astrophysical flows. The compressible turbulent mixing with cylindrical geometry introduces additional energy transfer, as explored in Chapter III. Additionally, more complicated evolution and dissipation mechanisms are expected for spherical turbulent mixing, which do not follow the results of planar turbulent mixing because the radius of the mixing region changes over time. Diverg-

ing and converging interfaces may decelerate the mixing process and lead to more nonlinear interactions between eddies. Moreover, acoustic waves transfer energy in a three-dimensional radius direction, and therefore the geometrical effects cause excessive energy loss and enhance the decay process of TKE. As a result, the current scaling for the mixing region growth and the decay of TKE may need to be extended to predict these disparate characteristics for the propagation of spherical turbulence.

The computational setup would be the same as in previous works, involving initial shear-free HIT with appropriate Reynolds and turbulent Mach numbers. However, in this case, the turbulent region would have a spherical shape and would be surrounded by the stationary non-turbulent flow. Preliminary results suggest that intermittent large-scale structures eject from the turbulent region, which increases the growth rate of the mixing region. Additionally, energy loss caused by inhomogeneity and compressibility effects is magnified, while the dissipation rate remains consistent with that of planar and cylindrical turbulence. This study introduces an additional mixing characteristic, vortex ejection, which is a large-scale phenomenon distinct from entrainment.

APPENDICES

APPENDIX A

Helmholtz's Decomposition

The Helmholtz decomposition is a method to decompose a vector field $\mathbf{F}$ into the sum of dilatational (curl-free) and solenoidal (divergence-free) components, which is useful for analyzing characteristics of compressible flow. The vector field $\mathbf{F}$ can be written as

$$\mathbf{F}(\mathbf{r}) = -\nabla\phi + \nabla \times \mathbf{A} \tag{A.1}$$

where ϕ is a scalar potential and $\mathbf{A}$ is a vector potential function. The vector field consists of the gradient of ϕ and the curl of $\mathbf{A}$, which are curl-free and divergence-free terms; therefore, the vector fields satisfy $\nabla\times\nabla\phi = 0$ and $\nabla\cdot(\nabla \times \mathbf{A}) = 0$, respectively (*Davidson*, 2015). The two potential functions are solved as $\nabla^2\phi = -\nabla \cdot \mathbf{F}$ and $\nabla^2\mathbf{A} = -\nabla \times \mathbf{F}$, where

$$\phi(\mathbf{r}) = \frac{1}{4\pi}\int \frac{\nabla^{'} \cdot \mathbf{F}(\mathbf{r}^{'})}{|\mathbf{r} - \mathbf{r}^{'}|}dV^{'}, \tag{A.2}$$

$$\mathbf{A}(\mathbf{r}) = \frac{1}{4\pi}\int \frac{\nabla^{'} \times \mathbf{F}(\mathbf{r}^{'})}{|\mathbf{r} - \mathbf{r}^{'}|}dV^{'} \tag{A.3}$$

if $\mathbf{F}$ is unbounded. These solutions can be obtained by the Fourier transform in wavenumber space. The Fourier transform of $\mathbf{F}$ is denoted as $\mathbf{G}$, which is described

as

$$\mathbf{F}(\mathbf{r}) = \int \mathbf{G}(\mathbf{k}) \exp^{i\mathbf{k}\cdot\mathbf{r}} \, dV_k, \tag{A.4}$$

where $\mathbf{k}$ is the wave vector and i is the imaginary unit (*Pope*, 2000). The $\mathbf{G}(\mathbf{k})$ consists of the scalar field and vector field as:

$$\mathbf{G}(\mathbf{k}) = -i\mathbf{k}G_\phi(\mathbf{k}) + i\mathbf{k} \times \mathbf{G}_A(\mathbf{k}), \tag{A.5}$$

where each term is represented as

$$\mathbf{G}_\phi(\mathbf{k}) = i\frac{\mathbf{k} \cdot \mathbf{G}(\mathbf{k})}{||\mathbf{k}||^2}, \tag{A.6}$$

$$\mathbf{G}_A(\mathbf{k}) = i\frac{\mathbf{k} \times \mathbf{G}(\mathbf{k})}{||\mathbf{k}||^2}. \tag{A.7}$$

This approach helps efficiently manipulate the vector field and analyze two different physics in compressible turbulence.

APPENDIX B

Investigation of the Effect of Characteristic Length on 2D Cylindrical Turbulence

Passive scalar fields are examined to analyze turbulence behavior. The scalar is initially distributed with a smeared interface. The mixing region width is determined by the passive scalar, where the mass fraction of the scalar is between 0.25 and 0.75. In Fig. B.1 the mixing region growth in time is illustrated for turbulence with 2D cylindrical geometry. To determine the d_0 of the geometry, the initial radius r_0 is changed to $1/6L$, $1/5L$, and $1/4L$, where r_0 is defined as $d_0/2$. It is assumed that the outer and inner interfaces propagate as a power law but at different rates because the planar turbulence develops as a power law in self-similarity, as shown in Chapter V. For the 2D cylindrical turbulence, as seen in Fig. B.1(a), the outer interface propagates at the same rate until $t \lesssim 5\tau$, but the growth rate decreases for turbulence with $r_0 = 1/6L$ and $1/5L$. Furthermore, for the inner interface shown in Fig. B.1(b), all the cases have a much larger growth exponent than the outer interface. However, the power-law growth is destroyed for the turbulence of $r_0 = L/6$ and $L/5$ because the turbulent eddies are interrupted as the interface approaches the center. Therefore, the initial radius r_0 should be greater than the size of the turbulent eddies, which is the Taylor microscale. The turbulence with $r_0 = L/4 = 0.25L$, which

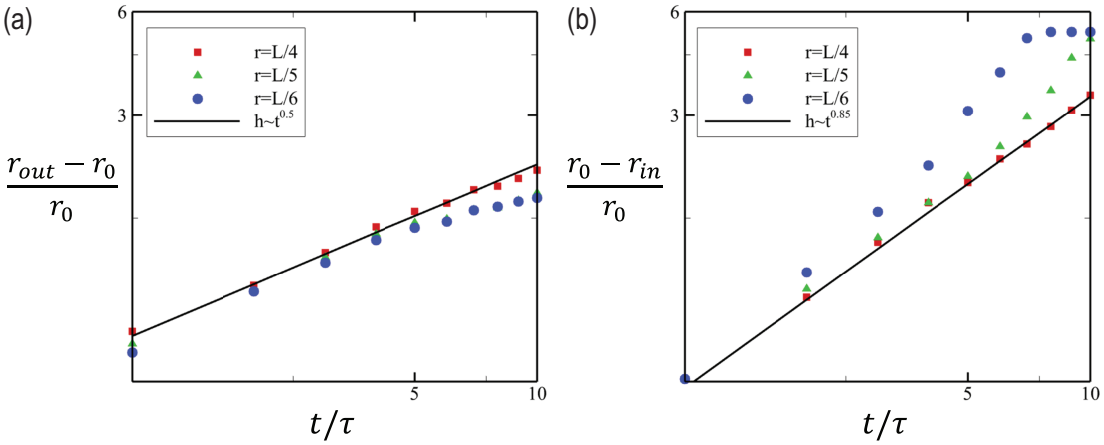

Figure B.1: Time evolution of the mixing region width of (a) the outer layer and (b) the inner layer for turbulence with the different initial radii: $r = L/4$ (red, square), $r = L/5$ (green, triangle), and $r = L/6$ (blue, circle). The solid lines are derived from dimensional analysis.

is equal to the Taylor microscale in cases 1 and 3, follows a power law and shows no unphysical behavior for developing the mixing region. Accordingly, the initial radius is set to $r_0 = L/4$ for all cases.

BIBLIOGRAPHY

BIBLIOGRAPHY

Aluie, H. (2011), Compressible turbulence: the cascade and its locality, *Physical Review Letters*, *106*(17), 174,502.

An, E., and E. Johnsen (2018), Initialization of decaying turbulence to study turbulent/non-turbulent interfaces, *Bulletin of the American Physical Society*, *63*.

Andrejczuk, M., W. W. Grabowski, S. P. Malinowski, and P. K. Smolarkiewicz (2004), Numerical simulation of cloud-clear air interfacial mixing, *Journal of the Atmospheric Sciences*, *61*(14), 1726–1739.

Baker, M., R. Breidenthal, T. Choularton, and J. Latham (1984), The effects of turbulent mixing in clouds, *Journal of Atmospheric Sciences*, *41*(2), 299–304.

Barenblatt, G., N. Galerkina, and M. Luneva (1987), Evolution of a turbulent burst, *Journal of Engineering Physics*, *53*(5), 1246–1252.

Batchelor, C. K., and G. K. Batchelor (1967), *An introduction to fluid dynamics*, Cambridge University Press.

Batchelor, G. K. (1953), *The theory of homogeneous turbulence*, Cambridge University Press.

Batchelor, G. K., and I. Proudman (1956), The large-scale structure of homogenous turbulence, *Philosophical Transactions of the Royal Society of London. Series A, Mathematical and Physical Sciences*, *248*(949), 369–405.

Batchelor, G. K., and A. A. Townsend (1948a), Decay of turbulence in the final period, *Proceedings of the Royal Society of London. Series A. Mathematical and Physical Sciences*, *194*(1039), 527–543.

Batchelor, G. K., and A. A. Townsend (1948b), Decay of isotropic turbulence in the initial period, *Proceedings of the Royal Society of London. Series A. Mathematical and Physical Sciences*, *193*(1035), 539–558.

Bell, G. I. (1951), Taylor instability on cylinders and spheres in small amplitude approximation, *Los Alamos Scientific Laboratory report*, *LA-1321*.

Benzi, R., L. Biferale, R. T. Fisher, L. P. Kadanoff, D. Q. Lamb, and F. Toschi (2008), Intermittency and universality in fully developed inviscid and weakly compressible turbulent flows, *Physical Review Letters*, *100*(23), 234,503.

Bhat, G., and R. Narasimha (1996), A volumetrically heated jet: large-eddy structure and entrainment characteristics, *Journal of Fluid Mechanics*, *325*, 303–330.

Bisset, D. K., J. C. Hunt, and M. M. Rogers (2002), The turbulent/non-turbulent interface bounding a far wake, *Journal of Fluid Mechanics*, *451*, 383–410.

Blaisdell, G., E. Spyropoulos, and J. Qin (1996), The effect of the formulation of nonlinear terms on aliasing errors in spectral methods, *Applied Numerical Mathematics*, *21*(3), 207–219.

Blyth, A. M. (1993), Entrainment in cumulus clouds, *Journal of Applied Meteorology and Climatology*, *32*(4), 626–641.

Breda, M., and O. R. Buxton (2019), Behaviour of small-scale turbulence in the turbulent/non-turbulent interface region of developing turbulent jets, *Journal of Fluid Mechanics*, *879*, 187–216.

Briggs, D., J. Ferziger, J. Koseff, and S. Monismith (1996), Entrainment in a shear-free turbulent mixing layer, *Journal of Fluid Mechanics*, *310*, 215–241.

Bryan, K., S. Manabe, and R. C. Pacanowski (1975), A global ocean-atmosphere climate model. part ii. the oceanic circulation, *Journal of Physical Oceanography*, *5*(1), 30–46.

Burattini, P., P. Lavoie, A. Agrawal, L. Djenidi, and R. Antonia (2006), Power law of decaying homogeneous isotropic turbulence at low reynolds number, *Physical Review E*, *73*(6), 066,304.

Buxton, O., M. Breda, and K. Dhall (2019), Importance of small-scale anisotropy in the turbulent/nonturbulent interface region of turbulent free shear flows, *Physical Review Fluids*, *4*(3), 034,603.

Caldwell, D. R., and J. N. Mourn (1995), Turbulence and mixing in the ocean, *Reviews of Geophysics*, *33*(S2), 1385–1394.

Cao, N., S. Chen, and G. D. Doolen (1999), Statistics and structures of pressure in isotropic turbulence, *Physics of Fluids*, *11*(8), 2235–2250.

Castro, D., P. Slane, D. C. Ellison, and D. J. Patnaude (2012), Fermi-lat observations and a broadband study of supernova remnant ctb 109, *The Astrophysical Journal*, *756*(1), 88.

Cenedese, C., and C. Adduce (2010), A new parameterization for entrainment in overflows, *Journal of Physical Oceanography*, *40*(8), 1835–1850.

Chasnov, J. (1994), Similarity states of passive scalar transport in isotropic turbulence, *Physics of Fluids*, *6*(2), 1036–1051.

Chauhan, K., J. Philip, and I. Marusic (2014), Scaling of the turbulent/non-turbulent interface in boundary layers, *Journal of Fluid Mechanics*, *751*, 298–328.

Chu, B.-T., and L. S. Kovásznay (1958), Non-linear interactions in a viscous heat-conducting compressible gas, *Journal of Fluid Mechanics*, *3*(5), 494–514.

Comte-Bellot, G., and S. Corrsin (1966), The use of a contraction to improve the isotropy of grid-generated turbulence, *Journal of Fluid Mechanics*, *25*(4), 657–682.

Cook, A. W., and P. E. Dimotakis (2001), Transition stages of rayleigh-taylor instability between miscible fluids, *Journal of Fluid Mechanics*, *443*, 69.

Corrsin, S. (1951), The decay of isotropic temperature fluctuations in an isotropic turbulence, *Journal of the Aeronautical Sciences*, *18*(6), 417–423.

Corrsin, S., and A. Kistler (1954), The free-stream boundaries of turbulent flows, *NACA Technical Notes*, *3133*.

da Silva, C. B., and R. J. N. dos Reis (2011), The role of coherent vortices near the turbulent/non-turbulent interface in a planar jet, *Philosophical Transactions of the Royal Society A: Mathematical, Physical and Engineering Sciences*, *369*(1937), 738–753.

da Silva, C. B., and R. R. Taveira (2010), The thickness of the turbulent/nonturbulent interface is equal to the radius of the large vorticity structures near the edge of the shear layer, *Physics of Fluids*, *22*(12), 121,702.

da Silva, C. B., J. C. Hunt, I. Eames, and J. Westerweel (2014a), Interfacial layers between regions of different turbulence intensity, *Annual Review of Fluid Mechanics*, *46*(1), 567–590.

da Silva, C. B., R. R. Taveira, and G. Borrell (2014b), Characteristics of the turbulent/nonturbulent interface in boundary layers, jets and shear-free turbulence, in *Journal of Physics: Conference Series*, vol. 506, p. 012015, IOP Publishing.

Davidson, P. A. (2015), *Turbulence: an introduction for scientists and engineers*, Oxford University Press.

Dimonte, G., et al. (2004), A comparative study of the turbulent rayleigh–taylor instability using high-resolution three-dimensional numerical simulations: the alpha-group collaboration, *Physics of Fluids*, *16*(5), 1668–1693.

Dimotakis, P. E. (1991), Turbulent free shear layer mixing and combustion, *High Speed Flight Propulsion Systems*, *137*, 265–340.

Dimotakis, P. E. (2000), The mixing transition in turbulent flows, *Journal of Fluid Mechanics*, *409*, 69–98.

Dimotakis, P. E. (2005), Turbulent mixing, *Annual Review of Fluid Mechanics*, *37*, 329–356.

Djenidi, L., M. Kamruzzaman, and R. Antonia (2015), Power-law exponent in the transition period of decay in grid turbulence, *Journal of Fluid Mechanics*, *779*, 544–555.

Donzis, D. A., and S. Jagannathan (2013), Fluctuations of thermodynamic variables in stationary compressible turbulence, *Journal of Fluid Mechanics*, *733*, 221–244.

Donzis, D. A., and J. P. John (2020), Universality and scaling in homogeneous compressible turbulence, *Physical Review Fluids*, *5*(8), 084,609.

Donzis, D. A., K. R. Sreenivasan, and P. Yeung (2005), Scalar dissipation rate and dissipative anomaly in isotropic turbulence, *Journal of Fluid Mechanics*, *532*, 199–216.

Donzis, D. A., P. Yeung, and K. R. Sreenivasan (2008), Dissipation and enstrophy in isotropic turbulence: resolution effects and scaling in direct numerical simulations, *Physics of Fluids*, *20*(4), 045,108.

Driedonks, A., and H. Tennekes (1984), Entrainment effects in the well-mixed atmospheric boundary layer, *Boundary-Layer Meteorology*, *30*(1), 75–105.

Dubrulle, B. (2000), Finite size scale invariance, *The European Physical Journal B*, *14*(4), 757–771.

Ducros, F., F. Laporte, T. Soulères, V. Guinot, P. Moinat, and B. Caruelle (2000), High-order fluxes for conservative skew-symmetric-like schemes in structured meshes: application to compressible flows, *Journal of Computational Physics*, *161*(1), 114–139.

Durbin, P. (2021), *Advanced approaches in turbulence: theory, modeling, simulation, and data analysis for turbulent flows*, Elsevier.

Durbin, P. A. (1991), Near-wall turbulence closure modeling without "damping functions", *Theoretical and Computational Fluid Dynamics*, *3*(1), 1–13.

Eisma, J., J. Westerweel, G. Ooms, and G. E. Elsinga (2015), Interfaces and internal layers in a turbulent boundary layer, *Physics of Fluids*, *27*(5), 055,103.

Emanuel, K. A., and M. Živković-Rothman (1999), Development and evaluation of a convection scheme for use in climate models, *Journal of the Atmospheric Sciences*, *56*(11), 1766–1782.

Ertunç, Ö., N. Özyilmaz, H. Lienhart, F. Durst, and K. Beronov (2010), Homogeneity of turbulence generated by static-grid structures, *Journal of Fluid Mechanics*, *654*, 473–500.

Esteban, L. B., J. Shrimpton, and B. Ganapathisubramani (2019), Laboratory experiments on the temporal decay of homogeneous anisotropic turbulence, *Journal of Fluid Mechanics*, *862*, 99–127.

Federrath, C. (2018), The turbulent formation of stars, *Physics Today*.

Freund, J. B., S. K. Lele, and P. Moin (2000), Compressibility effects in a turbulent annular mixing layer. part 1. turbulence and growth rate, *Journal of Fluid Mechanics*, *421*, 229–267.

Frisch, U., P.-L. Sulem, and M. Nelkin (1978), A simple dynamical model of intermittent fully developed turbulence, *Journal of Fluid Mechanics*, *87*(4), 719–736.

Gad-el Hak, M., and S. Corrsin (1974), Measurements of the nearly isotropic turbulence behind a uniform jet grid, *Journal of Fluid Mechanics*, *62*(1), 115–143.

Garreaud, R. D., and P. Aceituno (2007), Atmospheric circulation and climatic variability, *The physical geography of South America*, *45*, 59.

Garrett, C. (1979), Mixing in the ocean interior, *Dynamics of Atmospheres and Oceans*, *3*(2-4), 239–265.

Garwood Jr, R. (1979), Air-sea interaction and dynamics of the surface mixed layer, *Reviews of Geophysics*, *17*(7), 1507–1524.

Gaskin, S., M. McKernan, and F. Xue (2004), The effect of background turbulence on jet entrainment: an experimental study of a plane jet in a shallow coflow, *Journal of Hydraulic Research*, *42*(5), 533–542.

George, W. K. (1992), The decay of homogeneous isotropic turbulence, *Physics of Fluids*, *4*(7), 1492–1509.

George, W. K., and H. Wang (2009), The exponential decay of homogeneous turbulence, *Physics of Fluids*, *21*(2), 025,108.

Germano, M., U. Piomelli, P. Moin, and W. H. Cabot (1991), A dynamic subgrid-scale eddy viscosity model, *Physics of Fluids*, *3*(7), 1760–1765.

Gotoh, T., and D. Fukayama (2001), Pressure spectrum in homogeneous turbulence, *Physical Review Letters*, *86*(17), 3775.

Grotch, S. L., and M. C. MacCracken (1991), The use of general circulation models to predict regional climatic change, *Journal of Climate*, *4*(3), 286–303.

Gualtieri, P., C. Casciola, R. Benzi, G. Amati, and R. Piva (2002), Scaling laws and intermittency in homogeneous shear flow, *Physics of Fluids*, *14*(2), 583–596.

Hassan, W. U., and M. A. Nayak (2020), Global teleconnections in droughts caused by oceanic and atmospheric circulation patterns, *Environmental Research Letters*, *16*(1), 014,007.

Haworth, D., and S. Pope (1987), A pdf modeling study of self-similar turbulent free shear flows, *Physics of Fluids*, *30*(4), 1026–1044.

Holzner, M., A. Liberzon, N. Nikitin, W. Kinzelbach, and A. Tsinober (2007), Small-scale aspects of flows in proximity of the turbulent/nonturbulent interface, *Physics of Fluids*, *19*(7), 071,702.

Hughes, T. J., L. Mazzei, A. A. Oberai, and A. A. Wray (2001), The multiscale formulation of large eddy simulation: Decay of homogeneous isotropic turbulence, *Physics of Fluids*, *13*(2), 505–512.

Hunt, J. C., A. A. Wray, and P. Moin (1988), Eddies, streams, and convergence zones in turbulent flows, *Center for Turbulence Research Report*, *CTR-S88*.

Hunt, J. C., I. Eames, and J. Westerweel (2006), Mechanics of inhomogeneous turbulence and interfacial layers, *Journal of Fluid Mechanics*, *554*, 499–519.

Hurst, D., and J. Vassilicos (2007), Scalings and decay of fractal-generated turbulence, *Physics of Fluids*, *19*(3), 035,103.

Ireland, P. J., and L. R. Collins (2012), Direct numerical simulation of inertial particle entrainment in a shearless mixing layer, *Journal of Fluid Mechanics*, *704*, 301–332.

Isaza, J. C., R. Salazar, and Z. Warhaft (2014), On grid-generated turbulence in the near-and far field regions, *Journal of Fluid Mechanics*, *753*, 402–426.

Ishida, T., P. Davidson, and Y. Kaneda (2006), On the decay of isotropic turbulence, *Journal of Fluid Mechanics*, *564*, 455–475.

Ishihara, T., T. Gotoh, and Y. Kaneda (2009), Study of high-reynolds number isotropic turbulence by direct numerical simulation, *Annual Review of Fluid Mechanics*, *41*(1), 165–180.

Ishihara, T., Y. Kaneda, and J. C. Hunt (2013), Thin shear layers in high reynolds number turbulence—dns results, *Flow, Turbulence and Combustion*, *91*(4), 895–929.

Jagannathan, S., and D. A. Donzis (2016), Reynolds and mach number scaling in solenoidally-forced compressible turbulence using high-resolution direct numerical simulations, *Journal of Fluid Mechanics*, *789*, 669–707.

Jiménez, J., A. A. Wray, P. G. Saffman, and R. S. Rogallo (1993), The structure of intense vorticity in isotropic turbulence, *Journal of Fluid Mechanics*, *255*, 65–90.

John, J. P., D. A. Donzis, and K. R. Sreenivasan (2019), Solenoidal scaling laws for compressible mixing, *Physical Review Letters*, *123*(22), 224,501.

Johnsen, E., et al. (2010), Assessment of high-resolution methods for numerical simulations of compressible turbulence with shock waves, *Journal of Computational Physics*, *229*(4), 1213–1237.

Kaneda, Y., and T. Ishihara (2006), High-resolution direct numerical simulation of turbulence, *Journal of Turbulence*, (7), N20.

Kang, H. S., and C. Meneveau (2008), Experimental study of an active grid-generated shearless mixing layer and comparisons with large-eddy simulation, *Physics of Fluids*, *20*(12), 125,102.

Kida, S., and S. A. Orszag (1990), Energy and spectral dynamics in forced compressible turbulence, *Journal of Scientific Computing*, *5*(2), 85–125.

Kida, S., and S. A. Orszag (1992), Energy and spectral dynamics in decaying compressible turbulence, *Journal of Scientific Computing*, *7*(1), 1–34.

Knietzsch, M.-A., A. Schröder, V. Lucarini, and F. Lunkeit (2015), The impact of oceanic heat transport on the atmospheric circulation, *Earth System Dynamics*, *6*(2), 591–615.

Kolmogorov, A. N. (1941a), The local structure of turbulence in incompressible viscous fluid for very large reynolds numbers, *Cr Acad. Sci. URSS*, *30*, 301–305.

Kolmogorov, A. N. (1941b), Dissipation of energy in the locally isotropic turbulence, in *Dokl. Akad. Nauk SSSR A*, vol. 32, pp. 16–18.

Kolmogorov, A. N. (1962), A refinement of previous hypotheses concerning the local structure of turbulence in a viscous incompressible fluid at high reynolds number, *Journal of Fluid Mechanics*, *13*(1), 82–85.

Kousky, V. E., M. T. Kagano, and I. F. Cavalcanti (1984), A review of the southern oscillation: oceanic-atmospheric circulation changes and related rainfall anomalies, *Tellus A*, *36*(5), 490–504.

Kovasznay, L. S. (1953), Turbulence in supersonic flow, *Journal of the Aeronautical Sciences*, *20*(10), 657–674.

Krogstad, P.-Å., and P. Davidson (2011), Freely decaying, homogeneous turbulence generated by multi-scale grids, *Journal of Fluid Mechanics*, *680*, 417–434.

Krogstad, P.-Å., and P. Davidson (2012), Near-field investigation of turbulence produced by multi-scale grids, *Physics of Fluids*, *24*(3), 035,103.

Kumar, S., H. Hornung, and B. Sturtevant (2003), Growth of shocked gaseous interfaces in a conical geometry, *Physics of Fluids*, *15*(10), 3194–3208.

Kwon, Y., J. Philip, C. De Silva, N. Hutchins, and J. Monty (2014), The quiescent core of turbulent channel flow, *Journal of Fluid Mechanics*, *751*, 228–254.

Launder, B., A. Morse, W. Rodi, and D. Spalding (1973), Prediction of free shear flows: a comparison of the performance of six turbulence models, *NASA. Langley Research Center Free Turbulent Shear Flows*.

Laval, J., B. Dubrulle, and S. Nazarenko (2001), Nonlocality and intermittency in three-dimensional turbulence, *Physics of Fluids*, *13*(7), 1995–2012.

Lavoie, P., L. Djenidi, and R. Antonia (2007), Effects of initial conditions in decaying turbulence generated by passive grids, *Journal of Fluid Mechanics*, *585*, 395–420.

Lee, J., H. J. Sung, and T. A. Zaki (2017), Signature of large-scale motions on turbulent/non-turbulent interface in boundary layers, *Journal of Fluid Mechanics*, *819*, 165–187.

Lee, M. J. (1985), Numerical experiments on the structure of homogeneous turbulence.

Lee, S., S. K. Lele, and P. Moin (1991), Eddy shocklets in decaying compressible turbulence, *Physics of Fluids*, *3*(4), 657–664.

Lele, S. K. (1994), Compressibility effects on turbulence, *Annual Review of Fluid Mechanics*, *26*(1), 211–254.

Lombardini, M., and D. Pullin (2009), Small-amplitude perturbations in the three-dimensional cylindrical richtmyer–meshkov instability, *Physics of Fluids*, *21*(11), 114,103.

Lombardini, M., D. Pullin, and D. Meiron (2014a), Turbulent mixing driven by spherical implosions. part 1. flow description and mixing-layer growth, *Journal of Fluid Mechanics*, *748*, 85–112.

Lombardini, M., D. Pullin, and D. Meiron (2014b), Turbulent mixing driven by spherical implosions. part 2. turbulence statistics, *Journal of Fluid Mechanics*, *748*, 113–142.

Mankbadi, M. R., and S. Balachandar (2012), Compressible inviscid instability of rapidly expanding spherical material interfaces, *Physics of Fluids*, *24*(3), 034,106.

Mansour, N., and A. Wray (1994), Decay of isotropic turbulence at low reynolds number, *Physics of Fluids*, *6*(2), 808–814.

Mathew, J., and A. J. Basu (2002), Some characteristics of entrainment at a cylindrical turbulence boundary, *Physics of Fluids*, *14*(7), 2065–2072.

Matsushima, T., K. Nagata, and T. Watanabe (2021), Wavelet analysis of shearless turbulent mixing layer, *Physics of Fluids*, *33*(2), 025,109.

Mellado, J. P. (2017), Cloud-top entrainment in stratocumulus clouds, *Annual Review of Fluid Mechanics*, *49*, 145–169.

Mikaelian, K. O. (1990), Rayleigh-taylor and richtmyer-meshkov instabilities and mixing in stratified spherical shells, *Physical Review A*, *42*(6), 3400.

Mikaelian, K. O. (2005), Rayleigh-taylor and richtmyer-meshkov instabilities and mixing in stratified cylindrical shells, *Physics of Fluids*, *17*(9), 094,105.

Mohamed, M. S., and J. C. LaRue (1990), The decay power law in grid-generated turbulence, *Journal of Fluid Mechanics*, *219*, 195–214.

Moin, P., and K. Mahesh (1998), Direct numerical simulation: a tool in turbulence research, *Annual Review of Fluid Mechanics*, *30*(1), 539–578.

Movahed, P., and E. Johnsen (2015), The mixing region in freely decaying variable-density turbulence, *Journal of Fluid Mechanics*, *772*, 386–426.

Moyal, J. E. (1952), The spectra of turbulence in a compressible fluid; eddy turbulence and random noise, in *Mathematical Proceedings of the Cambridge Philosophical Society*, vol. 48, pp. 329–344, Cambridge University Press.

Mueschke, N. J., and O. Schilling (2009), Investigation of rayleigh-taylor turbulence and mixing using direct numerical simulation with experimentally measured initial conditions. i. comparison to experimental data, *Physics of Fluids*, *21*(1), 014,106.

Overholt, M., and S. Pope (1996), Direct numerical simulation of a passive scalar with imposed mean gradient in isotropic turbulence, *Physics of Fluids*, *8*(11), 3128–3148.

Pan, S., and E. Johnsen (2017), The role of bulk viscosity on the decay of compressible, homogeneous, isotropic turbulence, *Journal of Fluid Mechanics*, *833*, 717–744.

Panickacheril John, J., D. A. Donzis, and K. R. Sreenivasan (2022), Laws of turbulence decay from direct numerical simulations, *Philosophical Transactions of the Royal Society A*, *380*(2218), 20210,089.

Parneix, S., and P. Durbin (1996), A new methodology for turbulence modelers using dns database analysis, *Annual Research Briefs*, *1996*, 17–30.

Passot, T., and A. Pouquet (1987), Numerical simulation of compressible homogeneous flows in the turbulent regime, *Journal of Fluid Mechanics*, *181*, 441–466.

Penc, R. S., and B. A. Albrecht (1987), Parametric representation of heat and moisture fluxes in cloud-topped mixed layers, *Boundary-layer meteorology*, *38*(3), 225–248.

Pirozzoli, S. (2011), Numerical methods for high-speed flows, *Annual Review of Fluid Mechanics*, *43*, 163–194.

Plesset, M. (1954), On the stability of fluid flows with spherical symmetry, *Journal of Applied Physics*, *25*(1), 96–98.

Pope, S. B. (2000), *Turbulent flows*, Cambridge University Press.

Pouransari, H., M. Mortazavi, and A. Mani (2016), Parallel variable-density particle-laden turbulence simulation, *Center for Turbulence Research*.

Pruppacher, H. R., J. D. Klett, and P. K. Wang (1998), Microphysics of clouds and precipitation.

Randall, D. A. (2000), *General circulation model development: past, present, and future*, Elsevier.

Rascle, N., F. Ardhuin, and E. A. Terray (2006), Drift and mixing under the ocean surface: A coherent one-dimensional description with application to unstratified conditions, *Journal of Geophysical Research: Oceans*, *111*(C3).

Reichler, T. (2009), Changes in the atmospheric circulation as indicator of climate change, in *Climate Change*, pp. 145–164, Elsevier.

Reynolds, A., and H. Tucker (1975), The distortion of turbulence by general uniform irrotational strain, *Journal of Fluid Mechanics*, *68*(4), 673–693.

Richardson, L. F. (1922), *Weather prediction by numerical process*, University Press.

Rodi, W., and N. Mansour (1993), Low reynolds number k—ε modelling with the aid of direct simulation data, *Journal of Fluid Mechanics*, *250*, 509–529.

Rogallo, R. S. (1981), *Numerical experiments in homogeneous turbulence*, vol. 81315, National Aeronautics and Space Administration.

Rogers, M. M. (1986), *The structure and modeling of the hydrodynamic and passive scalar fields in homogeneous turbulent shear flow*, Stanford University.

Saffman, P. (1967), Note on decay of homogeneous turbulence, *Physics of Fluids*, *10*(6), 1349–1349.

Sahany, S., J. D. Neelin, K. Hales, and R. B. Neale (2012), Temperature-moisture dependence of the deep convective transition as a constraint on entrainment in climate models, *Journal of the Atmospheric Sciences*, *69*(4), 1340–1358.

Sarkar, S. (1992), The pressure-dilatation correlation in compressible flows, *Physics of Fluids*, *4*(12), 2674–2682.

Sarkar, S., G. Erlebacher, M. Y. Hussaini, and H. O. Kreiss (1991), The analysis and modelling of dilatational terms in compressible turbulence, *Journal of Fluid Mechanics*, *227*, 473–493.

Satoh, M. (2004), *Atmospheric circulation dynamics and circulation models*, Springer Science & Business Media.

Seoud, R., and J. Vassilicos (2007), Dissipation and decay of fractal-generated turbulence, *Physics of Fluids*, *19*(10), 105,108.

Sethuraman, Y. P. M., and K. Sinha (2020), Effect of turbulent mach number on the thermodynamic fluctuations in canonical shock-turbulence interaction, *Computers & Fluids*, *197*, 104,354.

Shawon, A. S. M., P. Prabhakaran, G. Kinney, R. A. Shaw, and W. Cantrell (2021), Dependence of aerosol-droplet partitioning on turbulence in a laboratory cloud, *Journal of Geophysical Research: Atmospheres*, *126*(5), e2020JD033,799.

She, Z.-S., E. Jackson, and S. A. Orszag (1990), Intermittent vortex structures in homogeneous isotropic turbulence, *Nature*, *344*(6263), 226–228.

She, Z.-S., S. Chen, G. Doolen, R. H. Kraichnan, and S. A. Orszag (1993), Reynolds number dependence of isotropic navier-stokes turbulence, *Physical Review Letters*, *70*(21), 3251.

Shih, T.-H. (1997), Some developments in computational modeling of turbulent flows, *Fluid Dynamics Research*, *20*(1-6), 67.

Silva, T. S., M. Zecchetto, and C. B. da Silva (2018), The scaling of the turbulent/non-turbulent interface at high reynolds numbers, *Journal of Fluid Mechanics*, *843*, 156.

Skyllingstad, E. D., W. Smyth, and G. Crawford (2000), Resonant wind-driven mixing in the ocean boundary layer, *Journal of Physical Oceanography*, *30*(8), 1866–1890.

Slane, P., A. Bykov, D. C. Ellison, G. Dubner, and D. Castro (2015), Supernova remnants interacting with molecular clouds: X-ray and gamma-ray signatures, *Space Science Reviews*, *188*, 187–210.

Speziale, C. G. (1991), Analytical methods for the development of reynolds-stress closures in turbulence, *Annual Review of Fluid Mechanics*, *23*(1), 107–157.

Sreenivasan, K. R. (1984), On the scaling of the turbulence energy dissipation rate, *Physics of Fluids*, *27*(5), 1048–1051.

Sreenivasan, K. R. (1998), An update on the energy dissipation rate in isotropic turbulence, *Physics of Fluids*, *10*(2), 528–529.

St. Laurent, L., and C. Garrett (2002), The role of internal tides in mixing the deep ocean, *Journal of Physical Oceanography*, *32*(10), 2882–2899.

Stalp, S. R., L. Skrbek, and R. J. Donnelly (1999), Decay of grid turbulence in a finite channel, *Physical Review Letters*, *82*(24), 4831.

Takahashi, H., Z. J. Luo, and G. Stephens (2021), Revisiting the entrainment relationship of convective plumes: A perspective from global observations, *Geophysical Research Letters*, *48*(6), e2020GL092,349.

Teixeira, M. A., and C. da Silva (2012), Turbulence dynamics near a turbulent/non-turbulent interface, *Journal of Fluid Mechanics*, *695*, 257–287.

Thormann, A., and C. Meneveau (2015), Decaying turbulence in the presence of a shearless uniform kinetic energy gradient, *Journal of Turbulence*, *16*(5), 442–459.

Tordella, D., and M. Iovieno (2006), Numerical experiments on the intermediate asymptotics of shear-free turbulent transport and diffusion, *Journal of Fluid Mechanics*, *549*, 429–441.

Tordella, D., and M. Iovieno (2011), Small-scale anisotropy in turbulent shearless mixing, *Physical Review Letters*, *107*(19), 194,501.

Toschi, F., G. Amati, S. Succi, R. Benzi, and R. Piva (1999), Intermittency and structure functions in channel flow turbulence, *Physical Review Letters*, *82*(25), 5044.

Townsend, A. A. (1980), *The structure of turbulent shear flow*, Cambridge University Press.

Townsend, A. A., and G. Taylor (1948), Experimental evidence for the theory of local isotropy, in *Mathematical Proceedings of the Cambridge Philosophical Society*, vol. 44, pp. 560–565, Cambridge University Press.

Tucker, H. J., and A. Reynolds (1968), The distortion of turbulence by irrotational plane strain, *Journal of Fluid Mechanics*, *32*(4), 657–673.

Valente, P., and J. Vassilicos (2012), Dependence of decaying homogeneous isotropic turbulence on inflow conditions, *Physics Letters A*, *376*(4), 510–514.

Van Dyke, M., and M. Van Dyke (1982), *An album of fluid motion*, vol. 176, Parabolic Press Stanford.

Vassilicos, J. C. (2015), Dissipation in turbulent flows, *Annual Review of Fluid Mechanics*, *47*, 95–114.

Veeravalli, S., and Z. Warhaft (1989), The shearless turbulence mixing layer, *Journal of Fluid Mechanics*, *207*, 191–229.

Wang, H., and W. K. George (2002), The integral scale in homogeneous isotropic turbulence, *Journal of Fluid Mechanics*, *459*, 429–443.

Wang, L.-P., S. Chen, J. G. Brasseur, and J. C. Wyngaard (1996), Examination of hypotheses in the kolmogorov refined turbulence theory through high-resolution simulations. part 1. velocity field, *Journal of Fluid Mechanics*, *309*, 113–156.

Warhaft, Z. (2000), Passive scalars in turbulent flows, *Annual Review of Fluid Mechanics*, *32*(1), 203–240.

Weart, S. (2010), The development of general circulation models of climate, *Studies in History and Philosophy of Science Part B: Studies in History and Philosophy of Modern Physics*, *41*(3), 208–217.

Westerweel, J., C. Fukushima, J. Pedersen, and J. Hunt (2005), Mechanics of the turbulent-nonturbulent interface of a jet, *Physical Review Letters*, *95*(17), 174,501.

Westerweel, J., C. Fukushima, J. M. Pedersen, and J. C. Hunt (2009), Momentum and scalar transport at the turbulent/non-turbulent interface of a jet, *Journal of Fluid Mechanics*, *631*, 199–230.

Yeung, P., and Y. Zhou (1997), Universality of the kolmogorov constant in numerical simulations of turbulence, *Physical Review E*, *56*(2), 1746.

Yeung, P., S. Pope, A. Lamorgese, and D. Donzis (2006), Acceleration and dissipation statistics of numerically simulated isotropic turbulence, *Physics of Fluids*, *18*(6), 065,103.

Yoder, D. A., J. R. DeBonis, and N. J. Georgiadis (2015), Modeling of turbulent free shear flows, *Computers & Fluids*, *117*, 212–232.

Young, W., P. Rhines, and C. Garrett (1982), Shear-flow dispersion, internal waves and horizontal mixing in the ocean, *Journal of Physical Oceanography*, *12*(6), 515–527.

Youngs, D. L. (1984), Numerical simulation of turbulent mixing by rayleigh-taylor instability, *Physica D: Nonlinear Phenomena*, *12*(1-3), 32–44.

Yu, H., and D. Livescu (2008), Rayleigh-taylor instability in cylindrical geometry with compressible fluids, *Physics of Fluids*, *20*(10), 104,103.

Yu, K., T. Colonius, D. Pullin, and G. Winckelmans (2021), Dynamics and decay of a spherical region of turbulence in free space, *Journal of Fluid Mechanics*, *907*.

Zecchetto, M., and C. B. da Silva (2021), Universality of small-scale motions within the turbulent/non-turbulent interface layer, *Journal of Fluid Mechanics*, *916*, A9.

Zeman, O. (1990), Dilatation dissipation: the concept and application in modeling compressible mixing layers, *Physics of Fluids*, *2*(2), 178–188.